The Henryk Niewodniczański
Institute of Nuclear Physics
Polish Academy of Sciences

Doctoral Thesis

Study of *b*-jet production and properties at the LHC

Author:
Sebastian Bysiak

Supervisor:
dr hab. Jacek Otwinowski,
profesor IFJ PAN

Assistant Supervisor:
dr Iwona Sputowska

September, 2023

Abstract

Jet production is a fundamental probe of perturbative quantum chromodynamics (pQCD). They play a vital role also in other areas of high energy physics. Jet quenching is arguably one of the most spectacular proofs of the creation of quark-gluon plasma in ultrarelativistic collisions of heavy ions.

Nowadays, the rise of novel experimental techniques, including jet substructure observables and the application of machine learning algorithms, are revolutionizing this field of study. New jet tagging capabilities allow for comparative studies between jet flavours. Substructure measurements open doors for direct observation of the effects, entangled into more generic observables. A perfect example is the dead-cone measurement by ALICE.

Results shown in this thesis benefit from both of these advances. The first part describes the analysis of the beauty-jet production cross section, measured in pp collisions at $\sqrt{s} = 5.02\,\text{TeV}$ by the ALICE experiment at the LHC. It is the first application of machine learning for heavy-flavour jet measurements in ALICE. The new method significantly improves tagging efficiency and purity, and shows a good stability over a wide range of these parameters. Results are consistent with the NLO pQCD predictions and the ALICE results obtained with other methods.

The second part shows simulation studies for the dead-cone effect measurement for beauty jets in heavy-ion collisions. The study focuses on the removal of distortions introduced by uncorrelated heavy-ion background. The combination of jet reclustering and jet grooming allows for the restoration of the quantitative properties related to the dead-cone effect of jets. Additionally, this thesis highlights some potential issues that may arise during future measurements of this effect, which are not immediately apparent.

Streszczenie

Pomiary produkcji dżetów stanowią fundamentalne narzędzie badawcze w zakresie perturbatywnej chromodynamiki kwantowej (pQCD). Pełnią one również istotną rolę w innych dziedzinach fizyki wysokich energii. Tłumienie dżetów jest prawdopodobnie jednym z najbardziej spektakularnych dowodów na tworzenie się plazmy kwarkowo-gluonowej w ultrarelatywistycznych zderzeniach ciężkich jonów.

Współcześnie pojawienie się nowatorskich technik eksperymentalnych, w tym obserwacji wewnętrznej struktury dżetów oraz zastosowania algorytmów uczenia maszynowego, rewolucjonizuje ten obszar badań. Nowe możliwości znakowania dżetów pozwalają na badania porównawcze między dżetami pochodzącymi z różnych partonów. Pomiar wewnętrznej struktury otwiera drzwi do bezpośrednich obserwacji efektów splątanych dotąd w bardziej ogólnych obserwacjach. Doskonałym przykładem jest pomiar efektu martwego stożka dokonany przez eksperyment ALICE.

Wyniki przedstawione w tej pracy korzystają z postępów w obu tych obszarach. Pierwsza część opisuje analizę przekroju czynnego na produkcję dżetów pięknych, zmierzonego w zderzeniach pp przy $\sqrt{s} = 5.02\,\text{TeV}$ przez eksperyment ALICE na LHC. Jest to pierwsze zastosowanie uczenia maszynowego do pomiarów dżetów ciężkich kwarków w eksperymencie ALICE. Nowa metoda znacząco poprawia wydajność i czystość znakowania oraz wykazuje stabilność w szerokim zakresie tych parametrów. Wyniki są zgodne z przewidywaniami pQCD w przybliżeniu NLO oraz wynikami ALICE uzyskanymi innymi metodami.

Druga część przedstawia badania symulacyjne efektu martwego stożka w pomiarach dżetów pięknych w zderzeniach ciężkich jonów. Badanie to skupia się na eliminacji zaburzeń wprowadzonych przez nieskorelowane tło. Połączenie re-klasteryzacji dżetów i technik ich oczyszczania pozwala na przywrócenie ilościowych właściwości dżetów związanych z efektem martwego stożka. Ponadto, praca zwraca uwagę na pewne nieoczywiste, potencjalne problemy, które mogą pojawić się podczas przyszłych pomiarów tego efektu.

Acknowledgements

I would like to express my deepest gratitude to all the people without whom this thesis would not have come into being.

First and foremost, I would like to thank my supervisor, *Jacek Otwinowski*. Our common journey had started years before my PhD program. You witnessed my scientific development over many stages, but actually, you are the main person behind it. Knowing each other for so many years, one cannot separate professional and personal life. We experienced a lot together. I would like to thank you for being accessible and always taking my side. After that many years, I can say that for sure I really enjoyed it. Thank you, *Jacek*, for everything!

As a gesture of gratitude, please accept one of your beloved arrows: $\rightarrow$.

I would like to thank fellow physicists whom I was lucky to encounter during my PhD.

First, I am thankful to *Mateusz Płoskoń* for his hospitality during my stay at Berkeley. It was the most inspiring time of my scientific career. I am grateful for the discussions and further collaboration, the results of which can be found in this thesis.

I would like to thank the people I had the pleasure to collaborate with during my stays at CERN: *Władek Trzaska, Varlen Grabski, Maciek Słupecki*. I have learned a lot from you, and it was a fun time.

I am grateful to the team at IFJ for their kindness and support: *Marek Kowalski, Adam Matyja, Iwona Sputowska*, and especially *Sándor Lökös* (good wine is always appreciated). *Iwona*, I am obliged for your hard work on reviewing this thesis – I predict a bright career in the Conference Committee for you! Special thanks to my office mates: *Himanshu, Sneha, Mirek* – it was a pleasure. I wish you good luck on your future path!

It is impossible to express my recognition to *Vladek* for his everlasting support and hard work throughout this year – it is very appreciated, *Vladek, really.*

Next, I would like to thank my school teachers and lecturers at AGH who introduced me to the complex world of physics. Speaking of people people who brought me here, the rest of these acknowledgements is in Polish...

Dziękuję *Rodzicom* za ich wkład – wychowanie, inspirację a następnie pełną swobodę w wyborze własnej ścieżki. *Mamo, Tato*, moja przygoda z nauką naprawdę zaczęła się w naszym domu. Dziękuję Wam za wsparcie przez te wszystkie lata, wiem że jesteście dumni.

Dziękuję *Braciom* i całej *Rodzinie*, za to, że zawsze mogłem na Was liczyć. Wasze wsparcie dla mnie i bliskich mi osób jest nieocenione.

Na koniec dziękuję *Teściom, Agacie i Piotrkowi*, za ich cegiełkę, którą dołożyli dokładnie 10 lat temu, we wrześniu 2013, gdy zgodzili się na wyjazd ze mną swojej córeczki na Dni Otwarte CERNu.

Author's contributions

Conference contributions

- XXIX International Workshop on Deep-Inelastic Scattering and Related Subjects
  DIS 2022, Santiago de Compostela,
  "Measurements of untagged and HF-tagged inclusive jet distributions in proton-proton collisions by ALICE"
- XXIXth International Conference on Ultra-relativistic Nucleus-Nucleus Collisions
  Quark Matter 2022, Cracow, poster
  "Measurement of b-jets in $\sqrt{s} = 5.02$ TeV pp collisions by ALICE using machine learning"
- The Eighth Annual Large Hadron Collider Physics
  LHCP 2020, online, poster
  "The Fast Interaction Trigger Upgrade for ALICE"

Publications:

- "Measurements of untagged and HF-tagged inclusive jet distributions in proton-proton collisions by ALICE", proceedings of DIS2022, Zenodo, https://doi.org/10.5281/zenodo.7260659
- "The Fast Interaction Trigger Upgrade for ALICE" PoS LHCP2020, 251 (2021)
  https://doi:10.22323/1.382.0251

Detector work on FIT:

- tests, assembling and installation of FV0
- development of Quality Control system
- trigger simulation studies
- on-call shifts

Contents

List of Figures

List of Tables

Acronyms

BDT Boosted decision trees. 39– 41, 43

CA Cambridge-Aachen. 6, 7, 9, 72, 76, 79

CS constituent subtraction. 72

DCA distance of closest approach. xiv, 27, 29, 30, 32, 33, 37, 40

DyG Dynamical Grooming. x, xvi, 10, 73, 74, 77– 80, 86, 95

HF heavy flavour. 12– 14, 17– 19, 30, 33, 37, 45, 68, 71

IROC Inner Readout Chambers. 25

MB minimum bias. 29, 36, 57

MC Monte Carlo. 35, 39, 41, 43– 46, 49, 50, 60

ML machine learning. ix, xiv, 7, 39– 41, 43– 46

PCA point of closest approach. 27

PID particle identification. 21, 23, 26

PV primary vertex. xiv, 25, 27, 30

QCD quantum chromodynamics. 2, 4

QGP quark–gluon plasma. 16, 17, 21

SD Soft Drop. x, xvi, 9, 10, 73, 74, 77, 81– 84, 86, 87, 89, 90

SM Standard Model. 1, 2

SV secondary vertex. xiv, 30, 40, 44

SVD Singular Value Decomposition. xv, 48– 50, 54, 55, 58, 59, 63, 64

UE underlying event. xiv, xv, 5– 7, 10, 30, 31, 37, 38, 48, 50, 52, 53, 60, 77

Dla A.M.B. i A.B. *– jesteście najważniejsze. . .*

Chapter 1

Introduction

1.1 Standard Model and Quantum Chromodynamics

1.1.1 Standard Model of particle physics

Standard Model (SM) of the particle physics is currently the most complete theory of interactions between elementary building blocks of matter. SM was developed in the 1950s, 60s and 70s. Still, up-to-date, none of the experiments delivered results that were contrary to its predictions. Apart from a very good agreement with all current measurements, SM has also a rich history of predicting the existence and properties of particles that were later discovered in the following decades. These particles include the charm and top quarks, gluons, as well as W, Z and Higgs bosons. Standard Model is not a complete theory of the universe as it does not describe gravity. It also does not explain a number of phenomena, mostly related to cosmological observations, like the existence of matter over anti-matter (baryon asymmetry), the potential existence of dark matter and dark energy, or some properties of neutrinos.

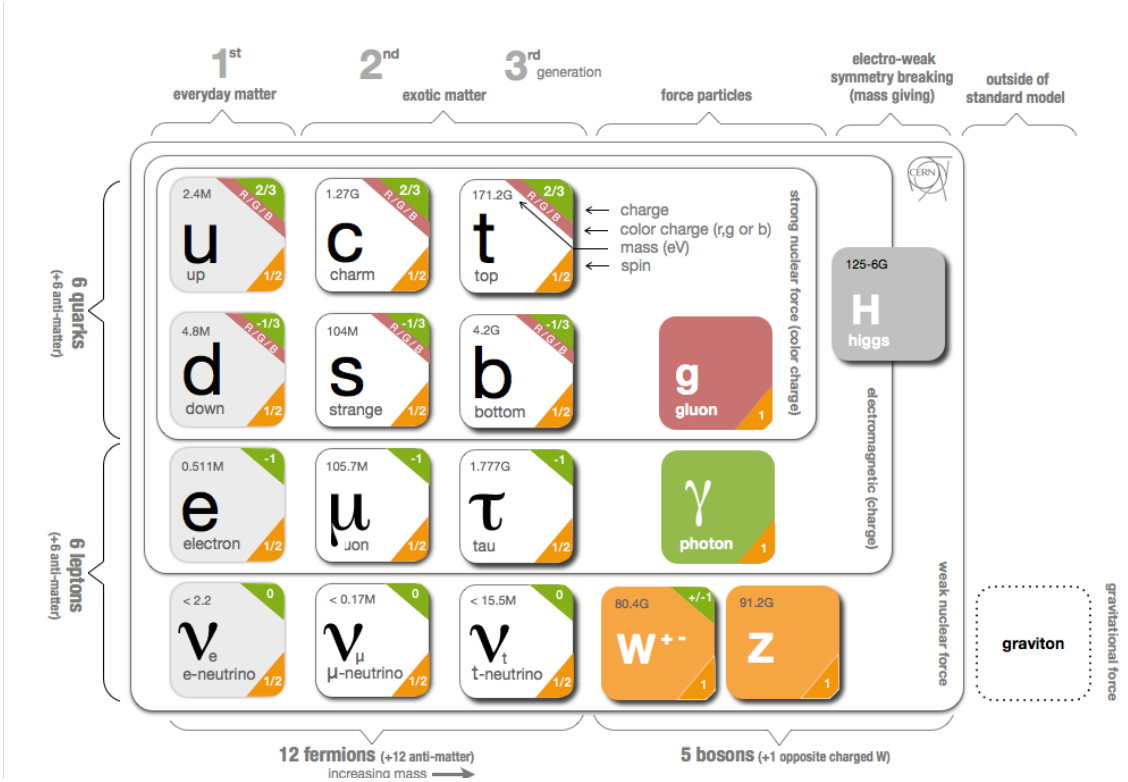

Figure 1.1: Categorisation of the particles described by the Standard Model of particle physics [1].

SM is a composition of theories developed over the years: quantum electrodynamics (QED), quantum chromodynamics (QCD), and Glashow-Weinberg-Salam theory of electro-weak interactions. The QED describes the interactions between electrically charged particles. It explains the properties of the chemical elements and compounds. The electro-weak theory incorporates QED into a more general theory together with the so-called weak nuclear forces. Weak forces are responsible for beta decay and are necessary to describe nuclear fission and fusion. QCD describes the so-called strong interactions taking place between the constituents of protons and neutrons and binding them together in atomic nuclei. The forces between nucleons are in fact just the remnants of the strong interaction between its constituents, similar to van der Waals forces.

In SM, there are 17 named elementary particles (see Fig. 1.1.): 6 particles of integer spin, called bosons, are described by Bose-Einstein statistics and 12 particles of half-integer spin called fermions are governed by Fermi-Dirac statistics and obey the Pauli exclusion principle. Matter is built from fermions, while bosons are responsible for their interactions. Photons are the carriers of electromagnetic-, gluons of strong-, and W and Z bosons of weak interactions. Discovered in 2012, the Higgs boson is a manifestation of the Higgs mechanism responsible for giving W and Z particles their mass. The standard model distinguishes two elementary fermions types: quarks and leptons. There are six different flavours of quarks: up, down, charm, strange, top, and beauty. Quarks have a fractional electric charge and carry colour charge, which makes them strongly interacting particles described by QCD. They are never observed as free particles, always bound into hadrons – groups of two (called mesons), three (baryons), or more (exotic hadrons: tetra-, pentaquarks) quarks. There are six flavours of leptons, three electrically charged ones namely electron, muon, and tau, and only weakly-interacting electron, muon, and tau neutrinos. Apart from the described above division, one can group the fermions into three generations with similar properties and increasing masses. Only fermions belonging to the first generation (electron and up and down quarks) are the building blocks of matter observed in everyday life. Each fermion has also an anti-matter counterpart. Moreover, quarks come in three and gluons in eight varieties related to their colour charges. Together with W boson having a positive and negative charge, it totals to 61 elementary particle types.

1.1.2 QCD

Quantum chromodynamics QCD is a quantum field theory of strong interactions. It describes the interactions between particles carrying colour charge, namely quarks and gluons. For an in-depth description of QCD refer for instance to [2, 3].

The Lagrangian of QCD is given by:

$$\mathcal{L}_{\mathrm{QCD}} = \sum_{q=1}^{N_f} \bar{\psi}_{q,a}(i\gamma^\mu \partial_\mu \delta_{ab} - g_s \gamma^\mu t^C_{ab} \mathcal{A}^C_\mu - m_q \delta_{ab})\psi_{q,b} - \frac{1}{4} F^A_{\mu\nu} F^{A\mu\nu} \quad , \tag{1.1}$$

where $\delta_{a,b}$ is the Kronecker delta, γ^μ are the Dirac's γ matrices, and Einstein's summation convention for repeated indices is used. $\psi_{q,a}$ is the quark-field spinor for a quark of flavour q and bare mass m_q. $N_f = 6$ is the number of quark flavours. Index a is a colour index running from $a = 1$ to $a = N_c$, where $N_c = 3$ is the number of colour charges (called red, green and blue). t^C_{ab} are the eight 3×3 generators of the $SU(3)$ group. $\mathcal{A}^C_\mu$ are the eight gluon fields (corresponding to $N_c^2 - 1 = 8$ gluons).

The first term in parenthesis is the free quark kinetic term, the second describes quark-gluon interactions, and the third is the quark mass term. Quark interacting with gluon has its colour rotated in $SU(3)$ space.

In the last term $F^A_{\mu\nu}$ is the gluon field tensor, given by:

$$F^A_{\mu\nu} = \partial_\mu \mathcal{A}^A_\nu - \partial_\nu \mathcal{A}^A_\mu - g_s f_{ABC} \mathcal{A}^B_\mu \mathcal{A}^C_\nu \quad . \tag{1.2}$$

It is similar to the QED electromagnetic tensor but contains an additional term. This term (the last one in Eq. 1.2) accounts for the fact that the gluons also carry colour charge and can therefore self-interact via 3- and 4-gluon vertices. Fig. 1.2 shows the three elementary Feynman vertices of QCD.

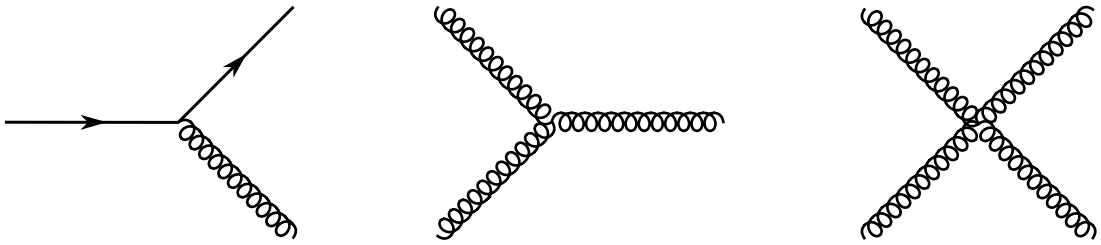

Figure 1.2: Three elementary Feynman vertices of the QCD, describing: quark-antiquark-gluon vertex, three-gluon and four-gluon vertex respectively.

g_s is the QCD coupling constant, related to the strong coupling constant by $\alpha_s = \frac{g_s^2}{4\pi}$. Coupling constant g_s and quark masses m_q are the fundamental parameters of the theory. The value of the coupling constant depends on the energy scale of the interaction. For a given momentum transfer Q^2 it is given by:

$$\alpha_s(Q^2) = \frac{\alpha_s(\mu^2)}{1 + b_0 \alpha_s(\mu^2) \ln \frac{Q^2}{\mu^2}} \quad , \tag{1.3}$$

where $b_0 = (33 - 2n_f)/12\pi$, with n_f being number of quark flavours available at given energies. The equation needs an experimental input of α_s value known at some arbitrary scale μ^2, and it is usually quoted at the mass of Z boson $\mu = M_Z$.

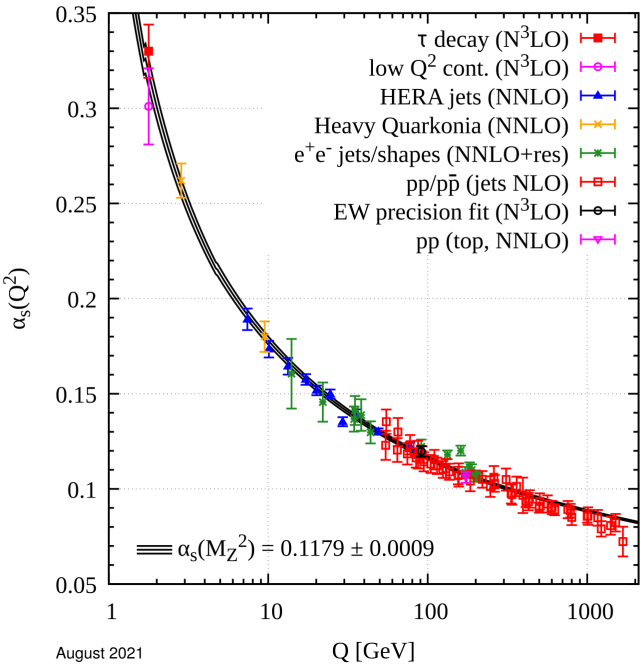

Figure 1.3: Summary of experimental measurements of the strong coupling constant α_s as a function of the momentum transfer Q^2, taken from [4].

Running coupling is a result of the screening from the virtual quark-antiquark pairs and antiscreening from gluons. As the second one dominates, the strong coupling becomes small at short distances (large energy scales) – contrary to QED running coupling. Fig. 1.3 shows α_s as a function of Q. In the limit of high Q^2, α_s tends to zero. This feature of QCD is called *asymptotic freedom* and means that quarks and gluons can exist as free particles at large Q^2. Predictions of perturbative QCD (pQCD) involving expansion only up to the first (second, third, fourth) order of α_s are commonly referred to as Leading Order LO (Next-to-Leading Order NLO, Next-to-Next-to Leading Order NNLO, N^{3}LO). In this regime, perturbation theory provides precise predictions as further terms of the expansion in α_s quickly vanish.

On the other side, when Q^2 is small and α_s becomes $\mathcal{O}(1)$ perturbative approach is no longer valid. One has to turn towards other approaches such as Lattice QCD [4], effective field theories (*e.g.* soft-collinear effective theory [5]) or to phenomenological models. In this regime the interaction between partons becomes strong. A consequence of this behaviour is the *colour confinement* – strongly interacting particles cannot be observed as free and are bounded in the colour-neutral states called hadrons. The strong force grows with increasing distance until it becomes energetically favourable to create a new pair of partons and bind them into hadrons. This process is called hadronization and is one of the poorly understood aspects of QCD, despite knowing its Lagrangian.

1.1.3 QCD factorization

Partons produced in the hadronic collisions are observed in detectors as collimated streams of particles called jets. These particles are created as a consequence of colour confinement. The hadronization process belongs to the non-perturbative regime of the QCD. Also, the initial state of the collision, *i.e.* the partons inside the collided hadrons before the actual interaction are characterized by a small energy scale.

QCD factorization allows for the separation of the various processes involved in the realistic hadronic collision. It preserves the applicability of pQCD to the hard scattering between partons, even if the other stages of the collision cannot be described this way.

The p_{T}-differential production cross section of hadron h in the pp collision can be factorized using the following formula:

$$\frac{d\sigma^{pp\to h}}{dp_{\mathrm{T}}} = \sum_{a,b,c} \int_0^1 dx_1 \int_0^1 dx_2 \int_0^1 dz f_a(x_1, Q^2) f_b(x_2, Q^2) \sigma^{ab\to c+X} D^{c\to h}(z) \ . \tag{1.4}$$

$f_a(x_1, Q^2)$ and $f_b(x_2, Q^2)$ are the probabilities of finding inside the proton a parton which carries $x = p_{\mathrm{parton}}/p_{\mathrm{p}}$ fraction of the proton momentum. They are the so-called Parton Distribution Functions (PDFs). They cannot be computed with pQCD and are obtained empirically from the measurements of deep inelastic scattering (DIS). The PDFs measured at some scale can be evolved to another scale using Dokshitzer-Gribov-Lipatov-Altarelli-Parisi (DGLAP) equations [6–8].

Next term, $\sigma^{ab\to c+X}$ describes the production of parton c in the hard scattering of partons a and b. It is calculable within pQCD.

The last term, $D^{c\to h}(z)$, is the so-called fragmentation function. It describes the probability of obtaining hadron h from parton c, where h carries a fraction z of the parton momentum. This process can be split into two stages: perturbative parton shower and non-perturbative hadronization. The first one is governed by the Altarelli-Parisi splitting functions. The other is in practice described by phenomenological models such as the Lund string model [9].

Note that the given description involves the hadron production cross section. For the jet production cross section, the fragmentation function $D(z)$ should be replaced with some jet formation function. Jets provide a more precise test of pQCD as they are not sensitive to the non-perturbative fragmentation functions.

1.2 Jetography

1.2.1 Jet finding algorithms

Highly energetic partons produced in the hard process cannot be observed directly due to colour confinement. Their properties can be deduced only based on the particles observed in the final state: hadrons and leptons.

Jet finding algorithms are a kind of clustering algorithms that operate on the final state particles. They aim at defining the objects whose properties will reflect the properties of generating them partons. The jet algorithm defines a common surface where theory and experimental perspectives meet. Note that while they are designed to resemble the partons, they yield fundamentally different objects that cannot be directly comparable. One of the requirements placed before the jets from the theory side is to produce a calculable outcome (should yield finite cross sections at any order of perturbation theory). Infrared (IR) and collinear (C) safety are crucial for this. These properties mean that neither very soft emission from a particle nor its collinear splitting should impact the reconstructed jet. From the experimental point of view, the algorithms should be deterministic given a set of particles, robust to experimental distortions such as underlying event (UE) or pile-up, and computationally fast.

LHC measurements are dominated by jet algorithms belonging to the k_{T} family. It is a group of sequential IR and C-safe algorithms. They cluster together particles which are closest according to some distance definition, described in detail below. In the past other algorithms,

belonging to the class of cone algorithms, such as SISCone [10], used to be utilized. For an in-depth review of other jet algorithms refer to [11].

The algorithmic prescription of k_{T} family algorithms is the following [1] :

0. Start with the list of particles in the event and an empty list of jets.
1. Calculate the distances between all pairs of particles:
   $d_{ij} = \min(p_{\mathrm{T}i}^{2p}, p_{\mathrm{T}j}^{2p})\Delta R_{ij}^2/R^2$ with $\Delta R_{ij}^2 = (\varphi_i - \varphi_j)^2 + (\eta_i - \eta_j)^2$
   and *particle-beam* distances:
   $d_{iB} = p_{\mathrm{T}i}^{2p}$.
2. Find the smallest value among d_{ij} and d_{iB}.
3. If it is d_{ij} then combine particles i and j into a new particle and return to step 1.
4. If it is d_{iB} then remove particle i from the list of particles and add it to the list of jets. Return to step 1.
5. Finish when the list of particles is empty.

The three algorithms belonging to this family are called: k_{T} [13, 14], Cambridge-Aachen (CA) [15, 16] and anti-k_{T} [17]. They differ only by the value of exponent p in the distance measure, which is equal to 1, 0 and -1 respectively. It means that the k_{T} algorithm starts by combining the soft particles to their closest neighbours, while anti-k_{T} grows the jets around the hardest particles in the event. CA ignores the information about the particle p_{T} when computing the distances (but not when combining particles). Fig. 1.4 illustrates the clustering performed with these algorithms. The anti-k_{T} is the most popular jet finding algorithm among LHC experiments. Nonetheless, the two others are also used, especially in some specific applications. The k_{T} algorithm is commonly used to measure background jets originating from UE, especially in heavy-ion collisions. Conversely, CA is typically used for reclustering of the already found jets (see Sec. 1.2.2).

All three algorithms are explicitly collinearly safe, as any collinear splitting is merged first due to $\Delta R_{ij} \to 0$ and the situation as if no splitting happened is restored. They are also infrared-safe. The additional soft particle ($p_{\mathrm{T}}^{\mathrm{soft}} \to 0$) in the k_{T} algorithm is clustered first as $d_{ij} \to 0$. For anti-k_{T}, it is either clustered as a last one, to an already well-defined jet, without affecting it ($p_{\mathrm{T}}^{\mathrm{soft}} \ll p_{\mathrm{T}}^{\mathrm{jet}}$) or is not clustered and is a separate jet which is simply dropped.

The k_{T} family of jet algorithms have only two parameters. The first one is the recombination scheme defining how the two particles are combined together. In the E-scheme used in this thesis, their four-momenta are simply added (for other see [18]). The second parameter is the jet radius R, defining the size of the jet on the $\eta - \varphi$ plane. The optimal value of R depends on analysis details. When R increases, the impact of perturbative gluon radiation and hadronization on the jet p_{T} decreases, while the impact of UE increases. The optimal value of R which minimises all these effects tends to grow with jet p_{T}. In practice values of R between 0.2 and 1 are usually selected, with $R = 0.4$ being the most popular choice. In heavy-ion collisions, $R = 0.2$ is also commonly used, in order to reduce the impact of the background. For a longer discussion see *e.g.* [11].

[1] Note that the implementation used in practice is based on the `FastJet` algorithm [12] which allowed for the reduction of algorithmic complexity from N^3 to $N \ln N$ thanks to taking the geometrical instead of combinatorial perspective. Without it, the algorithm was prohibitively slow to be applied in practice.

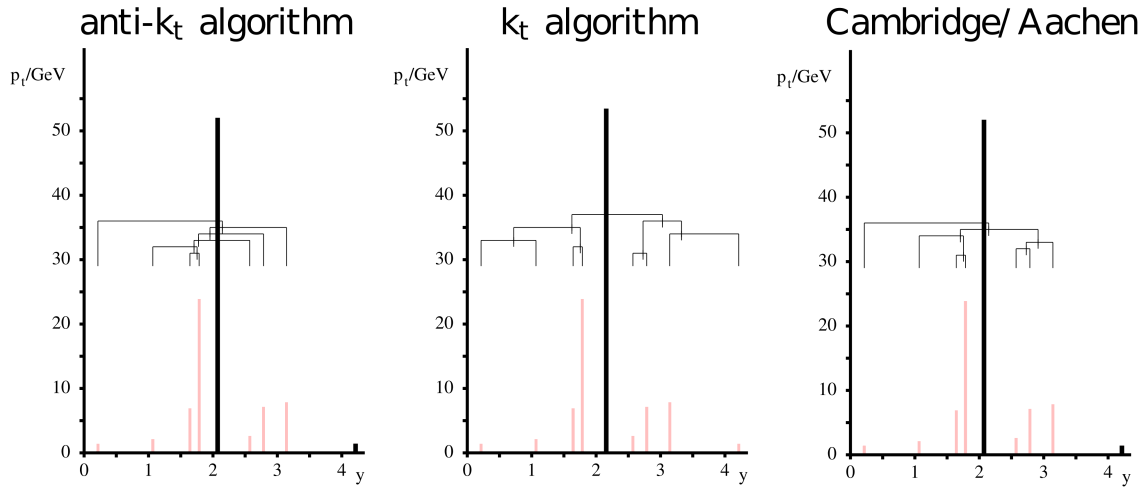

Figure 1.4: Visualization of the sequential clustering of particles into jet [19].

1.2.2 Jet substructure

There is rich information encoded in jets. All the quantities, which take into account the distribution of the particles inside the jet belong to a broad category of jet substructure observables. Their complexity can vary very much. The simplest ones are scalars such as jet angularities [20, 21], which often involve some kind of summation over all jet constituents. They are often referred to as jet shapes. Other variables may yield a distribution for each jet, for instance, one-dimensional radial profiles constructed as a cumulative distribution of a number of particles or their p_{T} as a function of distance from the jet axis. Observable of this type would be also jet images [22]. The most complex observables involve multiple processing stages, such as repeated clustering of jet constituents with different algorithm (usually CA, see following paragraphs) or R (yielding subjets). They can include also jet grooming.

Quantities related to the jet substructure can be used as tools: for tagging of boosted bosons vs. QCD jets or for mitigation of UE or pileup. They may also serve as standalone observables testing theoretical predictions. In the context of QCD, they probe the evolution of the parton shower happening after the hard scattering. It makes them a perfect tool to study the influence of dense medium created in heavy-ion collisions. They are also a good base for applying machine learning (ML) algorithms, thanks to the richness of information they carry. A comprehensive introduction to the jet substructure and review of experimental results can be found in [23–25]. In the following paragraphs, the topics most relevant to this thesis are briefly described.

Jet reclustering Reclustering of the jet refers to the clustering performed only among the constituents of the already found jet. The most common choice of the reclustering algorithm is CA with jet radius R taken as much larger than the original jet radius to make sure that all constituents of the initial jet are also present in the reclustered one. Angular ordering of the CA clustering reflects the angular ordering of the parton shower expected from QCD and is an explicit feature of some generators, *e.g.* HERWIG [26]. It means that reclustering with CA restore the time evolution of the parton shower, which is a very desirable feature.

Reclustering produces the so-called jet tree, which is an alternative representation of the jet and its constituents. It keeps track of the clustering history and not only its final result. Instead of single constituents or subjets the reclustered jet is divided into hierarchical branches or splittings, as shown with the dendrograms in Fig. 1.4. In this description the typical (p_{T}, η, φ) space is replaced with the space of the splitting properties:

- the fraction of p_{T} carried by the subleading prong: $z = \frac{p_{\mathrm{T,subleading}}}{p_{\mathrm{T,subleading}} + p_{\mathrm{T,leading}}}$,
- angular distance between the leading and subleading prongs $R_g = \sqrt{\Delta\eta^2 + \Delta\varphi^2}$,

or other quantities derived from them (in the small angle limit) such as:

- p_{T} of the radiator (from which the emission occurred): $p_{\mathrm{T,radiator}} = p_{\mathrm{T,subleading}} + p_{\mathrm{T,leading}}$,
- relative transverse momentum: $k_{\mathrm{T}} = p_{\mathrm{T,subleading}} R_g$,
- R_g normalized to the jet radius: $\theta_g = R_g / R$,
- k_{T} normalized to the jet p_{T}: $\kappa = z R_g$,
- time-scale of the splitting, called formation time: $t_f \sim 1/z\theta_g^2$;

Note that θ_g, R_g and Δ are sometimes used interchangeably to denote the angular distance between the splittings. g in subscript denotes that the splitting was selected by some grooming procedure, but it may be a splitting index as well. The newly obtained representation can be visualized with the so-called jet Lund plane.

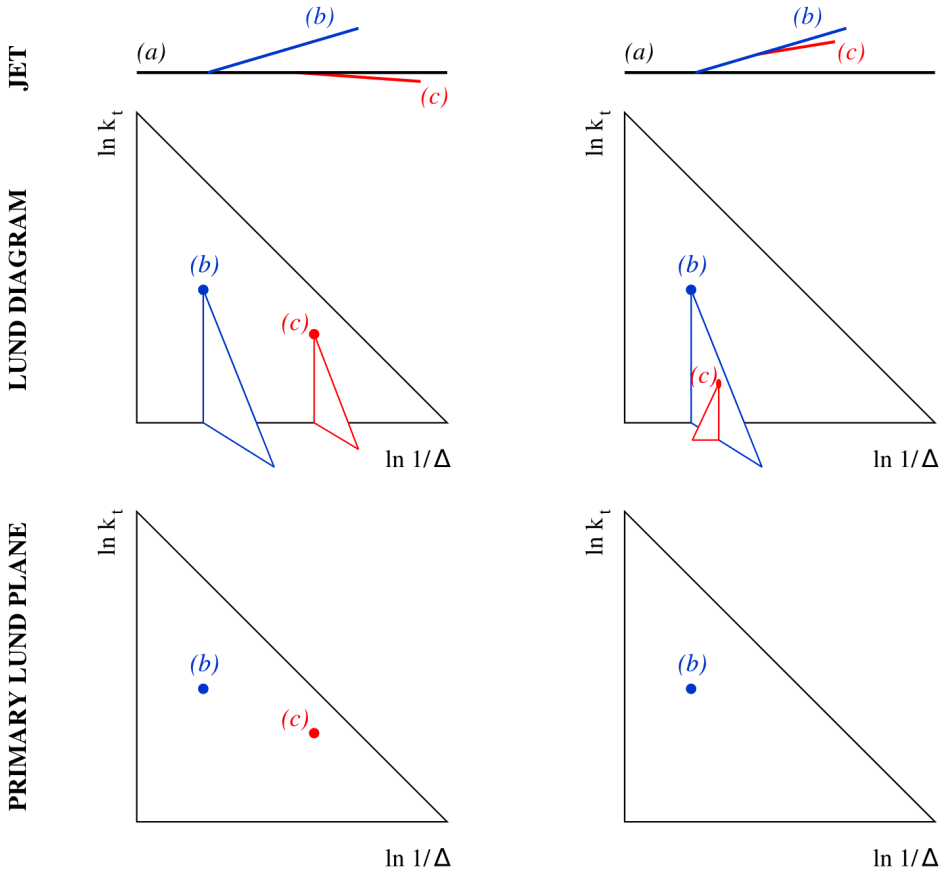

Figure 1.5: Construction of the Lund diagram and the primary Lund plane, taken from [27]. Here, Δ is the same as R_g defined above.

Jet Lund plane The Lund diagram [27] is the representation of the splittings obtained in the reclustering procedure. It exists in various forms, but usually, the horizontal axis corresponds to some function of the θ_g, *e.g.* $\ln(1/\theta_g)$ and the vertical axis to some function of k_T. If the Lund diagram is restricted to the first-order splittings (emissions from the hardest branch of the jet), then the Lund diagram fits on the plane, which is called the (primary) Lund plane, see Fig. 1.5. The history of the single jet can be then read from left to right (assuming the shower obeys angular ordering). Lund plane is then averaged over the sample of jets to obtain the density map normalized to the number of splittings or the number of jets.

Lund plane has interesting theoretical properties, with its various parts corresponding to different parton shower regimes. For instance, the hard, collinear splittings gather close to the boundary restricting the Lund plane from the top right (the boundary corresponds to $z = 0.5$). Non-perturbative effects, such as hadronization, populate the bottom part of the Lund plane.

Lund planes were first proposed as a visualization tool but now are considered also as observables. They were measured already in pp collisions by ATLAS [28], ALICE [29] and CMS [30] (results from ALICE and CMS are preliminary).

Jet grooming Grooming techniques are designed to increase robustness to undesirable experimental or theoretical effects. Grooming may involve the removal of some parts of the jet (usually soft and far from the jet axis) or the selection of a particular structure in the jet (usually one of the splittings in the reclustered jet). For groomers which operate on both of these modes, the second is sometimes referred to as *tagging mode*. Although various approaches exist, here we focus on the grooming variants preceded with the CA reclustering and returning one (or none) of the splittings for each jet. This approach is illustrated in Fig. 1.6. Lund planes for each of the described groomers are shown in Fig. 1.7.

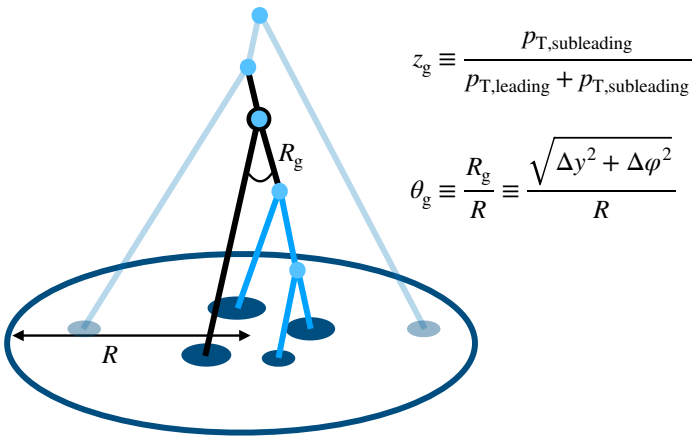

Figure 1.6: Visualization of the jet reclustering and application of groomer, taken from [31].

The groomers relevant to the presented studies include:

- Soft Drop (SD) [32] which is arguably the most popular grooming technique. In its tagging mode, it selects the first splitting which satisfies the soft drop condition (see Fig. 1.6):

$$z > z_{\text{cut}} \left(\frac{\theta}{R}\right)^{\beta} ,$$

  where z_{cut} and β are its parameters. Parameter β is often set to zero, soft drop condition then simplifies to the requirement that the splitting is sufficiently symmetric (z larger

than z_{cut}). For $\beta > 0$, it rejects the splittings which are soft and wide-angle (commonly attributed to UE or pile-up), thus is a usual choice in heavy-ion collisions.

- Dynamical Grooming (DyG) [33, 34] is a single-parameter technique with very good theoretical background. In its tagging mode, it selects the splitting which maximizes the following quantity [2]:

$$h = z\,(1-z)\,\theta^a\,p_{\text{T,radiator}}\ ,$$

where $a > 0$ is the parameter responsible for adjusting the weight of angular dependence. When $a \to 0$ it selects splitting with the highest z, but also has some preference towards the beginning of the shower (where $p_{\text{T,radiator}}$ is the largest). For $a = 1$, it is almost equivalent to selecting the largest relative transverse momentum k_{T}. For $a = 2$ the shortest formation time t_f or highest invariant mass is selected (short formation time corresponds to large angles and thus large mass)

- a set of simple groomers introduced in [35] with self-explaining names: max-z, max-$p_{\text{T}}^{\text{soft}}$, max-$k_{\text{T}}$, max-$\kappa$, min-$t_f$

Note that some of the described groomers yield very similar Lund planes, for instance, DyG with $a = 1$, max-k_{T} and max-κ. All the groomers described here except for SD return always exactly one splitting per jet. SD may not return any splitting if none of them satisfies the grooming condition.

[2] the variables which are constant throughout the shower evolution were removed w.r.t. the equation from original paper as they do not impact maximization

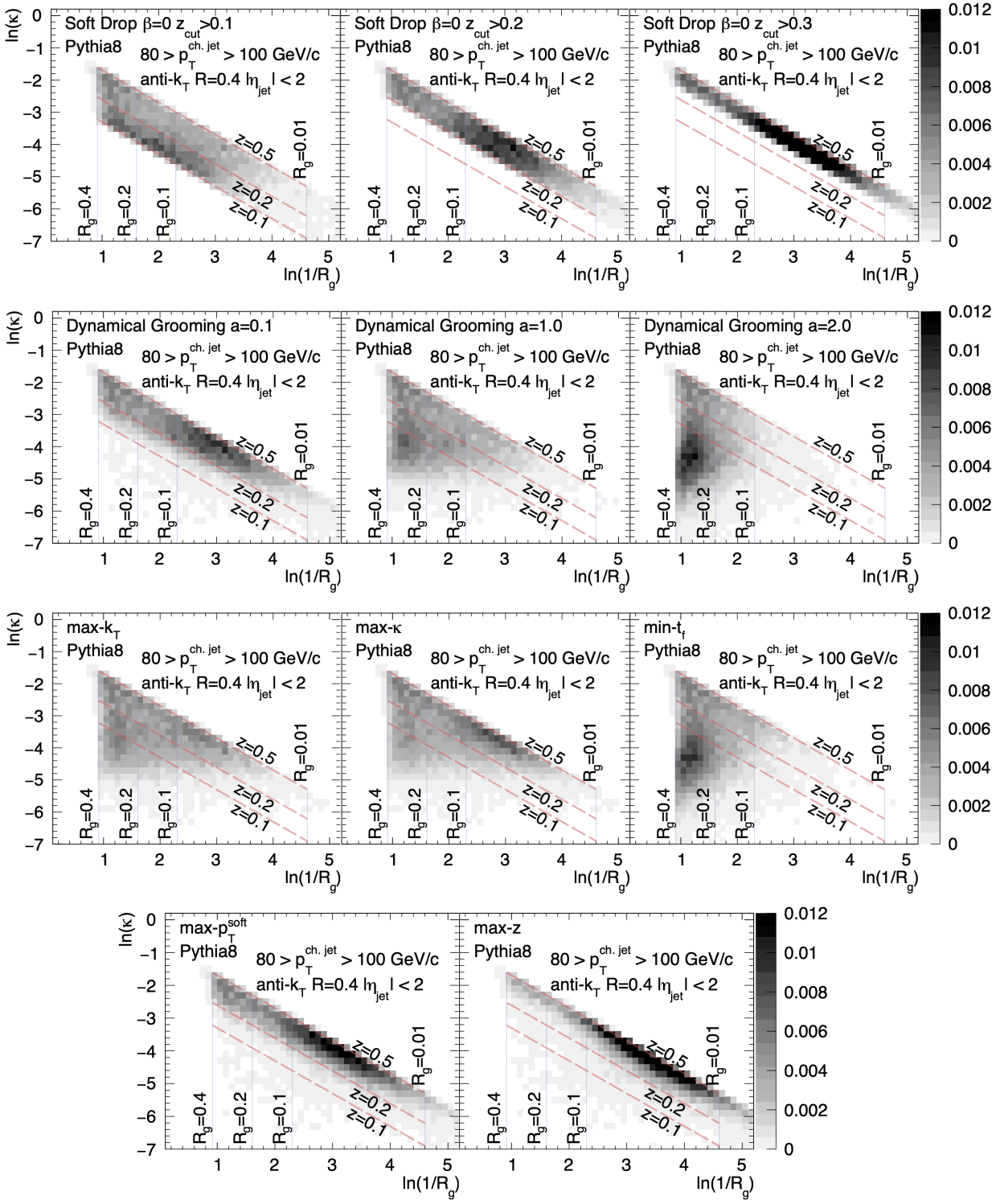

Figure 1.7: Lund planes obtained after applying various groomers on inclusive jets generated with PYTHIA 8, taken from [35].

1.3 Heavy-flavour jets

Heavy flavour (HF) jets are of particular interest for this study. The selection of their properties is described in the next paragraphs.

Production processes heavy flavour (HF) quarks (denoted Q) can be produced in several processes (shown in Fig. 1.8):

- Pair creation (FCR) via quark or gluon fusion, characterized by back-to-back topology
- Flavour excitation (FEX) – when HF quark taking part in hard scattering is a sea quark of one of the hadrons or from prior (initial state) gluon splitting
- gluon splitting (GSP) – when HF quark does not take part in hard scattering but is produced by the parton shower of a gluon. The $Q\bar{Q}$ produced in this process are the most collinear and sometimes may be reconstructed within a single jet

FCR is calculated at LO while FEX and GSP at NLO. CMS measurements of the $B\bar{B}$ angular correlations show that NLO processes dominate at the LHC energies (their dominance increases with p_T) [36].

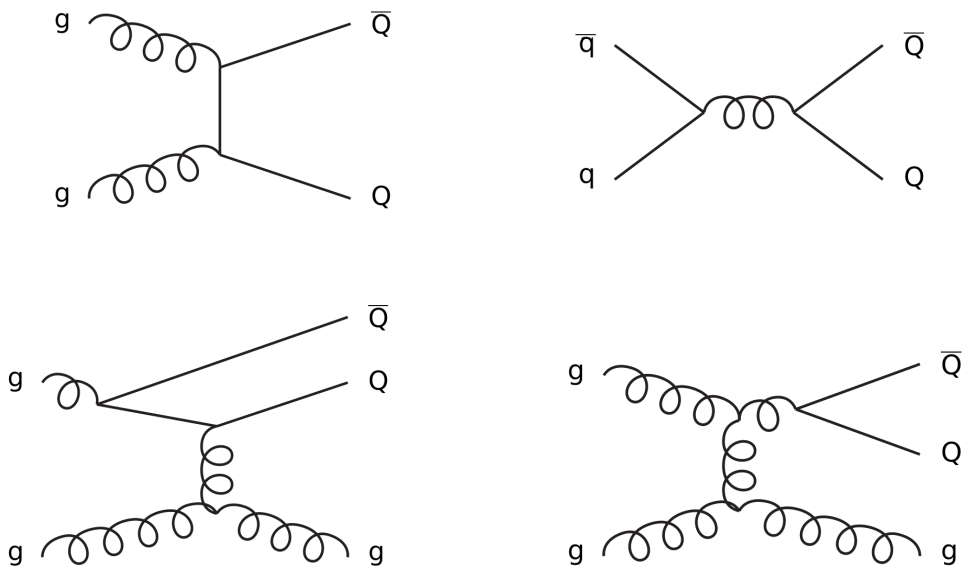

Figure 1.8: Feynman diagrams of processes leading to the production of heavy-flavour quarks: pair creations via gluon and quark fusion, flavour excitation and gluon splitting respectively.

Fragmentation HF jets are expected to undergo much harder fragmentation, *i.e.* more energy is contained in the leading hadron/subjet. Measurements at LEP [37–40] and LHC [41, 42] (see Fig. 1.9) show that the average beauty hadron carries more than 70% of the total jet p_T. The mean z decreases with increasing jet p_T. D^0-tagged jets measured by ALICE [43, 44] show slightly harder fragmentation than the inclusive jets. They have also a smaller number of splittings.

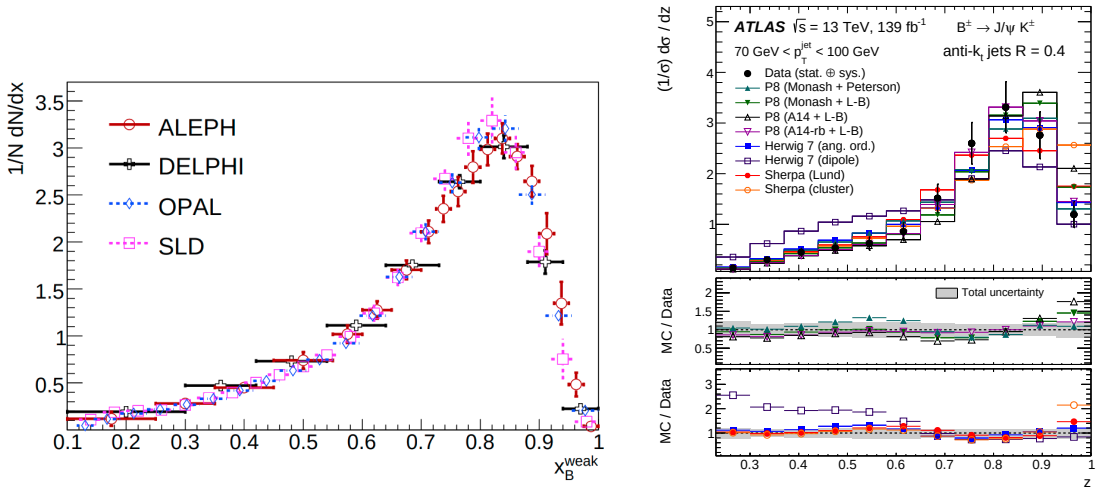

Figure 1.9: Fragmentation function of b-jet carried by the beauty hadron as measured by LEP experiments (left, [37]) and ATLAS (right, [41]).

Dead-cone effect In QCD, the probability for a parton to radiate off a gluon depends on the parton's colour factor and mass. For a massless parton, the probability of emission of gluon with energy ω at angle θ in the infrared and collinear limit is given by:

$$dP(\theta, \omega) = \frac{\alpha_s}{\pi} C_i \frac{d\theta^2}{\theta^2} \frac{d\omega}{\omega} \quad , \tag{1.5}$$

where C_i is the so-called colour factor, equal $C_i = C_F = \frac{4}{3}$ for quark radiator and $C_i = C_A = 3$ for gluon radiator. The value of the colour factor depends on the number of possible combinations of colour flow in the vertex of gluon radiation, which obey colour charge conservation. As gluons carry two colour charges, their colour factor is higher.

For a massive radiator, the formula is modified to:

$$dP(\theta, \omega) = \frac{\alpha_s}{\pi} C_i \frac{d\theta^2}{\theta^2 + \theta_0^2} \frac{d\omega}{\omega} \quad \text{where} \quad \theta_0 = \frac{m_Q}{E} \quad . \tag{1.6}$$

In the small mass limit, it reduces to Eq. 1.5. For a non-negligible mass-to-energy ratio it results in the suppression of radiations at small angles ($\theta < \theta_0$) leading to the appearance of the *dead-cone*.

The dead-cone effect has pronounced consequences on HF physics [45]:

- Suppression of small angle emissions, simultaneously leads to suppression of hard (large z) emissions (z and θ are normally negatively correlated). It leads to the so-called leading particle effect, see Fig. 1.9,
- The multiplicity of splittings in HF jets is smaller than for light flavour quark jets.

Note that a significant challenge with studying the pure mass dependence is that the sample of light flavour jets is a mixture of *uds* and gluonic jets. Their separation is still extremely challenging so in practice, the mass and colour factor effects are usually convoluted. The perfect scenario would be a simultaneous measurement of dead-cone for charm and beauty jets.

Dead-cone effect was for a long time unavailable for direct observation. Then, it was proposed to use for that purpose the iterative declustering applied to jets with fully reconstructed HF hadron [46].

Reconstruction of the HF hadron is a crucial part of this method as it allows for tracking the angles of the emissions from heavy quark throughout the shower evolution. Otherwise, the decay products of the HF hadrons can effectively fill the dead cone.

ALICE simulations with PYTHIA 8 shown in Fig. 1.10 study exactly this effect. It shows the Lund planes for inclusive jets and b-jets with beauty hadron decays switched off and on. When the B mesons are treated as stable, the dead-cone effect is clearly visible when compared with the inclusive jets. However, switching on the decays makes it almost indistinguishable from the inclusive jets.

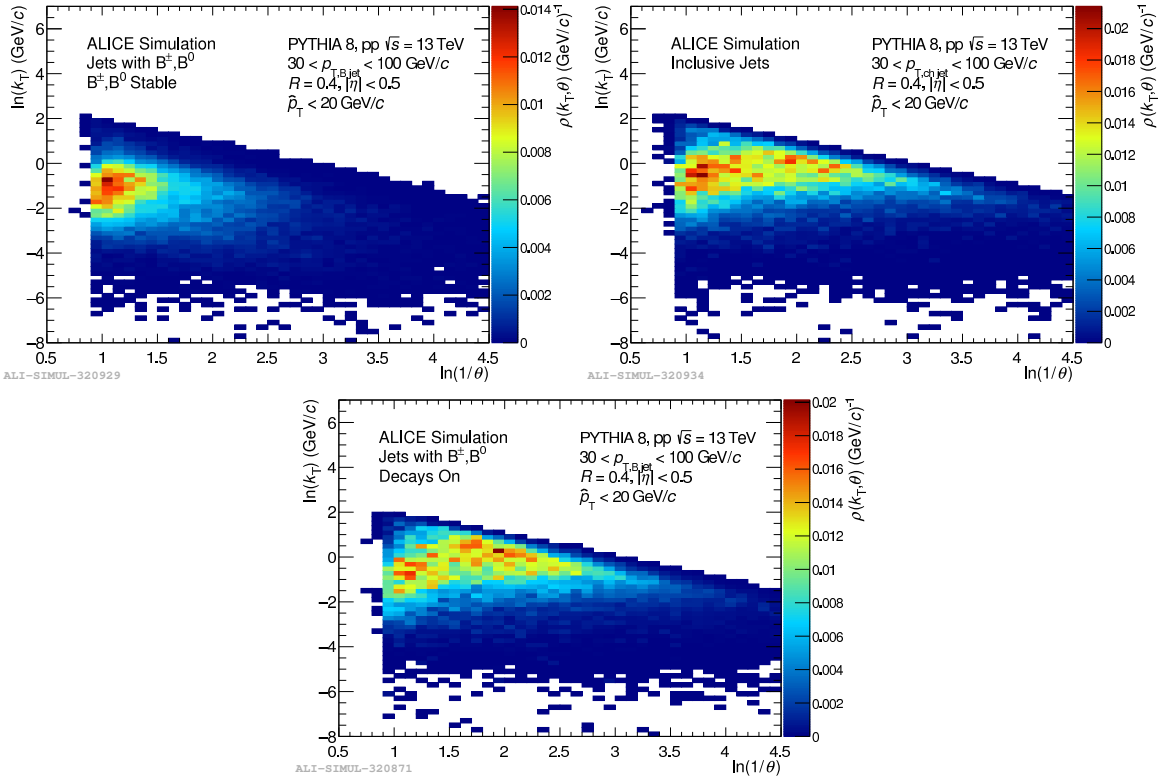

Figure 1.10: Lund planes for b-jets with stable beauty hadron (top left), for inclusive jets (top right) and for b-jets with decaying beauty hadron (bottom). Splittings related to the decay products of B populate the dead-cone region at $\ln 1/\theta \approx 2.5$ and $\ln k_{\mathrm{T}} \approx -1$. Taken from [47].

ATLAS measurement [42] confirms this issue by attributing on average 5 charged particles to the displaced secondary vertex of b-jet. It means that a large fraction of the jet constituents follow the angular distribution characteristic for the decays of beauty hadron instead of the angular structure of a parton shower.

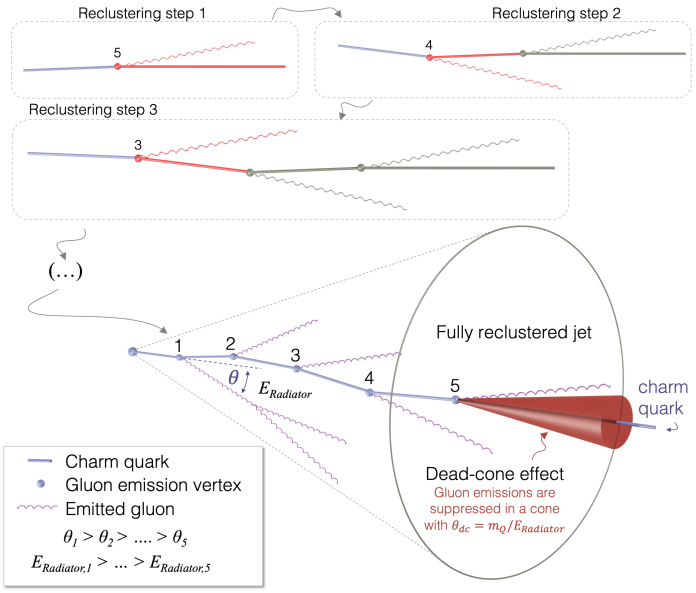

Figure 1.11: Diagram showing the analysis strategy for measurement of the dead-cone effect using iterative declustering technique, taken from [48].

Recently, the dead-cone effect was observed directly for the first time [48], by ALICE using the described technique for the charm jets tagged by D^0 mesons, see Fig. 1.11.

Its result is shown in Fig. 1.12, where $R(\theta)$ is the ratio of splitting angles distribution for the charm and inclusive jets. Only splittings with $k_T > 200\,\mathrm{MeV}/c$ *i.e.* above Λ_{QCD} scale are considered in order to suppress hadronization effects. The measurement shows for charm jets a significant suppression of splittings at $\theta < m_c/E$.

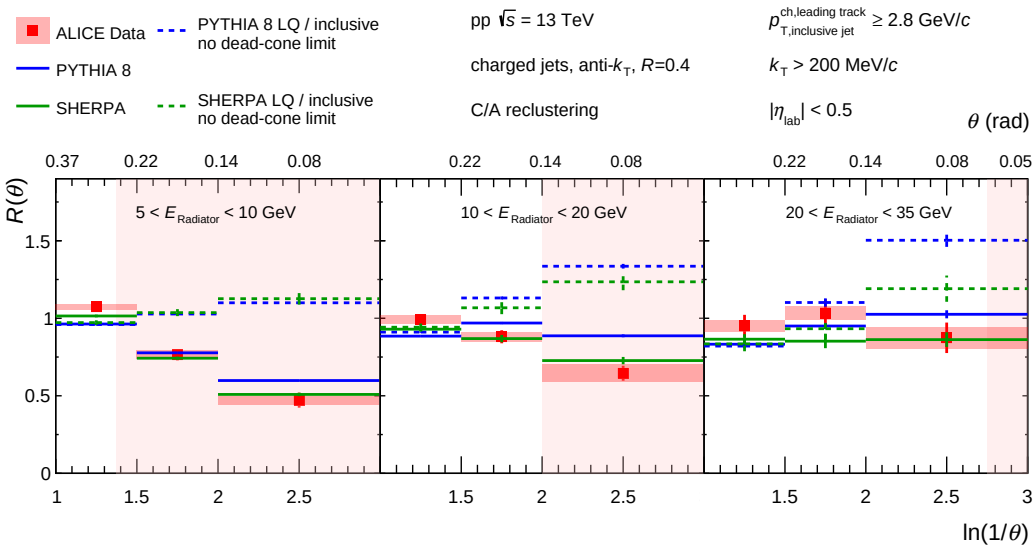

Figure 1.12: Ratio of splitting angle distributions obtained via iterative declustering for the charm and inclusive jets [48]. Shaded areas correspond to the angles smaller than the dead-cone angle θ_0 as expected from Eq. 1.6.

1.4 Quark-Gluon Plasma and relativistic heavy-ion colisions

1.4.1 QGP phase diagram

In the regime of high energies and short distances (low α_s) strong interactions can no longer bind the partons together. For the extremely high temperatures and densities a new state of matter with asymptotically free partons known as quark–gluon plasma (QGP) is postulated. In simpler terms, the matter that usually exists in the form of hadrons is either melted or compressed to densities that are much higher than those found in normal nuclear matter.

Quantities used to describe these conditions are the temperature T and baryon chemical potential μ_B. The distinct phases of matter are described in the form of a phase diagram, shown in Fig. 1.13. A QGP with very low baryon chemical potential is believed to have existed in the first microseconds after the Big Bang. Nowadays, the core of neutron stars may contain QGP at high μ_B and low T. The picture of QCD matter outlined above is being filled with experimental data and theoretical inputs.

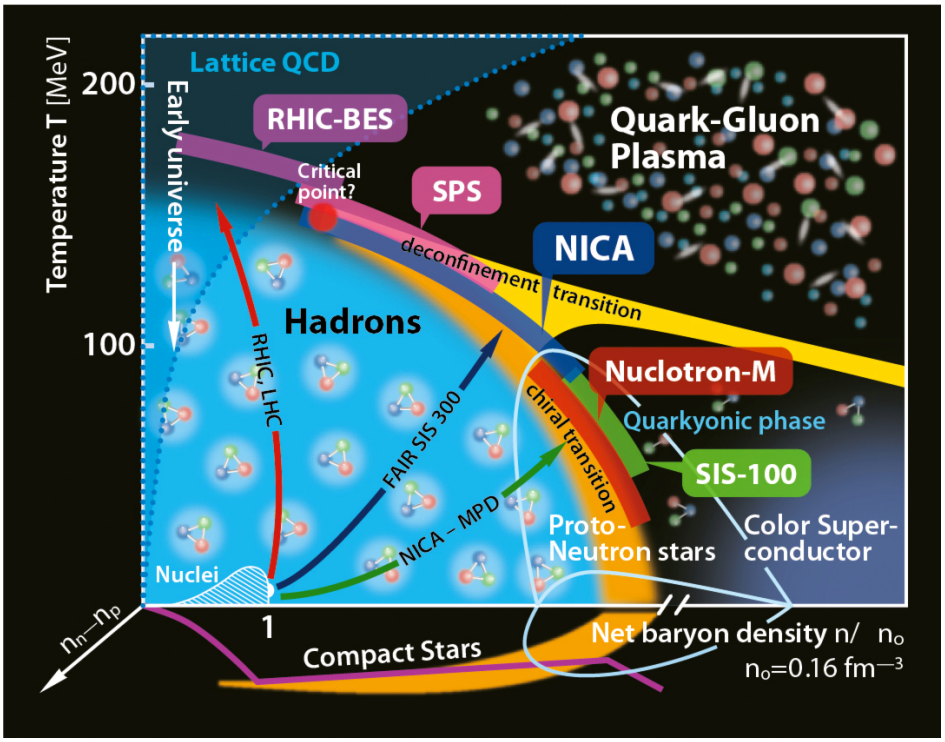

Figure 1.13: Phase diagram of the QCD matter, taken from [49].

A transition from hadronic matter to QGP takes place in the non-perturbative QCD regime. Lattice QCD calculations are applicable in the high T, $\mu_B = 0$ regime. They predict continuous crossover of phases at which the thermodynamic properties of the medium rapidly change as a function of T close to the crossover temperature $T_c \approx 150\,\mathrm{MeV}$ [50]. It includes the normalized energy density (ϵ/T^4) and entropy density $(3s/4T^3)$, which rise is related to the creation of additional degrees of freedom as the partons become deconfined. Other theoretical frameworks indicate that at lower T and higher μ_B the first order phase transition takes place and there should exist a critical point [51, 52]. It has not been discovered yet.

The main experimental tool to study the properties of matter at these extreme conditions are the collisions of ultra-relativistic heavy ions. LHC colliding lead (Pb) ions at the centre of mass energy $\sqrt{s_{\mathrm{NN}}} = 5.02\,\mathrm{TeV}$ and RHIC with its collisions of gold (Au) ions at $\sqrt{s_{\mathrm{NN}}} = 200\,\mathrm{GeV}$ occupy the top left part of the phase diagram, up to $T \approx 3 - 4 \times T_c$. Multiple lower energy facilities such as CERN SPS or future FAIR probe the other parts of the phase

diagram. The QCD critical point searches are performed with the so-called beam energy scans (BES) at SPS and RHIC where beam energy and colliding elements are systematically varied [53].

1.4.2 Experimental probes

There is a plethora of experimental probes used to describe the QGP. For a comprehensive review see for instance [54]. They can be grouped into two broad categories: soft and hard probes.

Soft (low p_{T}) probes generally are used to describe the collective properties of QGP [55]. One prominent example is the measurement of flow. Radial flow is the mass-dependent boost obtained by various particle species and attributed to the common velocity of the expanding medium. Elliptic [56] (and higher order [57]) flow is quantified by the Fourier decomposition of the azimuthal particle distribution. This final state anisotropy is interpreted as an effect of pressure gradient created due to spatial anisotropy in the initial state (as shown in Fig. 1.14). Hydrodynamical models used to describe these phenomena allow to extract the shear viscosity to entropy-density ratio, η/s [58]. It was found to be very small (smallest value ever observed) and close to the theoretical limit of $1/4\pi$ provided by AdS/CFT [59]. It indicates that QGP behaves as a nearly perfect liquid (is strongly coupled and does not resemble a gas). Other soft observables include observations of long-range correlations ("ridge") or enhancement of strangeness production [60].

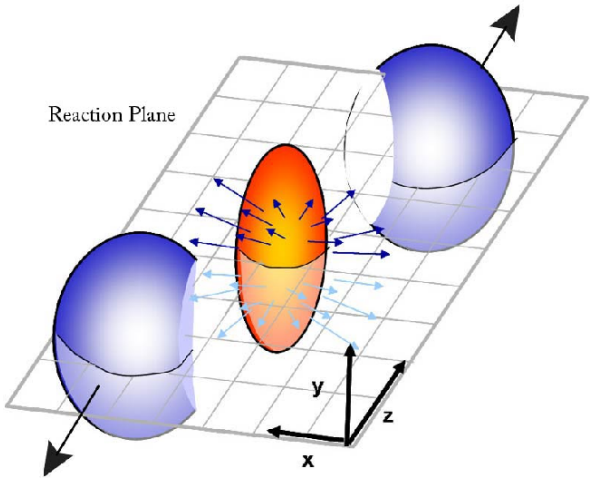

Figure 1.14: Spatial anisotropy in the initial state leading to momentum anisotropy in the final state.

Hard probes are those produced in the high Q^2 process at the beginning of the collision such as jets and HF. They therefore experience full-time evolution of the medium and allow to study how the probes interact with it. For example, quarkonia ($q\bar{q}$ bound states) are expected to meld sequentially according to their binding energy as the temperature increases. Experimentally it is observed as sequential suppression of the quarkonium yield [61].

High-energy partons passing through the QGP lose their energy, which is observed as the so-called jet quenching. It is quantified as a suppression of high p_{T} jets production in heavy-ion collisions with respect to production in pp scaled by number of binary nucleon-nucleon collisions N_{coll}:

$$R_{\mathrm{AA}} = \frac{\mathrm{d}N^{\mathrm{AA}}/\mathrm{d}p_{\mathrm{T}}}{\langle N_{\mathrm{coll}} \rangle \, \mathrm{d}N^{\mathrm{pp}}/\mathrm{d}p_{\mathrm{T}}} \quad .$$

Dijet pairs are observed to be less balanced in Pb–Pb than pp [62, 63] which is attributed to the difference in path length they traverse in the medium.

The distribution of energy inside jets is redistributed, which affects differently jets with different R [64].

Partons traversing the QGP medium lose energy in twofold ways: elastic collisions and radiation of gluons. Expectations for the energy loss differ for various partons. Radiative energy loss is believed to be larger for gluons than for quarks due to a larger colour coupling factor. It should also depend on the quark's mass through the dead cone effect. Collisional energy loss is predicted to be small (but non-negligible) compared to radiative energy loss for light quarks and high energy HF quarks. At lower energies when their velocities are not yet ultra-relativistic, elastic collisions become the dominant energy loss mechanism for HF quarks. Overall, the following ordering is expected $R_{\mathrm{AA}}(g) < R_{\mathrm{AA}}(uds) < R_{\mathrm{AA}}(c) < R_{\mathrm{AA}}(b)$, where lower R_{AA} value denotes larger suppression. It was observed that b-jets indeed lose less energy than inclusive jets (see Fig. 1.15 left). Colour factor dependence was observed for γ-tagged jets (mostly quark-initiated) which lose less energy than the inclusive sample, dominated by gluon-initiated jets (see Fig. 1.15).

Energy loss of the jet depends also on its substructure and the ability of the medium to resolve it. Medium induces additional radiation in the jet [65–67]. If the resolution length of QGP is smaller than the distance between the two subjects, they may act as two separate sources of radiation (decoherence) and lose more energy than in the case of a coherent single source of radiation (expected for narrow jets with less substructure) [68]. It was quantified by comparing jets with different angular scale r_g of first hard (soft-dropped) splitting in Fig. 1.15 (right): jets with two well-separated subjects lose much more energy.

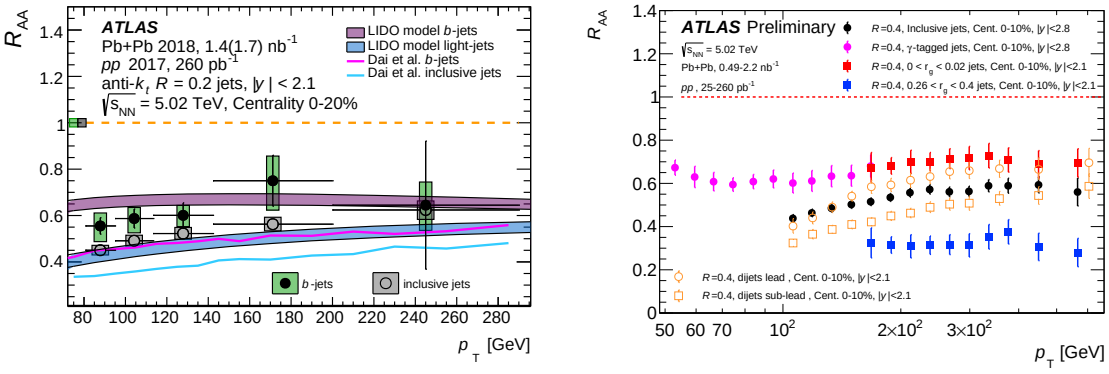

Figure 1.15: Nuclear modification factor measurements from ATLAS [69, 70].

1.4.3 Dead-cone effect in heavy-ion collisions

Preparations for the measurements of the dead-cone effect in the charm and beauty sector in pp collisions are currently ongoing in the LHC experiments. The dead-cone effect can be used also as an interesting probe of QGP properties. The medium-induced gluon radiation is not suppressed inside the dead cone so this region of phase space can be used to separate it from the parton shower typical to vacuum. The dead-cone region can be populated by the medium-induced radiation [71], but it depends on the interplay of angular scales: dead-cone angle θ_0 and medium ability to resolve the splittings (decoherence angle).

Such measurement would be very challenging primarily because of the presence of uncorrelated heavy-ion background which can fill the dead-cone region and is not related to the properties of the medium. For a given density of the background, low p_{T} jets are the ones mostly affected. It is unfortunate because θ_0 drops with the energy and is most pronounced at low p_{T}.

The impact of the heavy-ion medium and background on the jet substructure was studied for the inclusive jets [35, 72]. Little attention has been devoted so far to HF jets. The challenges and methods for removal of uncorrelated background in the context of future dead-cone measurement are discussed in Chapter 4.

Chapter 2

ALICE experiment

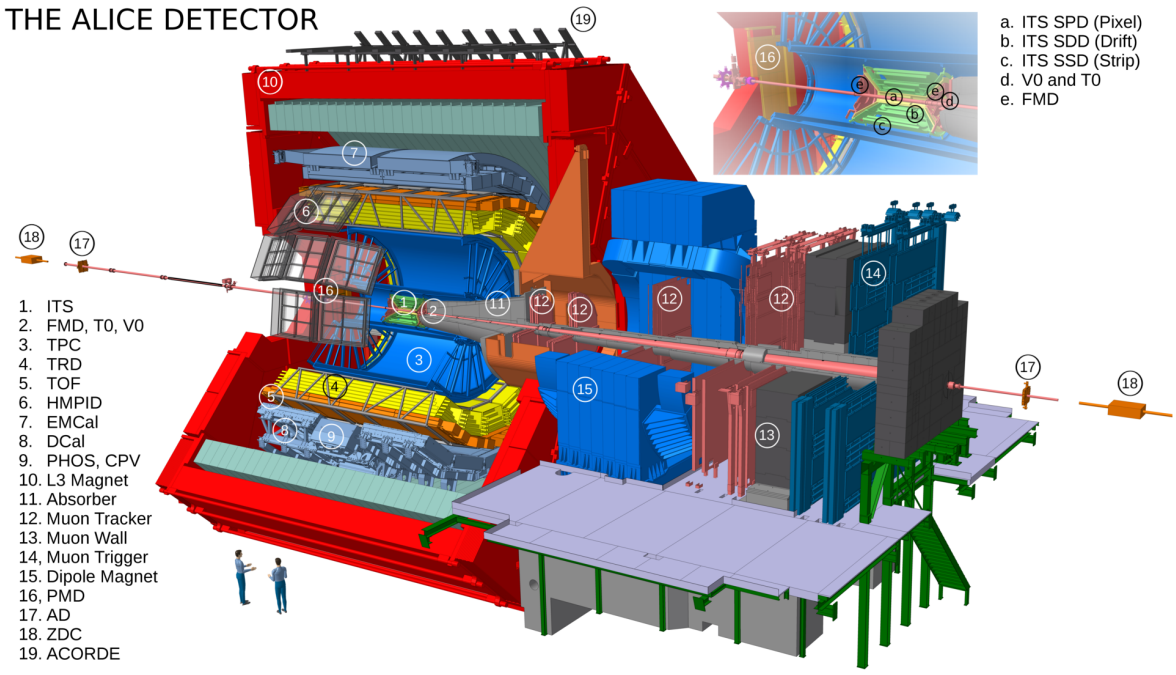

Figure 2.1: Layout of ALICE experiment during Run 2.

A Large Ion Collider Experiment (ALICE) [54, 73, 74] is one of the four largest experiments at the CERN Large Hadron Collider (LHC). ALICE physics program is mostly focused on the studies of the properties of the quark–gluon plasma (QGP). Its main technical objective is tracking a huge number of particles produced in heavy-ion collisions together with particle identification (PID).

ALICE experiment has undergone a thorough upgrade between 2019 and 2022 during LHC Long Shutdown 2 (LHC LS2)[75, 76]. The detector setup described in this chapter corresponds to the apparatus utilized for collecting the data used in this analysis, i.e., the so-called Run 2 of the LHC taking place from 2015 to 2018.

ALICE detection system consists of several detectors, see Fig. 2.1. In general, one can distinguish the following main components of the detector:

- **central barrel detectors:** Inner Tracking System (ITS), Time Projection Chamber (TPC), Transition Radiation Detector (TRD), Time-Of-Flight (TOF), and High Momentum Particle IDentification (HMPID) used for tracking and PID.
  - ITS, TPC, TRD, and TOF are the detectors with full azimuthal angle coverage

  - ITS and TPC are the main tracking and vertexing detectors, also allowing for the identification of particles based on their specific energy loss. They are described in detail later in the thesis
  - TRD is located at the outer boundary of the TPC. Each TRD module consists of a radiator and a multi-wire proportional chamber. It extends PID capabilities of ALICE in e/π separation at $p_{\mathrm{T}} > 1\,\mathrm{GeV}/c$ – electron passing through the radiator layer emits an additional, so-called "transition" photon, which modifies the shape of the signal produced by electrons compared to pions.
  - TOF is a precise time-of-flight detector with a resolution of 50 ps. One can deduce the particle's mass by combining track momentum (from its curvature) and velocity provided by TOF. TOF can operate in a regime where particle velocity is still distinctly below the speed of light. Therefore it is utilized for π/K and K/p separation up to p_{T} of a few GeV/c and is very useful in analyses of light nuclei. Thanks to its low noise, TOF is also used as a trigger for cosmic rays (for calibration or in specialized physics analyses).
  - HMPID is Ring imaging Cherenkov (RICH) detector enhancing ALICE PID capabilities at high momenta. It covers only 5% of the central barrel phase-space

- **electromagnetic calorimeters:** PHOton Spectrometer (PHOS), Electro Magnetic Calorimeter (EMCal), Di-Jet Calorimeter (DCal), located at central rapidity but covering limited azimuthal angle. They provide ALICE with capabilities in measuring direct photons, neutral mesons ($\rightarrow \gamma\gamma$), electrons, and jets, including their neutral component. Highly granular PHOS reaches better energy and spatial resolution, whereas EMCal-DCal pair has higher acceptance and, thanks to its location on the opposite sides of the interaction point, allows for dijet measurement. EMCal can serve as a fast-triggering detector.

- **the muon spectrometer arm:** located at the C-side, consisting of the hadronic absorber, dipole magnet, tracking stations, and triggering chambers. It measures heavy-quark resonances: J/ψ, ψ(2S), Υ(1S), Υ(2S), Υ(3S) via their decay to $\mu^+\mu^-$ pair. A set of filters stops any particles except the muons, making this channel very clear. Achieved mass resolution is sufficient to separate all of the above-mentioned states.

- **a set of specialized forward detectors:** ZDC, PMD, FMD, V0, T0, which serve multiple purposes. First, they provide minimum bias and centrality triggers (V0, T0, ZDC), while rejecting background from beam-gas events (T0, V0). Secondly, they measure global event characteristics, such as collision time (passed as start time to TOF) and vertex position along the beam axis (T0). In the heavy-ion collisions, the list of properties is supplemented by event centrality (V0, ZDC, T0, PMD) and reaction plane (V0, FMD, ZDC, or PMD). Finally, V0 and T0 are used to determine luminosity based on measurements of visible cross section in the van der Meer scans [77].

2.1 Tracking detectors

2.1.1 ITS

Inner Tracking System [79] is a silicon detector located at the heart of ALICE, closest to the interaction point (IP). It consists of 6 cylindrical layers located at a radial distance from 3.9 to 43 cm. For the vertices located within 1σ (5.3 cm) along z from the nominal interaction point, it covers the pseudorapidity range of $|\eta| < 0.9$. The layout of ITS is presented in Fig. 2.2.

Each of the three pairs of layers was manufactured with different technology. These are, starting from the innermost, Silicon Pixel Detectors (SPD), Silicon Drift Detectors (SDD), and

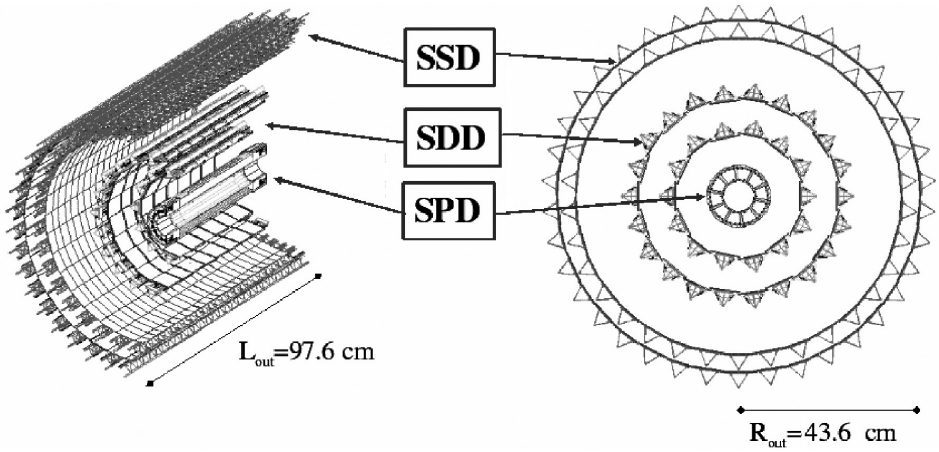

Figure 2.2: Drawing of the Inner Tracking System [78].

Silicon micro-Strip Detectors (SSD). This design reflects the need for keeping the occupancy at the level of a few percent for the density of particles varying from 50 particles per cm^2 for the inner layer of SPD to below one particle per cm^2 for SSD. SDD and SSD have an analog readout, which provides a wide dynamic range required for identifying low momentum highly ionizing particles via dE/dx. ITS can be thus used as a standalone tracker and spectrometer of low-momenta particles (below 200 MeV).

Its main objectives are precise ($\sigma < 100\,\mu m$) localization of primary vertex and improvement of TPC angular and momentum resolution. Precise primary vertex position determination is a prerequisite to the reconstruction of secondary vertices from decays of hyperons (typical $c\tau$ of 10–100 mm), charm ($c\tau$ ~0.1 mm) and beauty hadrons ($c\tau$ ~0.5 mm). ITS provides six additional points for tracking in the critical region close to the interaction point. Its impact on the momentum resolution is shown in Fig. 2.8. ITS also fills the gaps in the dead areas of the TPC.

2.1.2 TPC

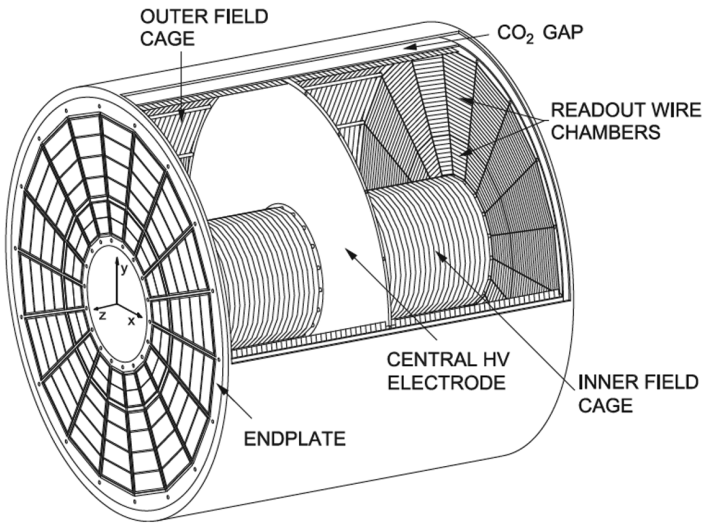

Figure 2.3: Drawing of the Time Projection Chamber [80].

Time Projection Chamber, presented in Fig. 2.3, plays a crucial role in tracking and PID. It is a detector of cylindrical shape having an overall length of 5 m and inner (outer) radius of

85 (250) cm [81]. It is located symmetrically along the beam pipe with the interaction point at its centre. TPC is composed of a field cage and readout chambers located close to the end plates and is filled with a carefully chosen mixture of gases. Field cage consists of a central anode set to a voltage of $-100\,\mathrm{kV}$ and cathodes on both ends set to $0\,\mathrm{V}$, which results in the uniform electric field of $400\,\mathrm{V/cm}$ directed parallel to the beam pipe and pointing towards the central electrode.

The charged particle traversing the volume inside the TPC interacts with the gas molecules, excites and ionizes them, see Fig. 2.4. Electrons start to drift towards cathodes, where they are multiplied in the multi-wire proportional chambers and read out. The readout chambers are normally closed, and they open only after receiving a signal from the L1 trigger ($\sim$6.5 µs after the collision) for a duration equal to the drift time of electrons. The transverse (x, y) coordinates of the track can be accessed via the position of the induced signal on the readout chamber, while the z component is calculated based on its drift time. This allows for the 3D reconstruction of the tracks of charged particles. Another piece of information, namely the amplitude of the signal, is translated into energy loss of the particle, which is type-specific and, together with knowledge of the momentum (based on the track's curvature), allows for its identification.

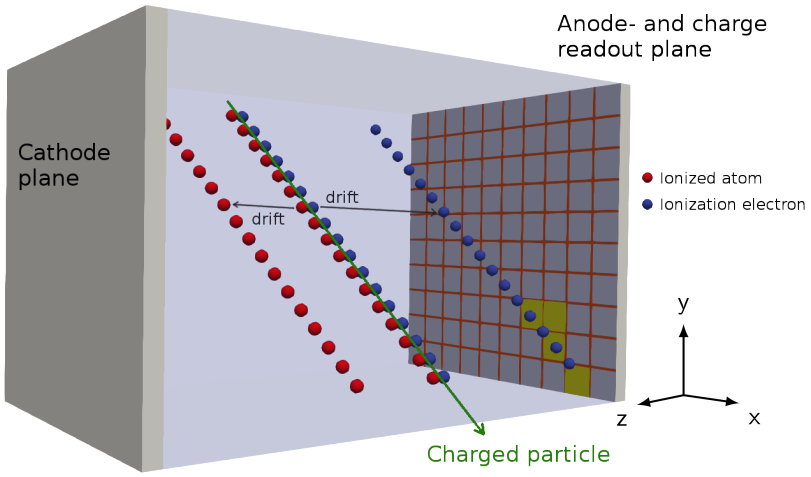

Figure 2.4: Working principle of the TPC as a detector capable of tracking particles in 3D.

The final composition of gas filling the volume of TPC is a result of careful optimization in terms of electron drift velocity, diffusion coefficients, ionization rate, density, aging, stability, and many other parameters, including those not related to measurement precision such as price and safety (inflammability, toxicity, radioactivity) [82]. Drift time and thus drift velocity v_D is a limiting factor for the dead time of the detector, therefore, it needs to be kept as low as possible. For achieved values of $v_D \approx 2.7\,\mathrm{cm/\mu s}$ the electron drift time equals $\tau_D \approx 92\,\mu\mathrm{s}$. Ions, much slower than electrons due to higher mass, stay longer in the gas volume. Their presence is observed macroscopically as a space-charge that distorts the drift paths of the ionization electrons Hence, high ion mobility is another desired feature. Ionization rate (number of electron-ion pairs created per unit length) should be neither too large nor too small – on one hand, high values improve spatial resolution and $\mathrm{d}E/\mathrm{d}x$ precision, on the other, they magnify the effect of space charge and increase occupancy. Finally, low gas density aims at reducing the number of scatterings undergone by charged particles traversing the gas over a long distance inside TPC. The gas mixture used in the LHC Run 2 was $\mathrm{Ar/CO_2}$ (88/12). Admixture of $\mathrm{CO_2}$ is beneficial due to its quenching properties (it absorbs photons emitted by excited noble gases like argon). ALICE TPC operates at room temperature and atmospheric pressure. In order to preserve good performance, gas parameters have to be maintained with the precision of

$\Delta T < 0.1\,\mathrm{K}$ and $\Delta p < 0.4\,\mathrm{mbar}$. It is a consequence of the steep dependence of drift velocity on these parameters. Moreover, contamination from other gases, most commonly oxygen (and water), has to be kept at the level of 1-2 ppm due to their tendency to attach electrons and consequently attenuate signal. Obtained drift time restricts the maximum trigger rate for Pb–Pb collisions to several kHz.

TPC is divided into 18 azimuthal sectors, each one having one inner and one outer readout chamber at each of the end plates, totalling 72 chambers. The chambers are split into pads, arranged into 159 rows, which is the maximum number of clusters, which can be produced by one particle trajectory of full length (with matches in both ITS and TRD). A total number of pads (channels) of 557 thousand keeps the (space-time) occupancy for collisions with $\mathrm{d}N/\mathrm{d}y \approx 8000$ at the level of 40% for the inner and 15% for the outer radius. For pp collisions, occupancy is below 0.1%. The number of $\mathrm{d}N/\mathrm{d}y \approx 8000$, which was used during the design of ALICE, was based on the early estimates, prior to the data collected by experiments at RHIC. The actual value of $\mathrm{d}N/\mathrm{d}y$ at midrapidity obtained in ALICE is close to 2000 [83], which gives ALICE a large safety margin, even for the most central Pb–Pb collisions.

The TPC can track charged particles in a wide range of momenta from 0.1 to $100\,\mathrm{GeV}/c$ with good momentum resolution. TPC covers full azimuthal angle (except the dead regions between the sectors, which account for approximately 10% of acceptance) and pseudorapidity range of $|\eta| < 0.9$. Using solely the Inner Readout Chambers (IROC), which cover around 1/3 of the radial size of TPC, allows tracing particles with reduced track length (and therefore resolution) within the extended rapidity range of $|\eta| < 1.5$.

The obtained position resolution depends on the three main factors, namely: drift length, track inclination angle, and charge deposited on the anode wire. For higher momentum tracks produced close to the nominal interaction point (which have a small inclination angle), the space point resolution is below 1 mm in both z and $r\varphi$ directions [81].

Identification of particles in TPC based on their specific energy loss which is fitted with Bethe-Bloch formula [84]. The distribution of the deposited energy follows Landau distribution, in which moments, like mean value, are undefined. In practice, it means, that the simple average is subject to large statistical fluctuations. It forces the usage of the so-called truncated mean approach, where the mean is calculated based on the lower 60% of the distribution (the upper 40% containing the "fat tail" is dropped). $\mathrm{d}E/\mathrm{d}x$ resolution of the TPC is around 5.5% at lower and 6.8% for higher multiplicities, with some dependence on the number of clusters and track η. The ability to distinguish between two particle species depends on the considered species and track momentum. In general, for lower momenta, up to $1–2\,\mathrm{GeV}/c$, one can do it track-by-track, while at higher momenta, in the regime of relativistic rise, the number of particles of each species can be determined on the statistical basis. Achieved separation power is by design complementary to that of other detectors. The wide energy loss dynamic range of the TPC allows it to identify also light nuclei, like deuterons, tritons or ^{3}He.

2.2 Track and primary vertex reconstruction

Reconstruction of tracks and primary vertex (PV) is performed in the common iterative procedure, pictured in Fig. 2.5 [74].

First, clusterization (grouping of points close in space and time) is performed for each detector separately. In the case of TPC, cluster position is calculated based on the center of gravity of the two-dimensional (time and position along pad-row) distribution of the signal.

In the next step, the first estimate of the primary vertex position is calculated. It considers only hits in the SPD detector (first two layers of ITS). Points close by in azimuthal angle are connected with straight lines (neglecting tracks curvature) and the space point intersected by the highest number of such tracklets is assumed to be PV. If such a point is not found,

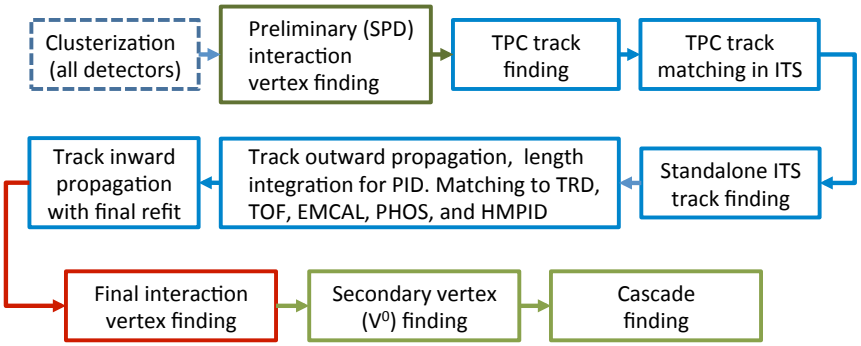

Figure 2.5: Scheme of the track and vertex reconstruction workflow in ALICE.

usually in low multiplicity collisions, then an alternative algorithm performing a scan along the z direction is executed. Due to its speed, it is also the default choice in Pb–Pb collisions.

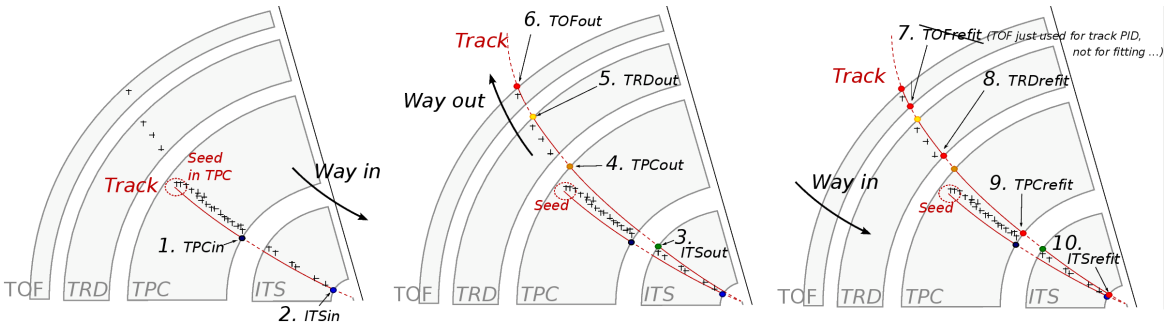

Figure 2.6: Illustration of iterative procedure of track fitting.

Track reconstruction in the central barrel is performed in several stages as illustrated in Fig. 2.6. It utilizes the Kalman filter approach [85] – an iterative procedure that updates track parameters and its covariance matrix after the addition of each new point. It naturally allows for the evolution of track parameters due to energy loss and scattering in gas. In the first stage, track seeds required by the Kalman filter are built at the outer radius side of the TPC, where the cluster density is the smallest. They consist either of two clusters and the SPD vertex or three clusters without vertex constrain in order to include also secondary tracks [1]. Seeds are propagated towards ITS adding one cluster (one TPC row) at a time. The maximum number of clusters assigned to the TPC track is 159. Until this moment almost 100% of potentially findable tracks (traversing at least half of the TPC and outside dead areas) are reconstructed. At this point, preliminary PID based on $\mathrm{d}E/\mathrm{d}x$ is done in order to compute ionization energy loss correction for further tracking steps.

TPC tracks reconstructed in the first stage are used as seeds for track finding in ITS, starting from the highest momenta. For each track, multiple path hypotheses may be considered and then filtered based on the track quality. The efficiency of this procedure is at the level of 95% when at least 2 hits in ITS are produced by the particle and drops to 80–85 % if at least 1 hit in SPD is required.

Very low p_{T} tracks which cannot be reconstructed in TPC due to their energy loss are reconstructed in ITS alone based on the clusters left after TPC-ITS matching. This procedure recovers also high p_{T} straight tracks, which fall into inactive areas between TPC sectors.

[1] products of weak decays or originating from interaction with detector material, for precise definition see [86]

After the first inward step, the search for so-called *kinks* takes place in TPC. These are tracks characterized by a sharp change of direction, which is a signature of charged particle decaying into one charged and one neutral particle, *e.g.* $\mathrm{K}^{\pm} \to \mu^{\pm}\nu$, $\mathrm{K}^{\pm} \to \pi^{\pm}\pi^{0}$ or $\pi^{\pm} \to \mu^{\pm}\nu$.

All tracks found so far are extrapolated to PV, where the second pass, this time outwards, starts. Tracks are refitted using the clusters found in the previous stage and an attempt to eliminate improperly assigned clusters is made. Then the tracks are matched to the tracklets reconstructed in detectors outside TPC: TRD, TOF as well as EMCAL, PHOS and HMPID. Finally, tracks are propagated once again inwards, starting from outer TPC clusters to determine the ultimate values of track parameters close to their production vertices.

After track reconstruction, the primary vertex is recalculated using more precise tracks measured in TPC and ITS. Tracks are extrapolated to the beam line, and fitted with weighted χ^2 fit from which outliers and tracks with less than 3 hits in ITS are excluded. Vertex position resolution depends critically on the number of contributing tracks. In order to improve it in low multiplicity events, the nominal luminous region (average vertex position over many events) is added as a constraint – it is equivalent to adding to the fit an additional point with a resolution equal to the size of the luminous region in xy plane. In Pb–Pb only one vertex is reconstructed. In pp or p–Pb where significant pile-up is expected, multiple vertices are found in the iterative procedure in which only tracks from the same bunch crossing (based on information from TOF) are allowed to contribute to the same vertex.

The event reconstruction is finalized with the search for V^0 candidates and cascades. V^0 candidates are pairs of tracks with opposite signs and large distance of closest approach (DCA) to PV. Their search aims at the reconstruction of neutral particles decaying to pair of charged ones, like $\mathrm{K}^0_{\mathrm{S}} \to \pi^+\pi^-$, $\Lambda \to \mathrm{p}\pi$ or $\gamma \to \mathrm{e}^+\mathrm{e}^-$ (photon conversions). For each such pair, the point of closest approach (PCA) is computed. Tracks are then required to be close to their PCA and have no clusters in front of the PCA (clusters closer to PV than PCA). A similar procedure is performed on V^0 candidates with a reconstructed mass close to m_Λ matched with the secondary track in order to reconstruct cascades $\Xi \to \Lambda\pi \to \mathrm{p}\pi\pi$.

2.2.1 Tracking performance

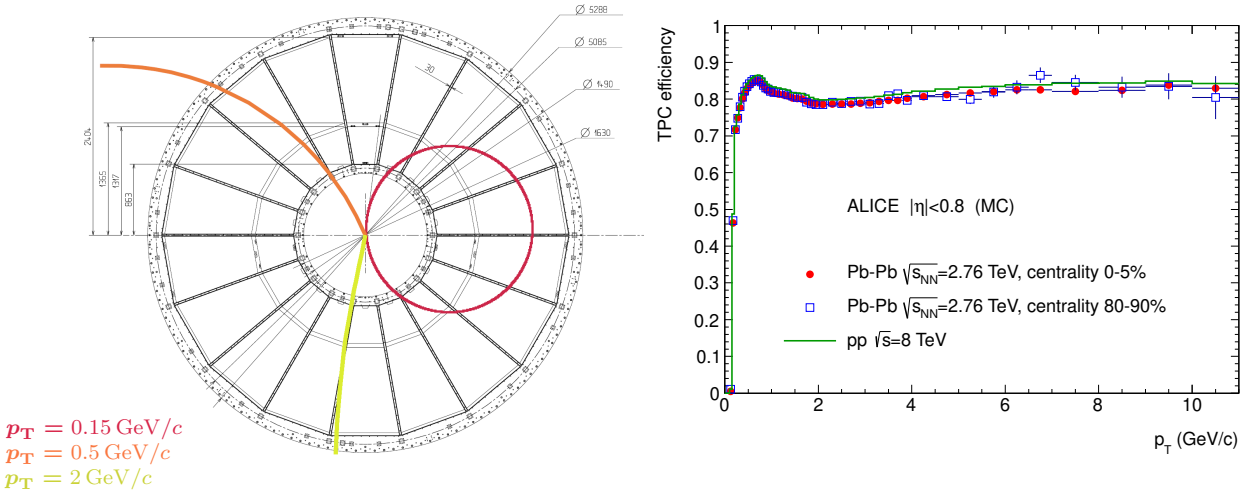

Figure 2.7: Trajectories of particles with different p_{T} overlaid with TPC size (left) and plot of the TPC tracking efficiency (right).

As described in previous paragraphs detector setup and procedures allows for precise tracking of charged particles produced in collisions of systems characterized by very different multiplicities. Fig. 2.7 (right) shows TPC tracking efficiency achieved by ALICE in pp and Pb–Pb collisions, which does not depend on the detector occupancy (is equal for both systems). A sudden drop of efficiency below transverse momentum of $\sim 0.5\,\mathrm{GeV}/c$ originates from large energy loss of low p_T particles interacting with detector material. The nonmonotonic behaviour at higher p_T is related to various impacts of dead areas between TPC sectors for particles with different p_T (curvature) as illustrated on 2.7 (left). The higher the p_T the smaller chance that the particle will encounter the sector boundary, but the larger is its impact in such a case. Every low p_T track traverses multiple sectors and therefore its detection efficiency is not affected by dead areas in between. Mid p_T track of $0.5\,\mathrm{GeV}/c$ will loose small fraction of its detectable clusters, but will manage to escape any dead area it could encounter. The efficiency dip around $p_\mathrm{T} = 2\,\mathrm{GeV}/c$ corresponds to the particles whose large part of the trajectory may belong to the dead area and the fraction of particles which are affected is larger than for completely straight tracks of high p_T particles which fit entirely either within or between sectors boundaries.

Table 2.1: Inverse transverse momentum resolution σ_{1/p_T} from Fig. 2.8 translated to relative momentum resolution $\sigma_{p_\mathrm{T}}/p_\mathrm{T}$ for TPC standalone tracks and tracks matched to ITS.

p_T (GeV/c)	σ_{p_T}/p_T [%]	
	TPC s.a.	TPC+ITS
1	0.8	0.8
2	1.5	0.8
10	6	2
50	30	5

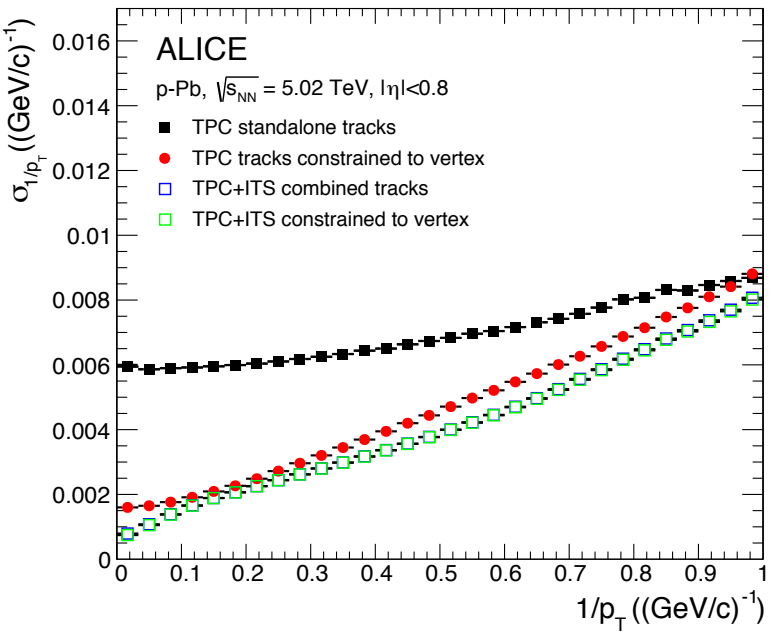

Figure 2.8: Inverse transverse momentum resolution (σ_{1/p_T}) for different reconstruction schemes.

Fig. 2.8 shows the inverse transverse momentum resolution σ_{1/p_T} as a function of $1/p_\mathrm{T}$ and Tab. 2.1 lists the same values translated to p_T and σ_{p_T} using relation $\sigma_{p_\mathrm{T}}/p_\mathrm{T} = p_\mathrm{T}\,\sigma_{1/p_\mathrm{T}}$.

This comparison demonstrates the importance of constraining tracks close to the interaction point either with vertex position or (preferably) using ITS. Having such constraint, ALICE can reconstruct p_{T} of the tracks with satisfactory resolution $\lesssim 5\%$ in a wide range of transverse momenta from 1 to 50 GeV/c.

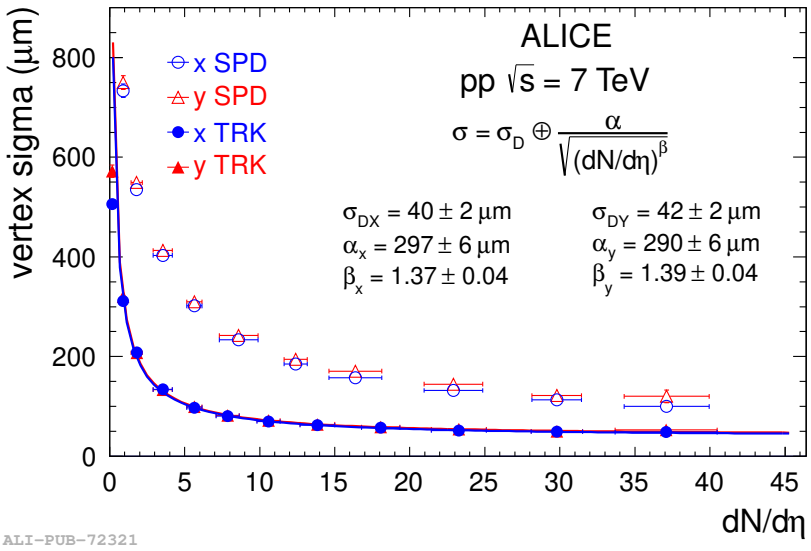

Figure 2.9: Width of the transverse vertex distribution (σ) of the preliminary, SPD and final vertex obtained after full track reconstruction. Final vertex σ is a convolution of luminous region size σ_D and vertex resolution.

Fig. 2.9 shows the resolution of the primary vertex as determined at the beginning of event processing using only SPD tracklets and using fully reconstructed tracks at the end. Resolution below 100 μm is achieved already for an average in terms of event multiplicity in minimum bias (MB) pp collision ($\langle \mathrm{d}N/\mathrm{d}\eta \rangle_{pp\,\mathrm{MB}} \approx 7$) [87].

The precision of the vertex position determination impacts track DCA resolution, shown in Fig. 2.10. In general, DCA resolution drops steeply with track p_{T} and slightly with event multiplicity. Contribution from the vertex position uncertainty dominates for higher p_{T} tracks, especially at lower multiplicities.

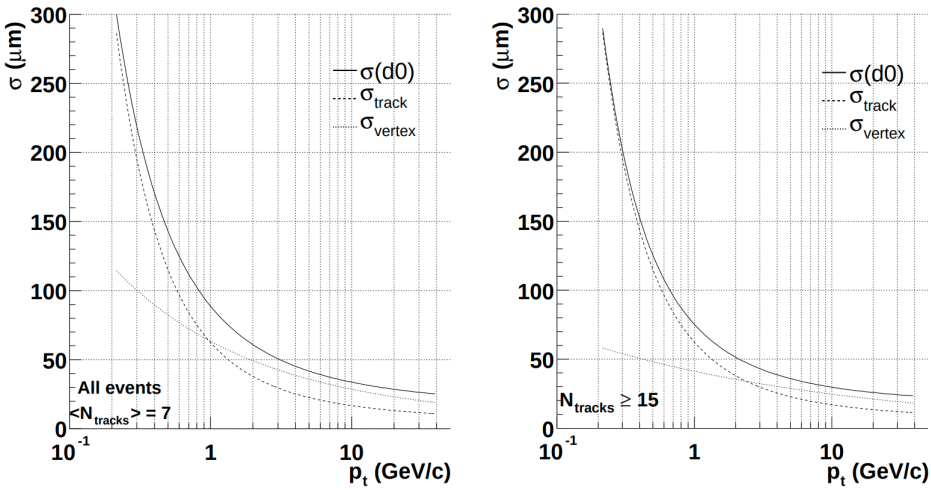

Figure 2.10: Track DCA resolution in transverse plane as a function of track p_{T} decomposed into contributions from PV and track itself. DCA resolution is different for different particle species and for given p_{T} is better for lighter particles.

2.3 (HF) Secondary vertex reconstruction

Secondary vertices (SV) coming from decays of heavy flavour (HF) hadrons are reconstructed later, on the analysis level, which is based on the already reconstructed objects: events and particles (as described in Sec. 2.2).

Multiple SV candidates are usually considered for a predefined list of tracks, *e.g.* a set of tracks that are constituents of a single jet. In this study, SV candidate is reconstructed for each possible three-track combination by finding the minimum-distance point among a triplet of tracks approximated as straight lines (with errors as weights). Then the candidates are filtered based on the calculated parameters, and either one or multiple of them is selected for further analysis.

2.4 Jet reconstruction and performance

ALICE can measure two classes of jets: those reconstructed solely from tracks of charged particles, called "charged-particle jets" or shortly: "charged jets", and those which make use of calorimeters and therefore accounting also for a neutral fraction of the jet energy, which are called "full jets". In this thesis, only charged-particle jets are used. Therefore further description will be limited to them.

In most of the analyses in ALICE, jets are reconstructed using anti-k_{T} algorithm [17]. Resolution parameter R is usually chosen to be between 0.2 and 0.7, with the most frequent value of 0.4.

Charged-particle jets are reconstructed out of tracks with $p_{\mathrm{T}} > 0.15\,\mathrm{GeV}/c$ and $|\eta| < 0.9$. A condition that the whole jet should fit in this acceptance puts the constraint on the jet axis pseudorapidity $|\eta_{jet}| < 0.9 - R$. It means that ALICE acceptance for jets with $R = 0.7$ is 3.5 times smaller than for jets with $R = 0.2$

Despite the typical usage of jets as the proxies to the initiating partons, their measurements are rarely corrected up to the parton level. Usually, the corrections only account for the underlying event (UE) and detector effects *i.e.* correct up to the level of measurable particles (particle level). The impact of these two factors on the measured jet properties are normally corrected for in the unfolding procedure (see Sec. 3.4), where response matrices corresponding to both effects can be factorized (treated as independent) or not. In pp collisions,

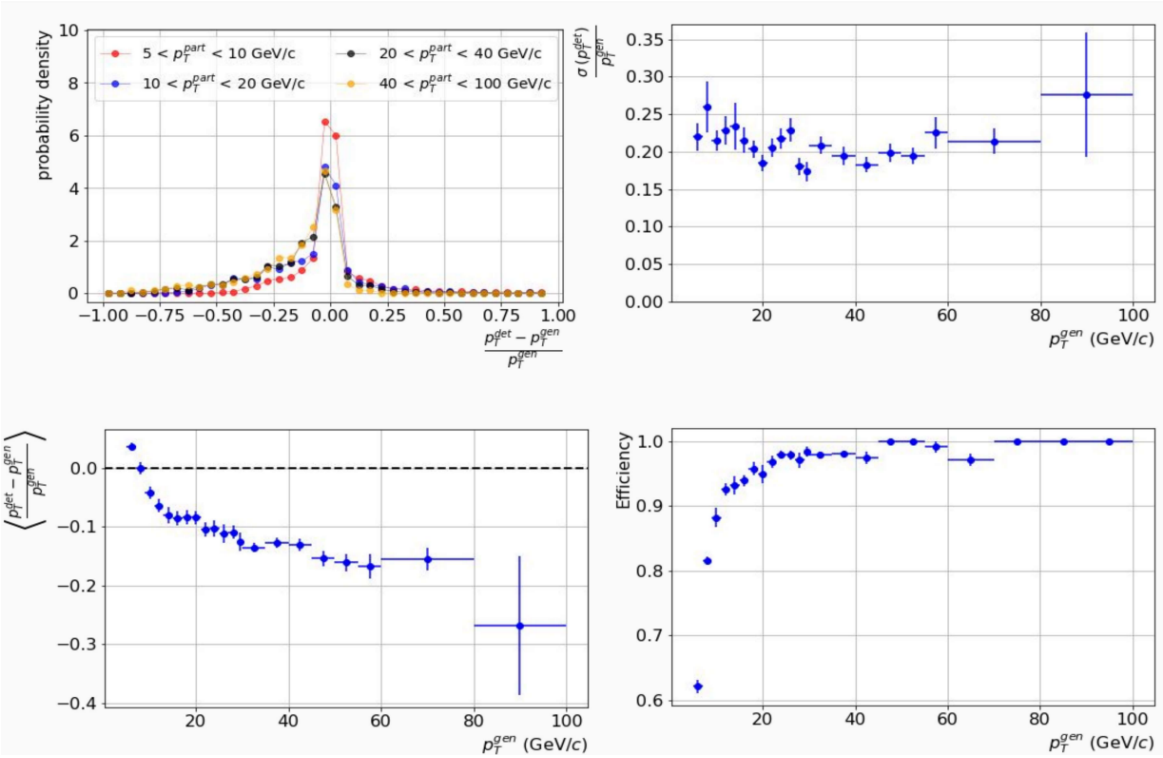

Figure 2.11: Performance of jet reconstruction.

the average transverse momentum density related to the UE activity ρ_{UE} is at the level of $1\,\mathrm{GeV}/c$ [88] and is much smaller than the contribution due to detector effects. As the jet is a composition of tracks, the detector performance in the measurement of jets is a function of single track performance, namely tracking efficiency and p_T resolution. Additional effects could be attributed to the increased density of tracks inside the jet, causing tracks to overlap. Track density inside jets is, however, limited. As it has been shown in [89] even for the most collimated jets (i.e. small $R = 0.2$ and high $p_\mathrm{T} = 80$–$100\,\mathrm{GeV}/c$) the average number of tracks in jet $\langle N_{ch} \rangle = 8$ which corresponds to the track density equal $\mathrm{d}^2N/\mathrm{d}\eta\,\mathrm{d}\varphi = 8/\pi R^2 = 64$ per unit of area in η-φ space. It is a much lower value than the tracking capabilities of ALICE, which reach the environment of central (0-5%) Pb–Pb collision, where $\langle \mathrm{d}N/\mathrm{d}\eta \rangle = 1943$ and $\langle \mathrm{d}^2N/\mathrm{d}\eta\,\mathrm{d}\varphi \rangle = 1943/2\pi = 310$ [90].

Using a detailed simulation of the detector with GEANT software [91] one can study the response of the detector for a given probe. Jet simulated with some event generator like PYTHIA is propagated through detector material. At both levels: generated (*i.e.* with perfectly reconstructed particles) and detector (taking into account finite efficiency and resolution), jets are reconstructed with the same selection criteria and matched (based on angular distance). Performance of the jet p_T determination is then assessed by comparison of values obtained at both levels. It is usually quoted in terms of 3 quantities (where $p_{\mathrm{T,part}}^{\mathrm{jet}}$ is the generated or particle-level or truth-level jet p_T and $p_{\mathrm{T,det}}^{\mathrm{jet}}$ is the reconstructed or detector-level jet p_T):

- jet energy scale (JES) – $\langle \frac{p_{\mathrm{T,det}}^{\mathrm{jet}} - p_{\mathrm{T,part}}^{\mathrm{jet}}}{p_{\mathrm{T,part}}^{\mathrm{jet}}} \rangle$, *i.e.* relative mean shift of the reconstructed jet p_T w.r.t its true value
- jet energy resolution (JER) – $\frac{\sigma(p_{\mathrm{T,det}}^{\mathrm{jet}})}{p_{\mathrm{T,part}}^{\mathrm{jet}}}$, *i.e.* relative spread of the reconstructed jet p_T for jets with given true p_T

- reconstruction efficiency – probability that given jet will be reconstructed, valid mostly jets close to the selected cut-off, *e.g.* at low p_{T}

Fig. 2.11 shows the ALICE performance of the jet detection. The probability of relative p_{T} difference (top left) shows large asymmetry, which arises mostly from the tracking miseffi-ciency, whereas finite track p_{T} resolution contributes to more or less symmetric spread around zero. As a result, reconstructed jet p_{T} is, on average, below its true value by around 10-20% (bottom left). Observed large asymmetry of the detector effects, convoluted with finite detection efficiency and steeply falling jet spectrum, is a reason why turning towards unfolding, considering a full response matrix is necessary.

2.5 Hybrid tracks

One of the prerequisites for analyzing jets based on the tracks of charged particles is the uniform tracking efficiency distribution of the detector over the whole considered angular phase space. Any irregularities in it lead to different responses of the detector depending on the position of the probe. Gaps in the acceptance are especially harmful in the jet analysis as jets are extended objects, and even a small gap affects a large fraction of the jet sample. For instance, a jet with $R = 0.4$ covers roughly $\frac{\pi R^2}{2\pi \times \Delta\eta} = 8\%$ of ALICE acceptance for jets – it means that even a tiny acceptance gap will affect almost 10% of the jet sample. Such irregularities are also hard to correct.

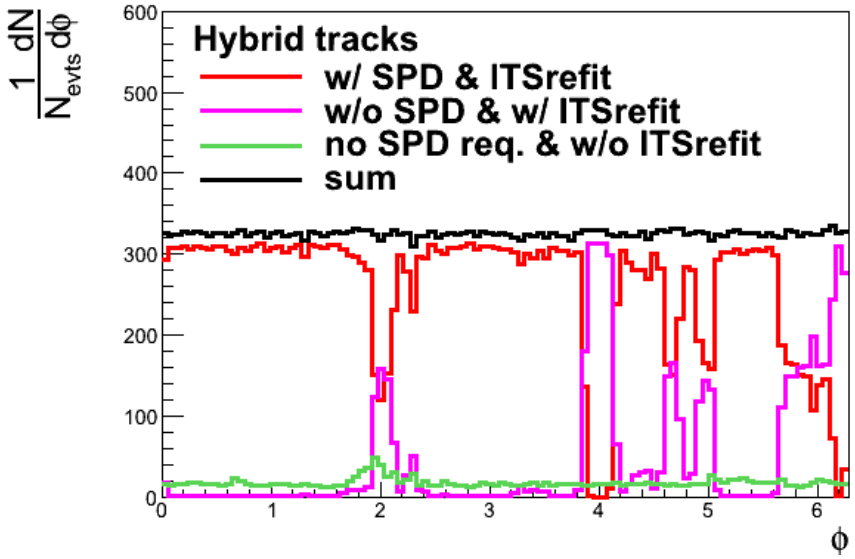

Figure 2.12: Azimuthal angle φ distributions of different track categories (private communication)

In the ALICE detector, some parts of the SPD were switched off during data taking due to a cooling system failure. This has resulted in the presence of irregularities in particle detection efficiencies (see red distribution in Fig. 2.12) As a solution to this problem, a properly selected set of detector cuts that ensure uniform distributions in (η, φ), called *hybrid tracks*, was proposed. This approach relaxes some quality cuts, sacrificing track p_{T} and DCA resolution in the affected regions of the detector.

Hybrid tracks combine two classes of tracks: *global tracks* and *complementary track* cuts. Global tracks satisfy usual quality cuts, including at least one hit in the SPD and ITS refit. The complementary tracks are the tracks lacking hit in SPD (but with ITS refit), which

are normally discarded, but in this approach, are preserved to improve the uniformity of ALICE acceptance. As shown in Fig. 2.12, the target was achieved – the sum of global and complementary tracks is uniform. The quality of the tracks, especially DCA resolution, will still vary between track classes and, therefore, will not be constant across φ.

A set of cuts used for each class of tracks, together with differences between a selection of tracks for analyses of inclusive jets and HF jets, are described in 3.1.5.

Chapter 3

Analysis of b–jets in pp collisions at $\sqrt{s} = 5.02\,\mathrm{TeV}$

3.1 Analysed data

3.1.1 Data sets

This analysis is based on the data collected by the ALICE experiment in 2017 during the LHC Run 2. It consists of events recorded during proton-proton collisions with the centre of mass energy $\sqrt{s} = 5.02\,\mathrm{TeV}$. The technical names of these data-taking periods are `LHC17p` and `LHC17q`.

Due to the relatively high maximum drift time of SDD (two middle layers of ITS), it was not able to provide information at the rate of a fast L1 trigger. To maximize the collected number of events, a large fraction of them (around 70%) were recorded without SDD information. In order to obtain homogeneous performance, the remaining 30% of events were also reconstructed without considering SDD information [1]. In total, slightly more than 1 billion events were recorded.

3.1.2 MC productions

Each data-taking run is associated with a dedicated Monte Carlo (MC) production, which mimics the experimental conditions. MC production anchored to analysed in this thesis periods is denoted as `LHC18b8`. The MC sample is simulated with PYTHIA 8.210 with the Monash 2013 tune [92] and particles are transported via detector material with GEANT 3 [93].

The physical $p_{\mathrm{T}}^{\mathrm{jet}}$ spectrum is steeply falling and spans over several orders of magnitude. In order to obtain a large enough sample of high-p_{T} jets, the PYTHIA simulations are performed in the so-called p_{T}-hard bins and then weighted according to their cross section. Twenty bins with the following edges {5, 7, 9, 12, 16, 21, 28, 36, 45, 57, 70, 85, 99, 115, 132, 150, 169, 190, 212, 235, 235+} GeV/c were used, each populated with 8 millions of events.

In the region where the expected number of counts is below one, upward fluctuation may result in a single count which is further multiplied by a large weight. The resulting jet p_{T} spectrum has, therefore, spikes in its highp_{T} tail. Jets with $p_{\mathrm{T}}^{\mathrm{jet}} > 3 \times p_{\mathrm{T,hard}}$ are rejected to mitigate this effect. This procedure is well established in ALICE and has no side-effects while recovering smooth $p_{\mathrm{T}}^{\mathrm{jet}}$ spectrum.

[1] in ALICE internal nomenclature these reconstruction types are called `FAST` and `CENT_woSDD` correspondingly

3.1.3 Event selection

Recorded events were filtered based on several criteria:

- minimum bias (MB) trigger
- pile-up rejection
- vertex reconstruction
- vertex quality
- vertex position

All events have to satisfy MB trigger requirement, namely the coincidence of signals in both sides of the V0 detector. Events with more than one primary vertex reconstructed are rejected as pile-up events. Next, the events must have a primary vertex reconstructed. Only events with high-quality vertex are accepted. The difference between the z coordinate of the vertex reconstructed from tracks and the vertex reconstructed from SPD should be below 0.5 cm. Additionally, if the vertex is reconstructed from SPD tracklets only, its resolution should be below 0.25 cm. Finally, only vertex within $|z| < 10\,\text{cm}$ from the nominal interaction point is accepted. It provides uniform acceptance and tracking efficiency of ITS and TPC at midrapidity. Fig. 3.1 shows the distribution of z coordinate of event vertex, before and after the above-mentioned selection criteria. The numbers of events that were collected and selected are shown in Table 3.1.

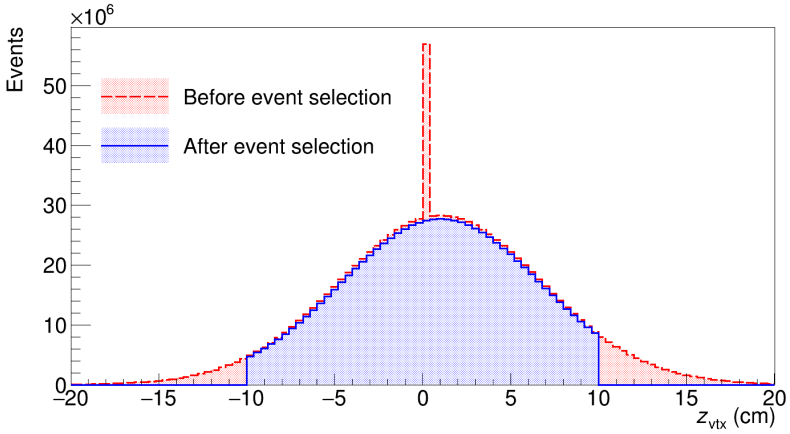

Figure 3.1: Event vertex position along z axis, before and after event selection. Excess of entries at 0 corresponds to events in which the vertex was not reconstructed.

Table 3.1: Number of processed events passing consecutive cuts.

No cuts	Pile-up	Vertex reconstruction and quality	Vertex position
1054.9×10^6	1054.1×10^6	1001.0×10^6	910.8×10^6

3.1.4 Underlying event subtraction

Jets reconstructed in the events are corrected for the average contribution of the underlying event (UE) background, using formula: $p_{\mathrm{T,reco}}^{\mathrm{jet}} = p_{\mathrm{T,raw}}^{\mathrm{jet}} - \rho \times A_{\mathrm{j}}$, where A_{j} is an "active" jet area [94] and ρ is the average UE activity. ρ is computed using estimator introduced by CMS [95]:

$$\rho = \underset{j \in \text{jets}}{\text{median}} \left\{ \frac{p_{\mathrm{T},j}}{A_j} \right\} \cdot C_{\mathrm{occ}} \ ,$$

where C_{occ} is event occupancy correction and sum runs over jets found by the k_{T} algorithm in the event filled with "ghost" particles, excluding two leading jets. This way ρ represents the average p_{T} per area unit added to jet p_{T} by UE. The real contribution of the background is still subject to local fluctuations, which are corrected for in the unfolding procedure described in Sec. 3.4

3.1.5 Track selection

Tracks of charged particles used in the analysis are selected based on a range of kinematic and quality cuts, summarized in Table 3.2. In general, these are TPC tracks prolonged to ITS with successful refit inward step and rejected kinks (see Sec. 2.2). Most of the cuts are rather standard for ALICE, with the exception of DCA cuts which are looser. Curious readers may refer to [96] for the precise definitions of all terms. Only tracks with $|\eta| < 0.9$, *i.e.* having chance to cross all TPC rows and with p_{T} above $0.15\,\mathrm{GeV}/c$ are selected.

Details of hybrid tracking Due to the malfunction of some SPD segments, in jet analyses an approach called *hybrid tracking* is utilized in ALICE, as described in 2.5. Filtering of the tracks is performed centrally and a set of pre-defined track classes are provided for analysers. Each class has assigned one filtering bit, which identifies it.

A typical set of tracks used for jet analyses consists of classes "8" and "9" (see Table 3.2). Class "8" defines good quality tracks and class "9" so-called *complementary* tracks whose main purpose is to fill the holes in SPD acceptance. The only difference between them is that class "9" does not require the presence of at least one SPD hit (but it does require ITS refit). Tracks belonging to class "9" must not belong to class "8" in order to avoid double-counting.

One of the cuts utilized in class "8" selects only tracks whose final path is in fair agreement with TPC-only track constrained to the event vertex ($\chi^2 < 36$). It is the so-called "golden χ^2 cut". It is used to eliminate secondary tracks [2], enhanced by the relaxed cut on distance of closest approach (DCA). A side effect of this cut is that it reduces also efficiency for decays of heavy flavour (HF) particles. Therefore, for analyses involving HF jets, class "8" is replaced with class "4", which does not include this cut.

As a result, tracks which do not have a point in SPD and do not pass the "golden χ^2 cut" are not accepted (they are complementary to class "4" but class "9" is defined as complementary to class "8"). Resulting distribution of track φ is slightly less uniform, but the effect is marginal.

3.1.6 Jet selection

Jets are reconstructed from tracks selected according to the previous section. The anti-k_{T} algorithm with jet radius $R = 0.4$ and four-momentum recombination scheme (E-scheme) is used. The pion mass is assumed for all jet constituents. Jets' axes must be reconstructed within $|\eta_{jet}| < 0.9 - R = 0.5$ so that, the jets do not exceed $|\eta| < 0.9$. Jets are also required

[2] those originating from weak decays of long-lived (strange) hadrons or from interactions in the detector material

Table 3.2: Selection criteria for tracks. Only classes "4" and "9" are used in the analysis. Additionally tracks from class "9" must not belong to class "8".

kinematic selection			
track p_{T}			$> 0.15\,\text{GeV}/c$
track $\lvert\eta\rvert$			< 0.9
quality selection			
$N^{\text{TPC}}_{\text{crossed rows}}$			> 70
$N^{\text{TPC}}_{\text{crossed rows}}/N^{\text{TPC}}_{\text{findable clusters}}$			> 0.8
$\chi^2/N^{\text{TPC}}_{\text{clusters}}$			< 4
$\chi^2/N^{\text{ITS}}_{\text{clusters}}$			< 36
$\sqrt{(\text{DCA}_{xy}/2.4\,\text{cm})^2 + (\text{DCA}_z/3.2\,\text{cm})^2}$			< 1
DCA_{xy}			$< 2.4\,\text{cm}$
DCA_z			$< 3.2\,\text{cm}$
kink daughters			rejected
TPC refit			required
ITS refit			required
track class-specific			
	"4"	"8"	"9"
"golden χ^2 cut"	✗	✓	✓
$f^{\text{TPC}}_{\text{shared clusters}} < 0.4$	✗	✓	✓
$N^{\text{SPD}}_{\text{hits}} > 0$	✓	✓	✗

to have an (active) area below $0.6 \cdot \pi R^2$, which is important in Pb–Pb collisions to remove combinatorial jets, but in pp has only a tiny effect at very low $p^{\text{jet}}_{\text{T}}$. Finally, only jets with reconstructed $p^{\text{jet}}_{\text{T}} > 5\,\text{GeV}/c$ (after UE subtraction) are considered.

3.2 *b*–jet tagging

Tagging of the *b*-jets is performed with the machine learning (ML) model trained on data from the PYTHIA simulations. It is based on the properties related to long lifetime of the beauty hadrons. The next sections describe input data, choice of parameters of the model and achieved performance.

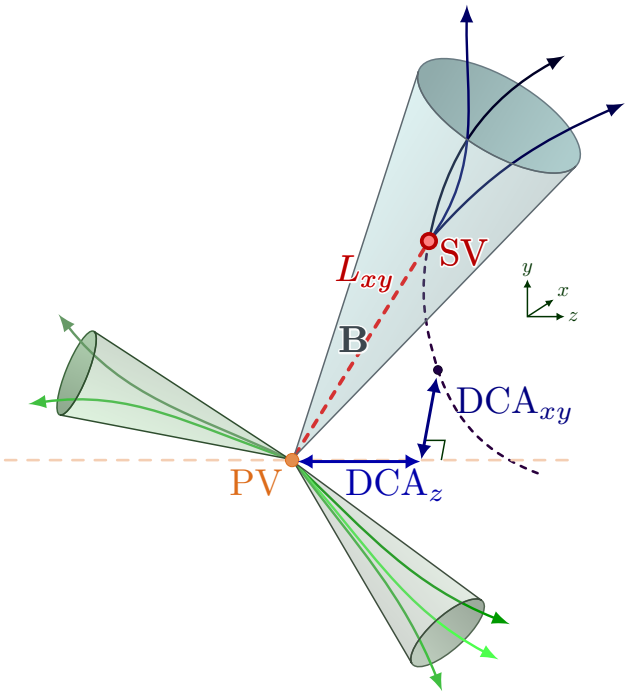

Figure 3.2: Illustration of features used for *b*-jet tagging.

3.2.1 *b*-jet definition

b-jet definition is based on the hadronic tag from MC information. A jet is tagged as a *b*-jet, if there was a beauty hadron within the jet radius in the Monte Carlo history. If not, and a charm hadron was there, it is tagged as a *c*-jet. All other jets are tagged as *udsg*-jet.

3.2.2 Choice of ML algorithm

ML model consists of several Boosted decision trees (BDT) models, trained and applied in bins of $p_{\mathrm{T}}^{\mathrm{jet}}$. Implementation from `xgboost` package is used [97]. Our preliminary studies have shown that for the same input data, fully-connected or convolutional neural networks do not improve the model performance. Moreover, they are more sensitive to the choice of training parameters or exact architecture. It is understandable as the features used in the training are rather high-level and are provided in the tabular form. Tree-based models are known for their excellent performance in such scenarios [98].

While numerous new architectures were proposed in recent years for the jet tagging, (Energy Flow Networks [99], ParticleNet [100] or Particle Transformer [101] to mention a few), they usually focus on quark-gluon discrimination and boosted W/Z boson or top tagging. An approach based on deep sets [102] seems promising in the context of *b*-tagging. It was applied by ATLAS, on lower-level track features [103]. It is however beyond the scope of this thesis.

3.2.3 Training features

The ML model is trained on features related to the long lifetime of the beauty hadrons, see Fig. 3.2. Fragmentation of beauty jets is not well constrained in the models therefore features closely related to jet substructure like jet angularity were not used in the training. Studies of the b-jet fragmentation are also one of the interesting areas where the model could be utilized in the future, so any possible bias should be avoided.

Features used in the training can be divided into three categories: those related to the whole jet, features of jet constituents (tracks) and features of secondary vertices (SV), all listed below. As described in Sec. 2.3, all three-track combinations of jet constituents are considered as SV. Only vertices with dispersion $\sigma_{\text{SV}} < 0.05\,\text{cm}$ are used.

BDT requires a tabular format of the data. For each jet, the listed below features were extracted for 10 tracks and 3 SV, the rest was dropped. Tracks were ordered by $|S_{\text{DCA}_{xy}}|$ and SV by $S_{L_{xy}}$. If the jet does not have the required number of objects, the related features are treated as "missing values". There is no need to treat them in a special way as they are handled naturally by xgboost.

- features at jet-level:
  - $p_{\text{T}}^{\text{jet}}$
  - N_{tracks} – jet multiplicity, *i.e.* number of tracks in the jet
  - N_{SV} – number of SV reconstructed from jet constituents
- features of tracks:
  - $p_{\text{T}}^{\text{track}}$
  - $\sigma_{\text{DCA}_{xy}}$ and σ_{DCA_z} – uncertainty of DCA in the beam direction of z and perpendicular plane xy
  - $S_{\text{DCA}_{xy}} = \text{DCA}_{xy}/\sigma_{\text{DCA}_{xy}}$ and $S_{\text{DCA}_z} = \text{DCA}_z/\sigma_{\text{DCA}_z}$ – significances of DCA
  - $|S_{\text{DCA}_{xy}}|$ and $|S_{\text{DCA}_z}|$ – their absolute values
- features of SV:
  - L_{xy} – decay length
  - $\sigma_{L_{xy}}$ – uncertainty of the decay length
  - $S_{L_{xy}} = L_{xy}/\sigma_{L_{xy}}$ – significance of the decay length
  - χ^2_{SV} of the vertex fit
  - $\sigma_{\text{SV}} = \sqrt{d_1^2 + d_2^2 + d_3^2}$, where d_i is DCA between the i-th contributing track and the secondary vertex – vertex dispersion

Most of the features are related to the long lifetime of the beauty hadrons. χ^2_{SV} and σ_{SV} help to remove SV candidates built from tracks which do not originate from the same SV. p_{T} of the tracks is important because the other track properties like DCA resolution depend critically on it. We note that it can introduce some fragmentation bias. To minimize its effects it was not combined with any information on the angular distribution of tracks inside the jet, not scaled by the $p_{\text{T}}^{\text{jet}}$ and not used to sort the tracks. Skipping the information on track p_{T} also does not guarantee a lack of bias, as it can be potentially introduced by other, correlated features.

There are also some derived features like $|S_{\text{DCA}_{xy}}|$ or $S_{L_{xy}}$, which do not carry any new information, but are still useful if one takes into account the specificity of the BDT. First of

all, they make it easier for BDT to make a cut on both tails of the distribution. The trees are grown using a greedy algorithm. An optimal pair of cuts will not be used if none of the cuts alone provides a good separation between the classes. Secondly, it allows to reduce the depth of the tree (so the model complexity). Such derived quantities provide model with some human guidance, about what features should be combined together. It was proved empirically that adding these features improves the model performance.

Most of the original features (from which the derived ones are computed) are still stored, as they bring some additional information. However, the raw DCA values were removed as they were found to be worse reproduced in MC. As the ML model is inherently multidimensional, it was not done based on the comparison of 1D distributions between data and MC. Instead, a new BDT model was trained. Its objective was to differentiate data from MC. Then the most important features [3], which enable this differentiation, were recursively removed.

3.2.4 Parameters

The BDT were trained with the following parameters:

- `max_depth` = 5
- `n_estimators` = 500
- `learning_rate` = 0.2
- `subsample` = 0.5
- `colsample_bynode` = 0.5
- `colsample_bytree` = 0.5

We refer the reader to the package documentation for the exact meaning of each parameter. We note that (for this dataset) BDT are not very sensitive to the exact values of the parameters and they achieve similar performance for the wide range of "reasonable" parameter values.

The ML model was trained on the sample consisting of approximately 1.2M *b*-jets and 1.2M of background jets. It was half of the total available MC statistics for *b*-jets. The jets used in the training are not used on any other step of the analysis. Ratio of *c* to *udsg*-jets was one of the parameters that were tuned in the analysis.

Training background composition A natural choice for training background composition would be the same as the composition of the background in the real data, *i.e.* approximately 10% of *c*-jets [43, 106]. *b*-jets are however much easier to differentiate from the *udsg*-jets than from *c*-jets as charm hadrons also have a substantial lifetime. As a result in the region of interest (*b*-jet tagging purities $> 50\%$) the *c*-jets dominate the sample of background jets which were incorrectly tagged as *b*-jets as shown in Fig. 3.3 (left).

[3] judged by the tree-based feature importances from xgboost (Eq. 44 and 45 in [104]) and permutation importance [105]

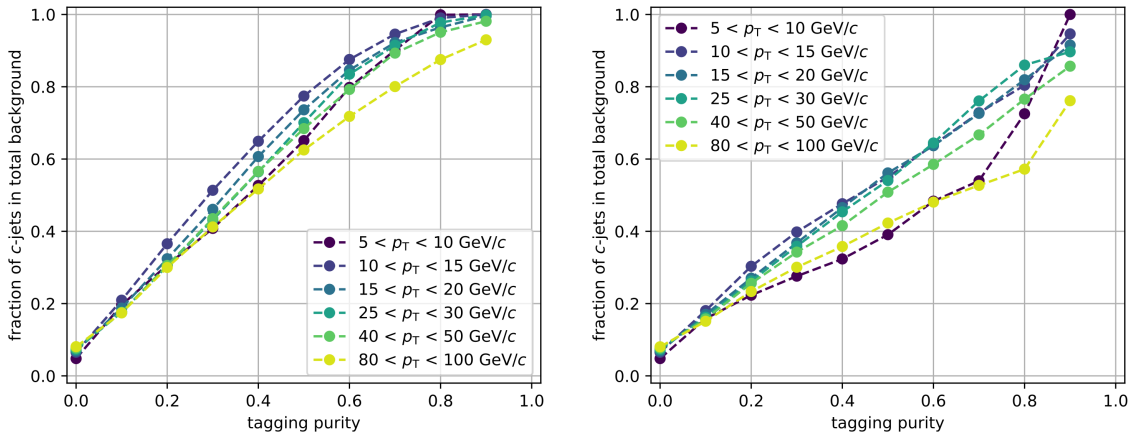

Figure 3.3: Fraction of c-jets in the total mistagged background as a function of b-jet tagging purity for various p_{T} ranges. A model was trained on a background composed of 10% of c-jets and 90% of $udsg$-jets (left) and 100% of c-jets (right).

It is undesirable because b-jet purities are then used to determine the model working points. If the mistagged background sample consists of only c-jets, then purities become more sensitive to the modelling of c-jet abundancy.

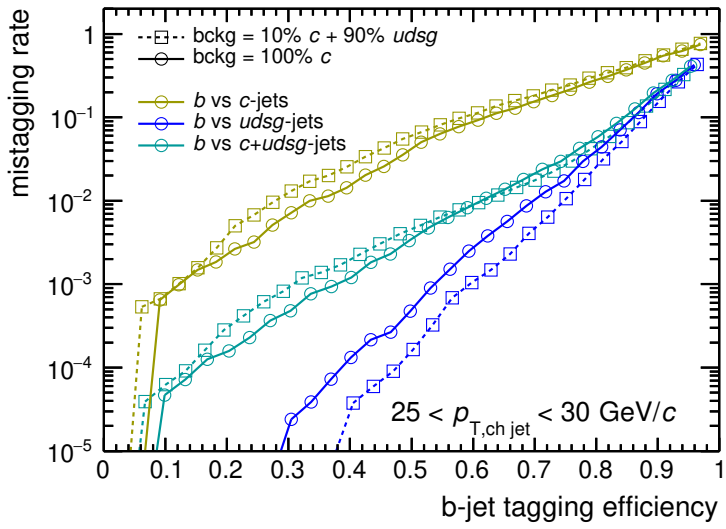

Figure 3.4: Background mistagging rate of c-, $udsg$- and combined c +$udsg$-jets as a function of b-jet tagging efficiency for two models: trained on natural abundances (10% of c-jets and 90% of $udsg$-jets) and on pure c-jet backgrounds.

With the increase of the c-jet contribution in the training background, the model focuses more on separating b and c-jets. It appears that the model trained on pure c-jet background [4] is still capable of differentiating b from light flavour jets as shown in Fig. 3.4. Such a model has lower (better) mistagging rate for c-jets and higher (worse) for $udsg$-jets, which result in an overall slight improvement of tagging performance, especially in the high-purity (low-efficiency) region. Another advantage of using pure c-jet background is the reduction in the c-jet contribution in the mistagged background shown in Fig. 3.3 (right).

[4] any modification of the background composition is applied only for the training, the validation which results are shown on the plots is performed on the unchanged background

Weights of training samples All the steps in this analysis have to take into account that the PYTHIA simulation was performed in the hard p_{T} bins and all the samples or distributions need to be weighted using proper weights. This would be a default scenario also for training of the ML model. This was however not done. I n order to obtain the model with more uniform performance across the p_{T}, all the jets during training had weights equal to one. Otherwise, too much weight is assigned to the low-p_{T} part of the sample.

Training in p_{T} bins The model was trained in the bins of $p_{\mathrm{T}}^{\mathrm{jet}}$, with the following boundary values: $\{5, 10, 15, 25, 50, 100, 200\}$ GeV/c.

In principle, this should enable the model to learn from the features' values characteristic for given p_{T}. For instance, the decay length L_{xy} is proportional to the lifetime of beauty hadron, which is proportional to its Lorentz gamma factor.

Empirically, it is not observed and the performance of the model trained in bins and of a single BDT are the same. It can be explained by the larger dataset used in the single BDT scenario.

Training in bins is then applied for practical reasons: it allows for easy extension or reduction of the measured $p_{\mathrm{T}}^{\mathrm{jet}}$ range without impacting the jets in the preserved range. It also reduces the memory footprint and allows for easier distribution of computation.

Application of the model Another "parameter" of the model is the way in which it is applied. To use the model as a tagger, one needs to define the so-called working point, *i.e.* the threshold on the BDT score above which the jets will be tagged as b-jets. Several approaches exist.

Cut defined as a constant value of the BDT score was excluded as the scores have no physical interpretation. It is easy to obtain the model that will have the BDT score distribution shifted to the left or right by weighting by a single number all the examples from one class.

In this analysis, the working point is defined separately for each bin of the measured jet p_{T}. It is a threshold for which a given value of b-jet purity is reached. The default value is $P_{\mathrm{tag}}^{\mathrm{MC}} = 70\%$ but the method aims at stability over some range of the purities. The working points are always defined with MC-derived purities even when the values of the purities that are used to correct the obtained p_{T} spectrum come from the data-driven method. The performance of the model generally improves with jet p_{T} so the corresponding tagging efficiencies will be increasing.

As a systematic variation the working point with a constant efficiency instead of constant purity is used, see Sec. 3.6.3.

3.2.5 Model performance

The metrics used to quantify model performance are:

- tagging efficiency ϵ_{tag} – probability that a true b-jet is (correctly) tagged as a b-jet,
- mistagging rate – probability that a *udsg*- or c-jet is (incorrectly) tagged as b-jet,
- tagging purity P_{tag} – probability that a jet tagged as b-jet is truly a b-jet.

The performance of the model in simulated data is shown in Fig. 3.5. It is compared to the other analysis of b-jets performed in ALICE, which used rectangular cuts on L_{xy} and σ_{SV} [107].

ML model achieves much better performance: the tagging efficiency is two times higher or alternatively, the suppression of the background is increased by more than an order of

magnitude. For the same tagging efficiency it corresponds to an increase of b-jet purity from 45% to 85%.

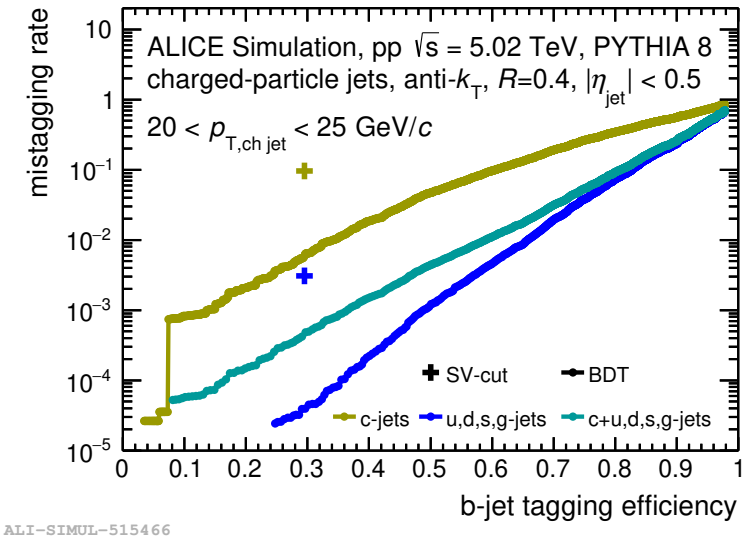

Figure 3.5: Background mistagging rate of c-, $udsg$- and combined $c+udsg$-jets as a function of b-jet tagging efficiency. Performance of the ML model from this thesis ("BDT") is compared to cut-based method using SV from [107].

Fig. 3.6 shows the tagging purity and efficiency for various jet p_{T}. It is based solely on MC and assumes the flavour abundances from PYTHIA are accurate. In the next step the provided values will be validated in a data-driven way, but still, the purities derived from MC are used to determine the threshold values for the working points. The performance of the model improves with the rising jet p_{T} and then saturates around $p_{\mathrm{T}}^{\mathrm{jet}} = 30\,\mathrm{GeV}/c$. For the default tagging purity of 70% the efficiencies grow from 20% to 65%.

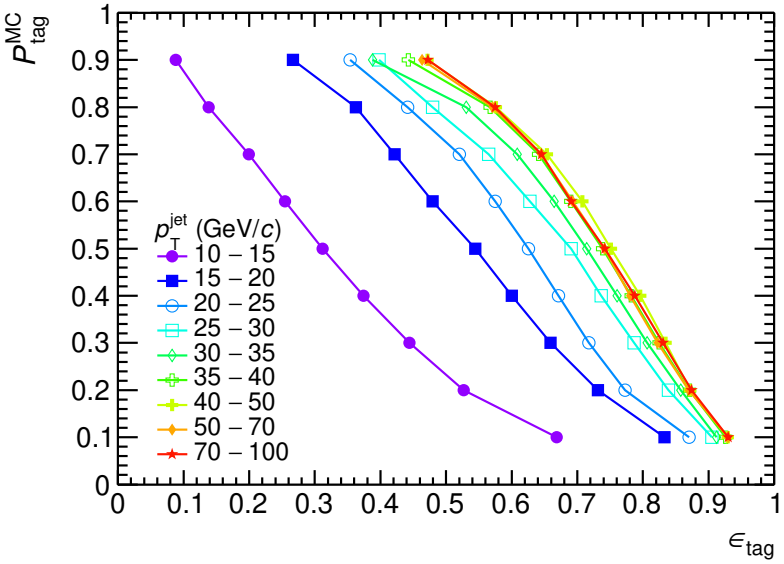

Figure 3.6: Tagging purity as a function of tagging efficiency for various jet p_{T}.

3.3 Tagging performance corrections

The sample of jets tagged as b-jets by the ML model has to be corrected for tagging performance (efficiency and purity) and then for jet p_{T} smearing (due to detector effects and underlying event fluctuations). The latter is done in the unfolding procedure described in Sec. 3.4.

The b-jet spectrum corrected for tagging performance — called "measured spectrum" — is obtained from the raw number of tagged jets using the following formula:

$$\frac{\mathrm{d}N_{\mathrm{measured}}}{\mathrm{d}p_{\mathrm{T}}^{\mathrm{jet}}} = \frac{\mathrm{d}N_{\mathrm{tagged}}}{\mathrm{d}p_{\mathrm{T}}^{\mathrm{jet}}} \cdot \frac{P_{\mathrm{tag}}}{\epsilon_{\mathrm{tag}}} \ ,$$

where ϵ_{tag} is tagging efficiency and P_{tag} is tagging purity.

Tagging efficiencies are derived directly from MC simulations. Doing the same with the purities results in the N_{measured} being strongly dependent on the working point selection. The most probable reason for that is the mismodelling of the HF jet production in PYTHIA. To minimise the reliance on MC, the purities are determined based on a data-driven method of template fitting.

Templates for three classes of jets: b-jets, c-jets and $udsg$-jets are derived from the sample of MC jets, which belong to a given class and were tagged as b-jets by the ML model.

The minimized loss function was the modified χ^2 function. Except for the statistical uncertainties in the data, it includes the statistical uncertainties on the MC templates:

$$\chi^2_m = \sum_{i=1}^{\mathrm{nbins}} \frac{N_i - (f_b \cdot T_{b,i} + f_c \cdot T_{c,i} + (1 - f_b - f_c) \cdot T_{udsg,i})}{\sigma^2_{N_i} + (f_b \cdot \sigma_{T_{b,i}})^2 + (f_c \cdot \sigma_{T_{c,i}})^2 + ((1 - f_b - f_c) \cdot \sigma_{T_{udsg,i}})^2} \ ,$$

where N_i is the content of i-th bin in the normalized data distribution, f_b, f_c are the fitted fractions of b and c-jets, T_x are the corresponding MC templates and σ denotes statistical uncertainties of quantity in the subscript. The fractions of b-, c- and $udsg$-jets are constrained to be positive and to sum to one. The fits were performed with `zfit` package [108]. The implemented modification is important in case of the highest $P_{\mathrm{tag}}^{\mathrm{MC}}$ where the mistagging rate for the $udsg$-jets is of the order of 10^{-5}. It also allows us to properly include the statistical uncertainties of the templates, which are not Poissonian as they originate from the MC simulation performed in the PYTHIA p_{T}-hard bins. Tagging purity P_{tag} used in the tagging correction is equal to f_b.

Distributions of three different observables are used in the fitting:

- BDT score – pseudo probability returned by the ML model
- $\mathrm{M_{jet}}$ – jet invariant mass
- $\mathrm{M_{SV}}$ – invariant mass of the secondary vertex with the highest $S_{L_{xy}}$

The three observables are not correlated and have different properties. $\mathrm{M_{jet}}$ and $\mathrm{M_{SV}}$ represent physical quantities while BDT score is number returned by ML model without straightforward interpretation. Correlation between b and c fractions are: negative for BDT score and $\mathrm{M_{SV}}$ and close to zero for $\mathrm{M_{jet}}$.

Fig. 3.7 shows the exemplary fits to the three observables for $20 < p_{\mathrm{T}}^{\mathrm{jet}} < 25\,\mathrm{GeV}/c$ and the default working point: $P_{\mathrm{tag}}^{\mathrm{MC}} = 70\%$. The uncertainties on the templates are not visualized but are included in the fit. The uncertainty on the total fit is the standard deviation of the ensemble of sums of the templates. The templates were weighted by the fractions which were generated from the two-dimensional Gaussian distribution with the mean and covariance matrix obtained from the fit.

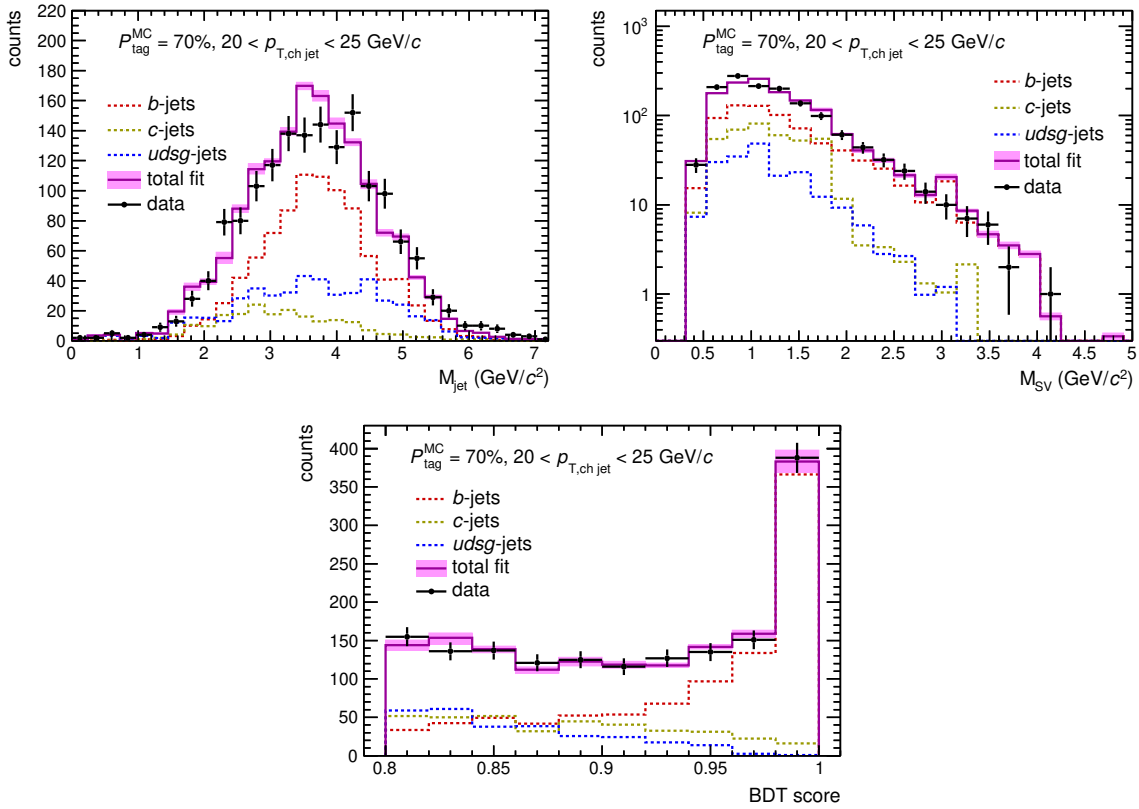

Figure 3.7: Exemplary fits to the three observables: M_{jet} (top left), M_{SV} (top right) and BDT score (bottom).

Out of the three observables, BDT score provides the best separation between b-jets and background jets. It is close to optimal thanks to an optimization performed by the ML algorithm. Due to worse separation power, M_{jet} and M_{SV} provide worse precision and require higher statistics. They do not yield meaningful results for the $p_{\text{T}}^{\text{jet}} > 30$–$50\,\text{GeV}/c$.

Fig. 3.8 shows the number of b-jets tagged in data and corrected for tagging efficiency and purity (N_{measured}) obtained with different methods. They are shown as a function of $P_{\text{tag}}^{\text{MC}}$ in the form of a ratio to the default result. The compared methods are fits to the three observables and the purity obtained directly from MC ($P_{\text{tag}}^{\text{MC}}$). One can see that the MC-based corrections give the N_{measured} value strongly dependent on the working point selection, with differences reaching 50%. The results using fit to BDT score are consistent across a very wide range of purities and the differences rarely exceed 10%. The other fitted observables, M_{jet} and M_{SV}, provide only very weak constraints on N_{measured} – they are not so consistent across working points and often pull in the opposite directions. However, on average they are consistent with the results from fits to BDT score in majority of p_{T} bins, especially at higher purities. Their values are not used in the analysis and serve only as a cross-check.

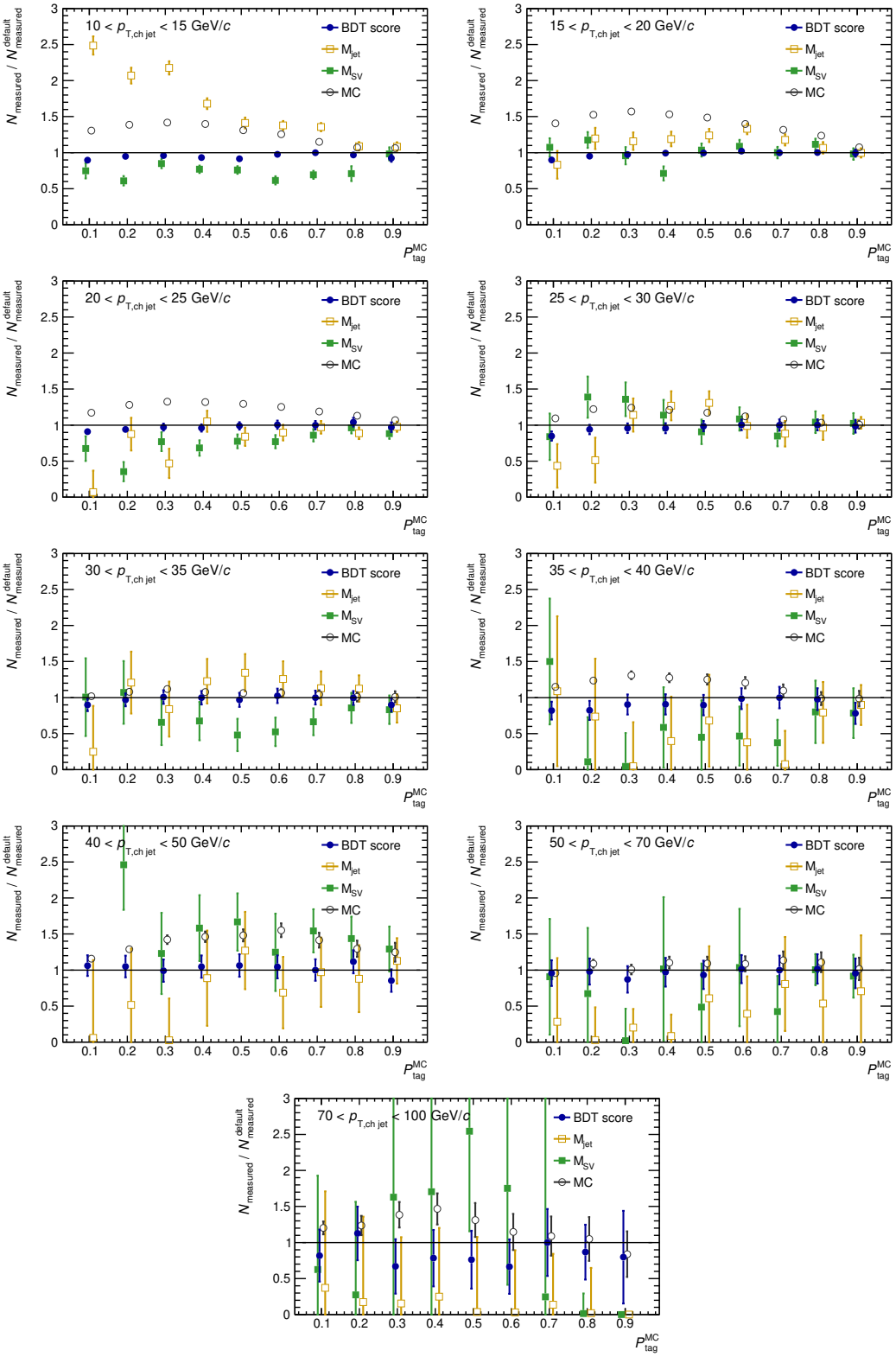

Figure 3.8: Comparison of N_{measured} as a function of $P_{\text{tag}}^{\text{MC}}$ obtained with various methods divided by the default value (fit to BDT score at $P_{\text{tag}}^{\text{MC}} = 70\%$). See text for details.

3.4 Unfolding

Traces left by particles in imperfect detectors does not allow for direct comparison to theoretical predictions. The common level on which the two perspectives often meet is the so-called "particle level". Theoretical description of the partonic interaction happening at colliders must be extended by simulation of further system evolution, including the hadronization process to provide prediction in terms of colorless (and measurable) particles, not partons.

On the other side, experimentally collected traces left by particles in the detectors need to be translated into the numbers expected from the perfect detector (capable to record particles with full efficiency and infinite resolution). The procedure aiming at the removal of all detector effects is called unfolding. It is an example of a so-called inverse problem: one wants to determine the true properties of particles from the measured properties and the knowledge of how particle with given properties interacts with the detector. Other effects which one may want to remove to enable easier comparison with theory or between experiments are related to the presence of the underlying event (UE) and its local fluctuations – a crucial issue in heavy-ion collisions (and topic of Chapter 4).

3.4.1 Unfolding methods

Mathematically, the smearing of the true continuous spectrum $t(x)$ by the function representing detector and background effect $A(x, y)$ which results in the measured spectrum $m(y)$ can be expressed with the following formula:

$$m(y) = \int A(x, y)t(x)dx \ .$$

Similarly, for the measurement performed in discrete bins:

$$m_j = \sum_i A_{ji}\, t_i \ ,$$

where m_j and t_i are contents of j-th/i-th bins in the measured and true histograms respectively. A_{ji} is then an element of the so-called response matrix, equal to the probability of the transition from bin i in the true histogram to bin j in the measured histogram.

As the aim of this procedure is to deconvolute the measured spectrum, the desired mathematical operation is simply the inversion of the matrix. In practice, this solution, while providing an unbiased estimate of the true distribution, suffers from intractable variance, see Fig. 3.9. Therefore various dedicated unfolding algorithms have been developed. Their working principle is the reduction of variance by the addition of small bias, via some kind of regularization. In other words, distribution resulting from response matrix inversion has huge uncertainties and suffers from high-frequency oscillations, while the regularization methods enforce a certain level of smoothness, expected from the physical processes. Two examples of unfolding methods used in this analysis are the so-called " SVD unfolding" and the "iterative Bayes" method, both implemented in `RooUnfold` package [109] and described below.

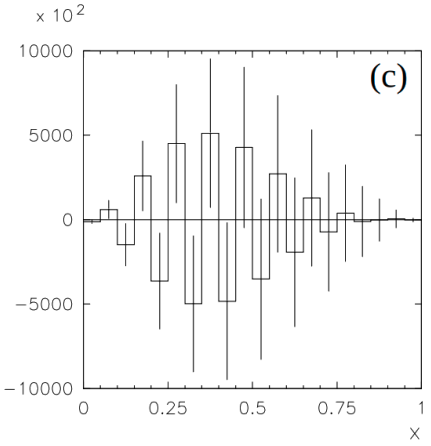

Figure 3.9: Typical true distribution obtained via direct matrix inversion – with clearly intractable fluctuations and large negative correlations between neighbouring bins resulting in unphysical, high-frequency oscillations, taken from [110].

SVD unfolding is an method introduced in [111]. In this approach regularization is realized by the addition of explicit penalty term, making it a variant of Tikhonov regularization [112] [5]. The response matrix is inverted with the Singular Value Decomposition (SVD) technique, thus the name of the method.

Starting from the unregularized matrix equation

$$m = A\,t \ , \tag{3.1}$$

the SVD factorizes matrix A of size $m \times n$ into product of three matrices: USV^T. U and V are $m \times m$ and $n \times n$ orthogonal matrices ($UU^T = I$), while S is $m \times n$ diagonal matrix, with non-negative diagonal terms s_i, called singular values of matrix A. This factorization represents the conversion from a single linear transformation A to the composition of rotation (by V^T), independent scaling of each component (by S) and another rotation (by U). The solution of the initial equation is given by

$$U^T m = SV^T t \ , \tag{3.2}$$

which can be expressed as

$$z_i = \frac{d_i}{s_i}, \ \text{ where } \ z \equiv V^T\, t \text{ and } d \equiv U^T m \ . \tag{3.3}$$

The problem with this solution arises, when d_i is insignificant and corresponding s_i is small, then z_i will be huge but still insignificant. It results in the already mentioned high-frequency oscillations with large uncertainties.

In the SVD unfolding variant as described in [111] and implemented in RooUnfold package, some major improvements are then introduced. Firstly, a preference is set towards smooth solutions. It is realised with the penalty term $\tau \cdot P(t)$ proportional to "curvature" of the discrete distribution, defined as the sum of squares of discretized second derivatives, $P(t) = \sum_i \left[(t_{i+1} - t_i) - (t_i - t_{i-1})\right]^2$. Secondly, the system of equations (3.1) is scaled by the number of generated MC entries in each bin of the true distribution. On one hand, it transforms the probability matrix into number-of-events matrix, assigning higher significance to bins with

[5] in statistics it is often called ridge regression, although sometimes this term is used in a narrower sense – for a particular choice of regularization term being L_2 penalty

a higher number of counts. Another effect is that instead of solving for true distribution, the new system of equations searches for *deviations* from the prior true distribution given, *e.g.* by the MC distribution. Searching for the distribution relative to some reasonable prior significantly simplifies the problem, especially when the distribution spans several orders of magnitude.

The modified system of equations can be solved again using SVD, giving:

$$z_i(\tau) = \frac{d_i}{s_i} \cdot \frac{s_i^2}{s_i^2 + \tau} \ ,$$

where τ is the regularization strength factor. It determines the smooth cut-off value, suppressing the terms with small singular values $s_i^2 \lesssim \tau$. τ should be chosen to be close to the s_k^2 where k is the index of the last significant d. This way, new regularization parameter $k_{\text{reg}} = 0, 1 \ldots n$ can be introduced, linked with τ by: $\tau = s_{k_{\text{reg}}}^2$

"Iterative Bayes" unfolding is an method proposed in [113]. It is a variant of truncated expectation-maximization (EM) algorithm, used also in other fields such as tomography, optics or astronomy where it is referred to as Lucy-Richardson deconvolution. In high-energy physics, it is often called "Bayesian unfolding", which is a misnomer, as it is a fully frequentist approach.

The unfolded distribution is obtained by iterative application of Bayes theorem:

$$P(t_i|m_j) = \frac{A_{ji} t_i}{\sum_l A_{jl} t_l} \ , \tag{3.4}$$

where $A_{ji} = P(m_j|t_i)$ is the response matrix. Here each observation m_j, must have some true source t_i, so: $\sum_i P(t_i|m_j) = 1$ ("fakes" can be added as another bin in t). On the other hand, not every generated count t_j has to be observed: so $0 \leq \sum_j P(m_j|t_i) = \sum_j A_{ji} \leq 1$, where the sum gives the efficiency ϵ_i of detecting t_i in any measured bin.

Best estimate of t_i is given by:

$$t_i = \frac{1}{\epsilon_i} \sum_j m_j P(t_i|m_j) \ ,$$

which however contains circular dependence on t_i through (3.4). A solution is to start from some initial values of $t_j^{(0)}$ (they may come from MC or just from flat distribution) and then iteratively compute the updated values:

$$t_i^{(k+1)} = \frac{t_i^{(k)}}{\sum_j A_{ji}} \sum_j \frac{A_{ji} m_j}{\sum_l A_{jl} t_l^{(k)}} \ .$$

The solution is guaranteed to converge to the maximum likelihood (noisy) solution in the limit of the infinite number of iterations [114]. The regularization for this approach is realized by restricting the number of iterations.

3.4.2 Response matrix construction

Knowledge of effects which shall be removed is encoded in the response matrix. In this analysis, two response matrices are used: one related to detector effects RM_{det} ($p_{\text{T,part}}^{\text{jet}}$, $p_{\text{T,det}}^{\text{jet}}$) and the second to residual UE fluctuations RM_{UE} ($p_{\text{T,det}}^{\text{jet}}$, $p_{\text{T,reco}}^{\text{jet}}$), where $p_{\text{T,part}}^{\text{jet}}$, denotes $p_{\text{T}}^{\text{jet}}$ at particle-level, $p_{\text{T,det}}^{\text{jet}}$– jet p_{T} measured with imperfect detector, while $p_{\text{T,reco}}^{\text{jet}}$ includes also effect of fluctuating UE. Both matrices are then combined as described later.

Detector response RM_{det} is built based on GEANT 3 simulations. Particle- and detector-level jets are matched geometrically, with a maximal allowed distance equal to $\Delta R = \sqrt{(\eta_{det} - \eta_{part})^2 + (\varphi_{det} - \varphi_{part})^2} = 0.25$. Except for the matrix describing migration between p_{T} bins, one needs to take into account particle-level jets which are not reconstructed (or not matched) at all: such probability is called reconstruction efficiency $\epsilon_{reco}(p^{\mathrm{jet}}_{\mathrm{T,part}})$. Moreover, one needs to take into account the kinematic efficiency, $\epsilon_{kine}(p^{\mathrm{jet}}_{\mathrm{T,part}})$, which is a probability that jet with given $p^{\mathrm{jet}}_{\mathrm{T,part}}$ will be measured with $p^{\mathrm{jet}}_{\mathrm{T,det}}$ falling inside the measured p_{T} range: $p^{\mathrm{jet}}_{\mathrm{T,det}} = 10$–$100\,\mathrm{GeV}/c$. Both efficiencies are shown together with RM_{det} in Fig. 3.10.

As a typical jet consists of several particles, the probability of missing it completely is rather low – ϵ_{reco} is close to one and falls slightly only for the lowest bins of $p^{\mathrm{jet}}_{\mathrm{T,part}}$. Kinematic efficiency drops rapidly outside of the measured $p^{\mathrm{jet}}_{\mathrm{T,det}}$ range. The final spectrum despite being unfolded in the wide range of $p^{\mathrm{jet}}_{\mathrm{T,part}}$ will be only reported in this narrower range, where the ϵ_{kine} is close to 1.

Due to finite tracking efficiency, measured jet p_{T} will be usually lower than its true value. $p^{\mathrm{track}}_{\mathrm{T}}$ resolution also smears significantly jet p_{T} in both directions. Examples of $p^{\mathrm{jet}}_{\mathrm{T,det}}/p^{\mathrm{jet}}_{\mathrm{T,part}}$ distributions are shown in the bottom left panel of Fig. 3.10. With normalization to $p^{\mathrm{jet}}_{\mathrm{T,part}}$, one can see that the detector response is actually quite similar across $p^{\mathrm{jet}}_{\mathrm{T,part}}$, which is not necessarily clear from the plot of RM_{det} . The average value of $p^{\mathrm{jet}}_{\mathrm{T,det}}/p^{\mathrm{jet}}_{\mathrm{T,part}}$ below 1 would suggest that the $p^{\mathrm{jet}}_{\mathrm{T,part}}$ spectrum will be less steep (will be on average higher) than $p^{\mathrm{jet}}_{\mathrm{T,det}}$. On the other hand, the jet p_{T} spectrum is steeply falling. If the detector response was symmetric, then the chance that a jet measured with given $p^{\mathrm{jet}}_{\mathrm{T,det}}$ originates from the upward fluctuation of jet with $p^{\mathrm{jet}}_{\mathrm{T,part}} < p^{\mathrm{jet}}_{\mathrm{T,det}}$ would be much higher than a chance of downward fluctuation from higher $p^{\mathrm{jet}}_{\mathrm{T,part}}$. It would result in average $p^{\mathrm{jet}}_{\mathrm{T,det}} > p^{\mathrm{jet}}_{\mathrm{T,part}}$. In practice, the first effect slightly dominates and the $p^{\mathrm{jet}}_{\mathrm{T,part}}$ is on average a bit larger ($p^{\mathrm{jet}}_{\mathrm{T,part}}$ spectrum is less steep or "harder") than $p^{\mathrm{jet}}_{\mathrm{T,det}}$.

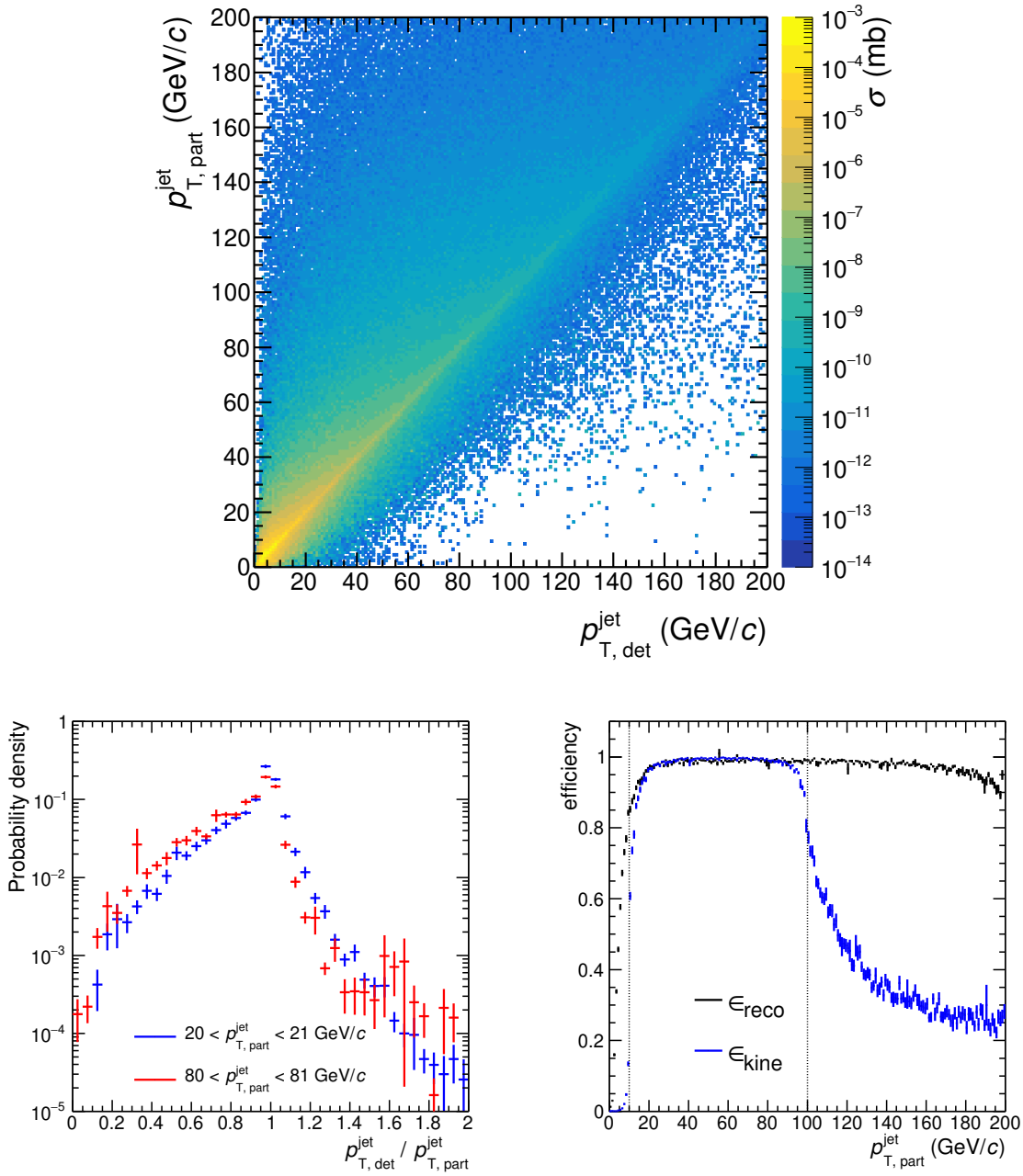

Figure 3.10: Detector response matrix RM_{det} (top), distributions of ratio ($p^{\mathrm{jet}}_{\mathrm{T,det}}/p^{\mathrm{jet}}_{\mathrm{T,part}}$) for two intervals of $p^{\mathrm{jet}}_{\mathrm{T,part}}$ (bottom left) and kinematic and reconstruction efficiencies (bottom right). The dotted vertical lines in the bottom right panel denote the reported range of the unfolded spectrum, $p^{\mathrm{jet}}_{\mathrm{T,part}} = 10$–$100\,\mathrm{GeV}/c$.

UE activity fluctuations Average UE contribution is subtracted from each jet p_{T} as described in Sec. 3.1.4. Still, the jet sample is affected by the fluctuations of the UE activity.

Two methods to estimate background fluctuations were explored. In the first one, track embedding, a single track is embedded in the real event at the same η, but φ rotated by 90° w.r.t. b-jet candidate axis. Transverse momentum smearing due to background fluctuations is then:

$$\delta p_{\mathrm{T}}^{\mathrm{emb}} = p_{\mathrm{T,emb}}^{\mathrm{jet}} - \rho A_j - p_{\mathrm{T}}^{\mathrm{emb.track}} \quad ,$$

where $p_{\mathrm{T,emb}}^{\mathrm{jet}}$ is p_{T} of the jet containing the embedded track, ρA_j is the subtracted average UE contribution and $p_{\mathrm{T}}^{\mathrm{emb.track}}$ is the p_{T} of the embedded track. This approach allows to study possible differences of background influence depending on $p_{\mathrm{T}}^{\mathrm{jet}}$ (by varying $p_{\mathrm{T}}^{\mathrm{emb.track}}$).

In the second method, called random cones (RC), the jet cone with radius R_{cone} equal to R of analysed jets is placed randomly in the detector acceptance (the cone should be fully contained in the acceptance and not overlap with any of the two leading jets). Background fluctuations estimated with RC method are then given by:

$$\delta p_{\mathrm{T}}^{\mathrm{RC}} = \sum_{\text{track} \in \text{RC}} p_{\mathrm{T}}^{\mathrm{track}} - \rho \pi R_{\mathrm{cone}}^2 \ ,$$

where the sum runs over tracks found within R_{cone} from a randomly chosen axis.

Both methods provide in principle 1D distribution of δp_{T}, which characterizes the sample of events and not the sample of jets. To obtain the response matrix, the distributions are shifted along the diagonal, with zero of the δp_{T} distribution placed at point where $p_{\mathrm{T,reco}}^{\mathrm{jet}} = p_{\mathrm{T,det}}^{\mathrm{jet}}$. Formally: $RM_{UE}(i,j) = \sum_k u(k)\ \delta(j-i-k+k_0)$, where $RM_{UE}(i,j)$ is the j-th column of i-th row of RM_{UE}, $\delta(i)$ is the Kronecker δ function (equal 1 if $i = 0$ and 0 if $i \neq 0$), $u(k)$ is the content of k-th bin of δp_{T} histogram and k_0 is the index of bin containing value $\delta p_{\mathrm{T}} = 0\,\mathrm{GeV}/c$. Both 1D distributions of δp_{T} and constructed from it RM_{UE} are shown in Fig. 3.11. To suppress statistical fluctuations, tails of the δp_{T} distributions — range 8–20 GeV/c (5–10 GeV/c) for RC method and embedding with $p_{\mathrm{T}}^{\mathrm{track}} > 10\,\mathrm{GeV}/c$ (embedding with $p_{\mathrm{T}}^{\mathrm{track}} < 10\,\mathrm{GeV}/c$) — are first fitted with an exponential function.

The embedding method was used to obtain the main result of the analysis, while RC method was utilized as a systematic variation.

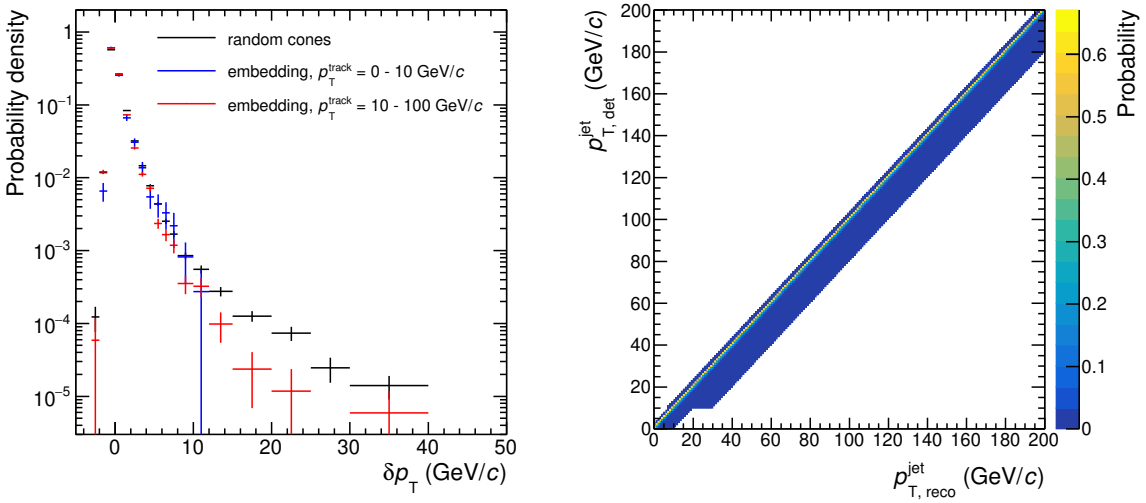

Figure 3.11: Left: the distribution of local UE fluctuations δp_{T} obtained with two methods (see text for details). Right: RM_{UE} obtained with the track embedding method.

Combined response matrix Response matrices related to detector effects and background fluctuations are combined into one response matrix by multiplication of both matrices (the effects they represent are assumed to be independent). Obtained response matrix needs to be rebinned and then normalized. Binning of the response matrix is equal to binnings used in the input spectrum and the final, unfolded spectrum. They are determined based on two main factors: resolution (too much populated off-diagonal bins may result in unstable results) and available statistics (roughly 10 entries are required) in each bin of input spectrum

for successful unfolding. In this analysis, additionally, the input spectrum binning must allow for template fitting which at higher p_{T} bins is challenging due to the limited data sample size (see Sec. 3.3).

Binning used in this analysis are following:

- input spectrum: $p_{\mathrm{T,det}}^{\mathrm{jet}} = 10, 15, 20, 25, 30, 35, 40, 50, 70, 100$ GeV/c
- unfolded spectrum: $p_{\mathrm{T,part}}^{\mathrm{jet}} = 0, 10, 20, 30, 40, 50, 60, 70, 100, 200$ GeV/c

where fist and last bins of the unfolded spectrum are not reported in the final spectrum, but are important for the stability of the method.

After the rebinning of the response matrix, it has to be normalized to reflect the probability of a jet with a certain $p_{\mathrm{T,part}}^{\mathrm{jet}}$ to be reconstructed at $p_{\mathrm{T,reco}}^{\mathrm{jet}}$. Each distribution for a given $p_{\mathrm{T,part}}^{\mathrm{jet}}$ bin (row) is then normalized to unity. The combined response matrix obtained from multiplication RM_{det} and RM_{UE} , as well as its rebinned and normalized versions, are shown in Fig. 3.12.

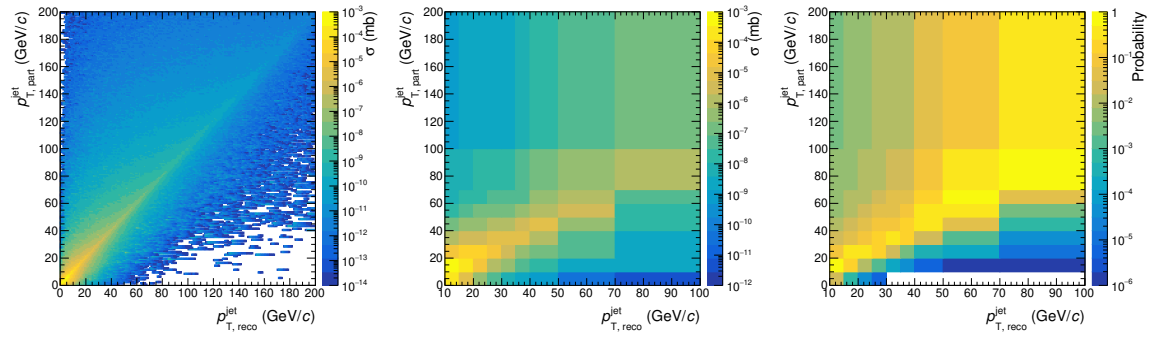

Figure 3.12: Combined response matrix $RM_{\mathrm{comb}} = RM_{\mathrm{det}} \times RM_{\mathrm{UE}}$ (left) as well as its rebinned (center) and normalized version (right).

3.4.3 Unfolding of b-jet spectrum

The measured b-jet spectrum was obtained as the sample of jets reconstructed in data, tagged by the ML model and corrected for tagging purity and efficiency. b-jet spectrum from PYTHIA (POWHEG as systematic variation) was used as the prior distribution in the default analysis. Technically, the prior is enforced by reweighting the response matrix. Together with the normalized response matrix and (reconstruction and kinematic) efficiencies described above, they were the input to the unfolding procedure. The procedure was performed with SVD method ("iterative Bayes" as a systematic variation). The unfolded spectrum is given by:

$$\frac{\mathrm{d}N_{\mathrm{unfolded}}}{\mathrm{d}p_{\mathrm{T}}^{\mathrm{jet}}} = \mathrm{Unfold}\left(\frac{\mathrm{d}N_{\mathrm{tagged}}}{\mathrm{d}p_{\mathrm{T}}^{\mathrm{jet}}} \cdot \frac{P_{\mathrm{tag}}}{\epsilon_{\mathrm{tag}}}\right) \frac{1}{\epsilon_{\mathrm{reco}}\epsilon_{\mathrm{kine}}} \quad .$$

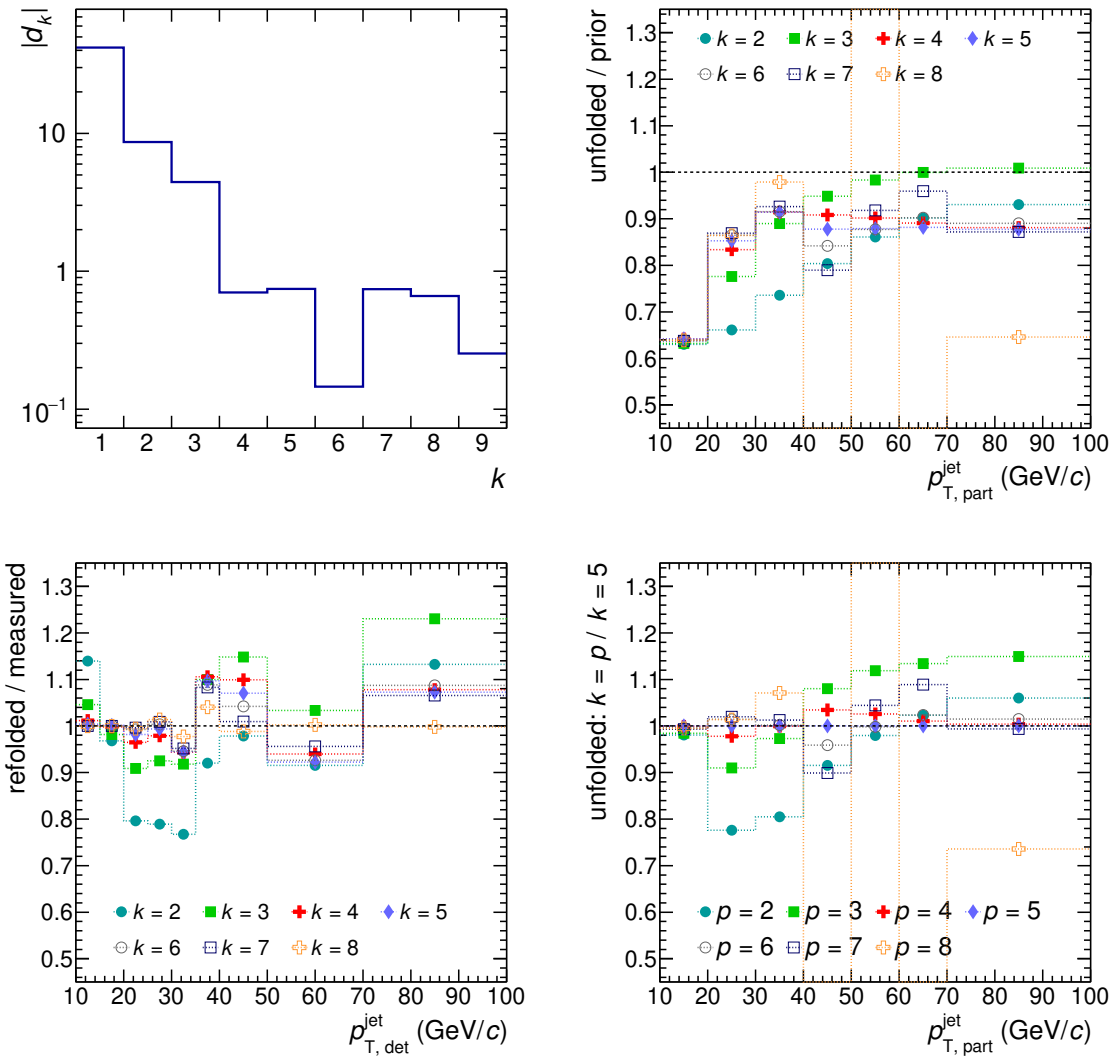

Figure 3.13: Top left: distribution of d_k values (defined in Eq. 3.3). Top right: ratios of unfolded spectra obtained with various values of k to prior distribution. Bottom left: ratios of refolded spectra to the measured spectrum. Bottom right: ratios of unfolded spectra obtained with various k to the one obtained with k selected in the default analysis.

The SVD unfolding requires the choice of regularization parameter k. Its value was chosen based on several, non-sharp criteria, namely:

- it should be close to the index of last significant d_k, all d_k have by construction estimated errors equal to ± 1 [111] (Fig. 3.13, top left)
- results of unfolding with increasing k should converge close the selected value of k (Fig. 3.13, top right and bottom right)
- refolded spectrum (unfolded and then folded again with the same response matrix) should be compatible with the measured input spectrum (Fig. 3.13, bottom left)
- correlations between bins should be limited – often there is a transition from positive to negative correlation between neighbouring bins as the regularization strength decreases (k increases) (Fig. 3.14)

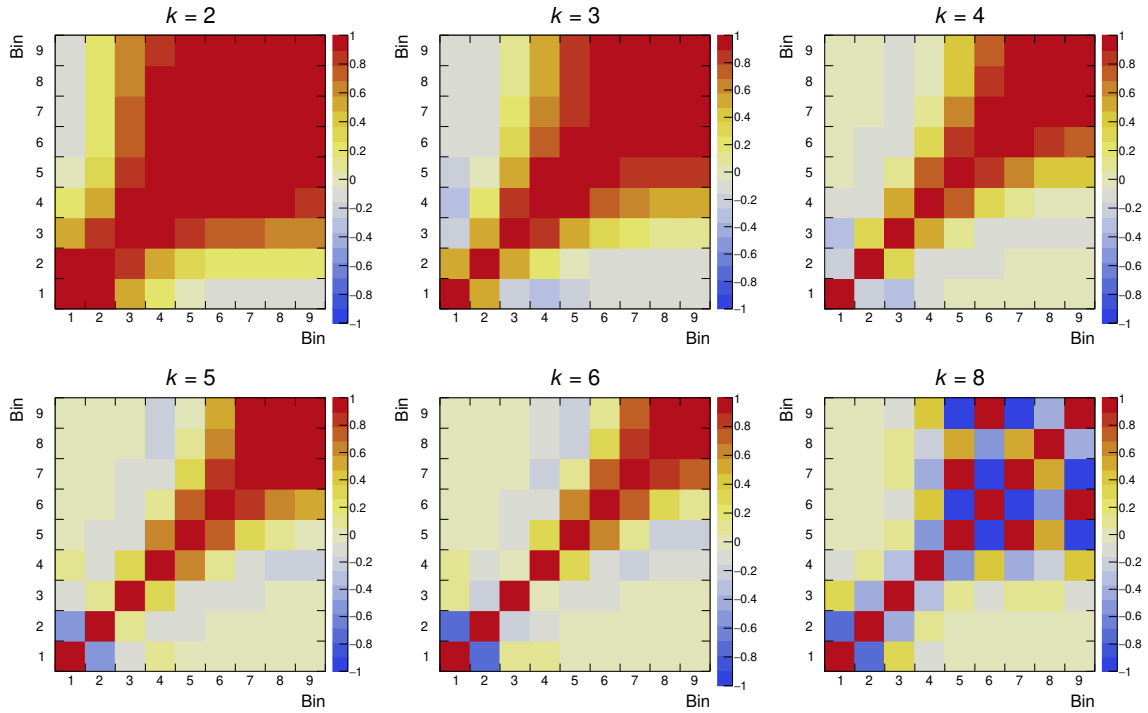

Figure 3.14: Bin-to-bin Pearson correlation of the unfolded spectrum obtained with various values of parameter k.

Based on these, the default value of regularization parameter was selected to equal $k = 5$. The unfolded spectrum is compared to prior distribution as well as the measured and refolded spectra in Fig. 3.15

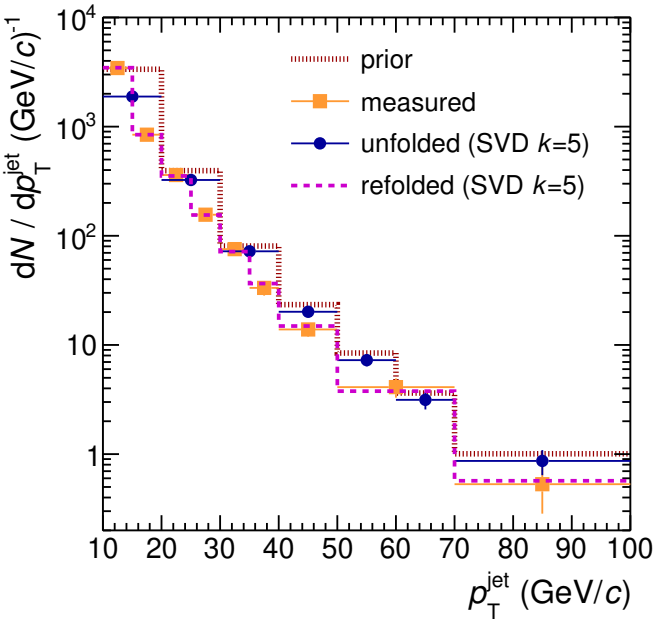

Figure 3.15: Measured and unfolded spectra compared to the refolded and the prior distributions. Note that the measured and refolded spectra have binning of $p^{\text{jet}}_{\text{T,det}}$ while prior and unfolded spectra of $p^{\text{jet}}_{\text{T,part}}$.

3.5 Scaling to the b-jet cross section

To get the b-jet production cross section $\frac{\mathrm{d}\sigma_{b\text{-jet}}}{\mathrm{d}p_{\mathrm{T}}^{\mathrm{jet}}}$, the unfolded spectrum of number of b-jets $\frac{\mathrm{d}N_{b\text{-jet}}^{\mathrm{unfolded}}}{\mathrm{d}p_{\mathrm{T}}^{\mathrm{jet}}}$ has to be divided by the integrated luminosity $\mathcal{L}$.

In ALICE, luminosity is not measured directly. The cross sections are determined based on a comparison with the visible cross section σ_{vis} measured in van der Meer (vdM) scans. The visible cross section is the cross section of the reference process σ_{vis} visible by a given detector and satisfying some trigger logic. Luminosity is then the reference-process rate divided by σ_{vis}. The whole procedure for the analysed data set is described in [77]. The visible cross section measured with V0 detector was $\sigma_{\mathrm{vis}} = 50.87 \pm 0.04(\mathrm{stat.}) \pm 1.07(\mathrm{sys.})$ mb..

The MB trigger used during the collection of the analysed data was a requirement of coincidence between two sides of the V0 detector. The same logic was set to define the reference process used in σ_{vis} determination. Number of reference-process events $N_{\mathrm{ref\ evt}}$ can be then substituted with the number of MB events N_{MB}:

$$\frac{\mathrm{d}\sigma_{b\text{-jet}}}{\mathrm{d}p_{\mathrm{T}}^{\mathrm{jet}}} = \frac{1}{\mathcal{L}} \frac{\mathrm{d}N_{b\text{-jet}}^{\mathrm{unfolded}}}{\mathrm{d}p_{\mathrm{T}}^{\mathrm{jet}}} = \frac{\sigma_{\mathrm{vis}}}{N_{\mathrm{ref\ evt}}} \frac{\mathrm{d}N_{b\text{-jet}}^{\mathrm{unfolded}}}{\mathrm{d}p_{\mathrm{T}}^{\mathrm{jet}}} = \frac{\sigma_{\mathrm{vis}}}{N_{\mathrm{MB}}} \frac{\mathrm{d}N_{b\text{-jet}}^{\mathrm{unfolded}}}{\mathrm{d}p_{\mathrm{T}}^{\mathrm{jet}}} \quad .$$

The b-jets are measured only in events which have $|z_{\mathrm{vtz}}| < 10\,\mathrm{cm}$. There is no such requirement during measurement of σ_{vis}, therefore N_{MB} has to be replaced with N_{MB}^{10} – number of MB events with z_{vtx} within 10 cm from the nominal interaction point. It implicitly assumes that the b-jet production cross section is independent on z_{vtx}:

$$\frac{\mathrm{d}\sigma_{b\text{-jet}}}{\mathrm{d}p_{\mathrm{T}}^{\mathrm{jet}}} = \frac{\sigma_{\mathrm{vis}}}{N_{\mathrm{MB}}^{10}} \frac{\mathrm{d}N_{b\text{-jet}}^{\mathrm{unfolded}}}{\mathrm{d}p_{\mathrm{T}}^{\mathrm{jet}}} \quad .$$

Next, not all events accounted for in N_{MB}^{10}, have reconstructed primary vertex – there are events with "true" $|z_{\mathrm{vxz}}| < 10\,\mathrm{cm}$ for which vertex is not reconstructed:

$$N_{\mathrm{MB}}^{10} = N_{\mathrm{MB}}^{10,\ \mathrm{vtx}} + N_{\mathrm{MB}}^{10,\ \mathrm{no\text{-}vtx}} \quad .$$

By definition, their number cannot be known, so it is assumed that the efficiency of reconstructing the primary vertex ϵ_{vtx} is the same for $|z_{\mathrm{vtx}}|$ below and above 10 cm. In other words, the fraction of events which have $|z_{\mathrm{vtz}}| < 10\,\mathrm{cm}$ is assumed to be the same for events with and without the reconstructed vertex:

$$\frac{N_{\mathrm{MB}}^{10,\ \mathrm{vtx}}}{N_{\mathrm{MB}}^{\mathrm{vtx}}} = \frac{N_{\mathrm{MB}}^{10,\ \mathrm{no\text{-}vtx}}}{N_{\mathrm{MB}}^{\mathrm{no\text{-}vtx}}} \quad .$$

It gives:

$$N_{\mathrm{MB}}^{10} = N_{\mathrm{MB}}^{10,\ \mathrm{vtx}} + N_{\mathrm{MB}}^{\mathrm{no\text{-}vtx}} \cdot \frac{N_{\mathrm{MB}}^{10,\ \mathrm{vtx}}}{N_{\mathrm{MB}}^{\mathrm{vtx}}} = N_{\mathrm{MB}}^{10,\ \mathrm{vtx}} \left(\frac{N_{\mathrm{MB}}^{\mathrm{vtx}} + N_{\mathrm{MB}}^{\mathrm{no\text{-}vtx}}}{N_{\mathrm{MB}}^{\mathrm{vtx}}} \right) = \frac{N_{\mathrm{MB}}^{10,\ \mathrm{vtx}}}{\epsilon_{\mathrm{vtx}}} = N_{\mathrm{MB}}^{10,\ \mathrm{vtx}} \cdot C_{\mathrm{vtx}} \quad ,$$

with C_{vtx} being the vertex reconstruction correction factor. Based on values from Table 3.1 (only events passing pile-up cut are considered), it is equal to $1054.1 \times 10^6/(1001.0 \times 10^6) = 1.053$. $N_{\mathrm{MB}}^{10,\ \mathrm{vtx}}$ is equal to the number of accepted events: $N_{\mathrm{acc}} = 910.8 \times 10^6$ (last column in Table 3.1).

The b-jet spectrum is also scaled by allowed η_{jet} range: $|\eta_{\mathrm{jet}}| < (\eta_{\mathrm{TPC}} - R) = 0.9 - 0.4 = 0.5$. η_{TPC} is the fiducial TPC acceptance equal 0.9. For $R = 0.4$ it corresponds to factor 1 and has no impact here, but allows for straightforward comparison with measurements taken at different jet radii or by other experiments.

Final b-jet production cross section is given by:

$$\frac{\mathrm{d}^2\sigma_{b\text{-jet}}}{\mathrm{d}p_{\mathrm{T}}^{\mathrm{jet}}\mathrm{d}\eta_{\mathrm{jet}}} = \frac{\sigma_{\mathrm{vis}}}{C_{\mathrm{vtx}}\,N_{\mathrm{acc}}}\frac{\mathrm{d}N_{b\text{-jet}}^{\mathrm{unfolded}}}{\mathrm{d}p_{\mathrm{T}}^{\mathrm{jet}}} \quad ,$$

with $C_{\mathrm{vtx}} = 1.053$, $N_{\mathrm{acc}} = 910.8 \times 10^6$ events and $\sigma_{\mathrm{vis}} = 50.87 \pm 0.04(\text{stat.}) \pm 1.07(\text{sys.})$ mb.

3.6 Systematic uncertainties

Systematic uncertainties related to various aspects of the analysis were evaluated at the level of the unfolded spectrum. The normalization described in Sec. 3.5 is only scaling of the whole spectrum by a constant factor, so it does not impact the fractional differences. If not stated otherwise, the uncertainties are treated as asymmetric.

Each of the following subsections contains one group of uncertainties, which are further treated as independent and added in quadrature. All the values of systematic uncertainties are shown in Fig. 3.24 and in Table 3.3 at the end of this section.

Procedure This section aims to quantify *systematic* uncertainties of the final result. To estimate systematic uncertainties, toy-measured spectra are used to reduce the effect of statistical fluctuations that affect the input spectrum.

First, the toy spectrum is generated and processed with the default settings and selected systematic variations. The toy spectra are produced by generating random numbers from the standard normal distribution and independently varying the bin contents of the measured spectrum by its statistical uncertainty σ_{stat} multiplied by these random numbers. Next, the ratio of the default to varied unfolded results is computed. The procedure is repeated 100 times. The mean and standard deviation of the sample of ratios are used to assess systematic uncertainty.

The systematic variations were considered on two stages (A) at the level of the already created measured spectrum (*e.g.* modifications of the response matrix or unfolding parameters) (B) at the generating level of the measured spectrum (*e.g.* working point selection). In the first case, systematic uncertainty is determined by comparing the unfolded results obtained from two identical toy spectra with different unfolding. In the second case, if the changes affect the creation of the measured spectrum, the statistical fluctuations are taken as fully correlated between the two toy spectra.

Fig. 3.16 shows the demonstrations of the described procedure for two exemplary cases. The 2D histograms accumulate the ratios between the unfolded spectra obtained with varied and default settings, bin-by-bin. Their bin-wise means and standard deviations are shown as black points. They are compared to the blue points – "not randomized" case where the original measured spectrum was used without generating toys. Its error bars correspond to the statistical uncertainties. As it can be seen from the plot related to tracking efficiency, sometimes even in the p_{T} range affected by large statistical fluctuations, the systematic variation may provide a well-defined shift, with a small spread between different toy spectra. In other cases, like for SVD unfolding with modified regularization parameter $k = 6$, the spread between toys is significant.

All the values and error bars shown in the next sections describing consecutive systematic variations correspond to the means and standard deviations of the ensembles of ratios collected with toy spectra – they are equivalent to black points in Fig. 3.16. If the error bars are not visible, they are smaller than the markers.

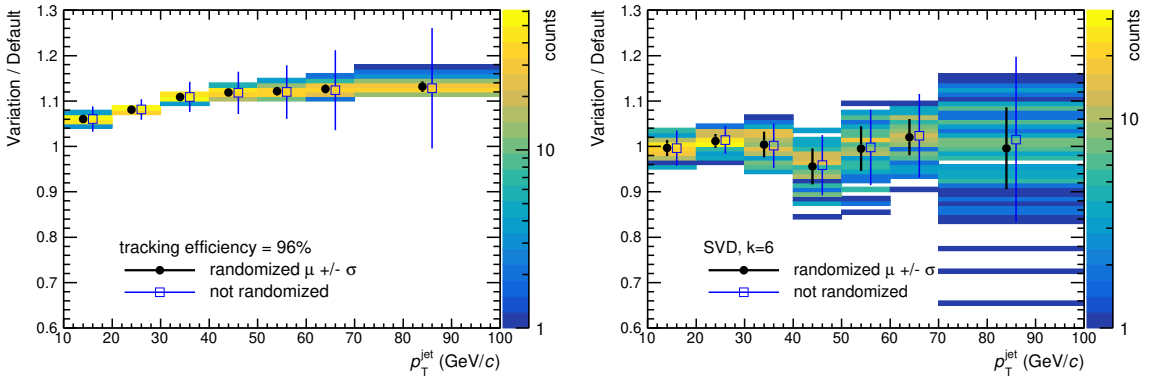

Figure 3.16: Results of the procedure used to estimate systematic uncertainties for two exemplary systematic variations: lowering tracking efficiency (left) and changing regularization parameter k in SVD unfolding from $k = 5$ to $k = 6$ (right).

3.6.1 Tracking efficiency

The uncertainty of the tracking efficiency in ALICE can be assessed by varying the track selection parameters and ITS-TPC matching requirements. Its value is estimated to 4% [115]. It impacts the average shift between the particle and the detector-level jet p_{T} (JES). The related uncertainty on the final b-jet spectrum is assessed using an alternative response matrix constructed by randomly rejecting 4% of the reconstructed tracks. Artificial enhancement of the tracking efficiency is hard to implement, therefore it is assumed that enhancement and reduction of efficiency act symmetrically.

Fig. 3.17 shows the ratio to the result obtained with the default response matrix. The uncertainty is taken as the difference in each bin and symmetrized (to account for the tracking efficiency enhancement).

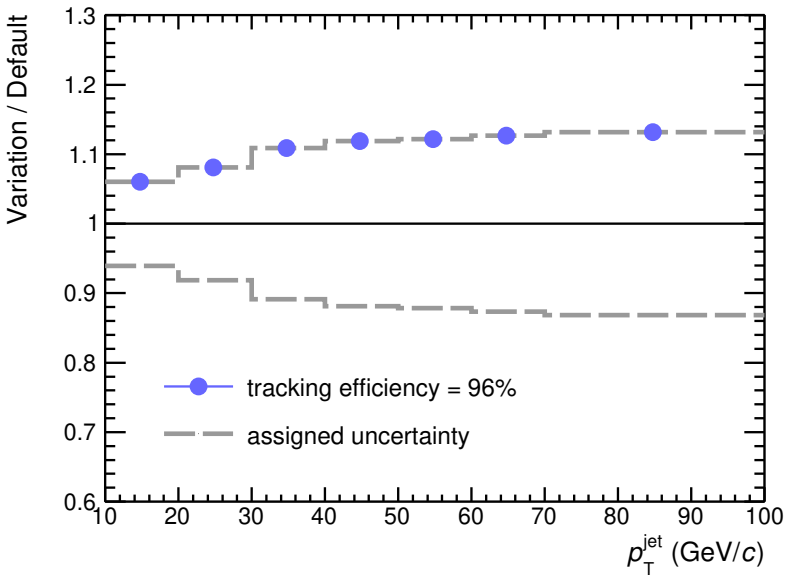

Figure 3.17: The ratio of the spectrum obtained with the lowered tracking efficiency to the default analysis spectrum. The gray dashed line shows the final uncertainty values assigned to tracking efficiency.

3.6.2 Underlying event fluctuations

Fluctuations of the UE in the default analysis were estimated using the track embedding method, with $p_{\text{T}}^{\text{emb.track}}$ split into two ranges: 0–10 and 10–100 GeV/c. Two systematic variations were used: the random cones method and the embedding method with a single range of 0–100 GeV/c. A new RM_{UE} was created each time, followed by a new combined response matrix. Effects of both variations are shown in Fig. 3.18 The uncertainty was taken as the maximum deviation (envelope) from both variations in each bin.

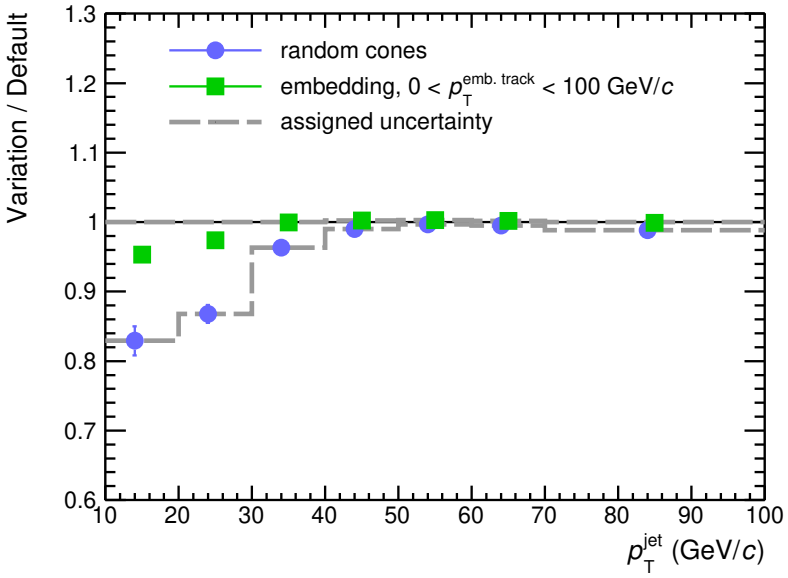

Figure 3.18: The ratio of the spectrum obtained with the alternative RM_{UE} to the default analysis spectrum. The gray dashed line shows the final uncertainty values assigned to UE fluctuations.

3.6.3 Working point selection

The working point of the b-jet tagger in the default settings was defined as $p_{\text{T}}^{\text{jet}}$-dependent cut, which in MC yields a b-jet sample with a fixed purity of 70%. The systematic variations include alternative purity values (30%, 40%, 50%, 60%, 80%, and 90%) and defining the thresholds by the fixed tagging efficiency instead of purity (ϵ_{tag} = 60% and 80%). Effects of these variations are shown in Fig. 3.19. Changing the working point selection requires a new purity estimation using template fitting, therefore obtained result have some hard-to-eliminate component of statistical fluctuations. The fitted data also partially correlated and the obtained values do not seem to follow normal distribution. They are then modelled as a uniform distribution.

As the considered variations cover pretty much the entire space of reasonable variations (and irreducible statistical fluctuations additionally spread them out) obtained values are assumed to provide good coverage of the extreme cases. Therefore, the assigned (asymmetric) uncertainty is taken as the range from smallest to largest deviation in each bin (envelope), narrowed by a factor of $\sqrt{3}$ to obtain an estimate of one σ.

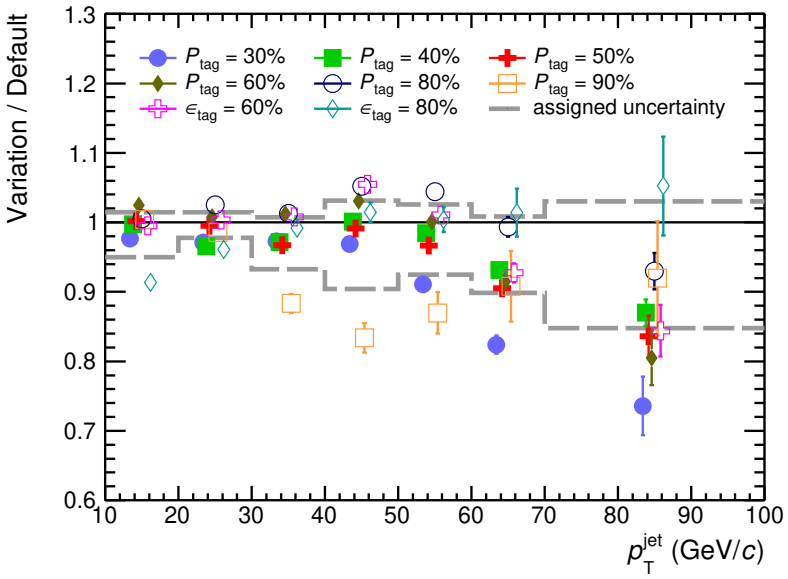

Figure 3.19: The ratio of the spectrum obtained with the alternative choice of tagger working point to the default analysis spectrum. It includes variation of tagging purity P_{tag} from 30% to 90% and switch to selection based on constant tagging efficiency $\epsilon_{\text{tag}} = 60\%$ and 80%. The gray dashed line shows the final uncertainty values assigned to the working point selection.

3.6.4 Measured spectrum binning

The default binning of the measured spectrum was varied while preserving the binning of the unfolded spectrum. Also the overall range of the measured spectrum – left (right) edge of the first (last) bin – were left unchanged. Four alternative binnings were used:

- all inner bin edges are shifted alternately left and right by 1 GeV/c (labelled "LR"), yielding binning: 10, 14, 21, 24, 31, 34, 41, 49, 71, 100 GeV/c
- same as above but in inversed order (labelled "RL"), yielding binning: 10, 16, 19, 26, 29, 36, 39, 51, 69, 100 GeV/c
- all inner bin edges shifted to the left by around 20% of bin width (labelled "LL"), yielding binning: 10, 14, 19, 24, 29, 34, 39, 48, 66, 100 GeV/c
- same as above but right (labelled "RR"), yielding binning: 10, 16, 21, 26, 31, 36, 41, 52, 74, 100 GeV/c

Alternative binning of the measured spectrum requires new estimates of the tagging purity and efficiency. The template fitting method suffers from limited statistical precision which convoluted into binning modification enhances the estimated uncertainty. Therefore, both tagging efficiency and purity were parametrized with $f(p_{\text{T}}^{\text{jet}}) = a + b \cdot (p_{\text{T}}^{\text{jet}})^{-1} + c \cdot (p_{\text{T}}^{\text{jet}})^{-2}$ and constant function respectively as shown in Fig. 3.20. To study solely the effects of the binning, also the reference result to which the variations were compared, was obtained using the values from these parameterizations.

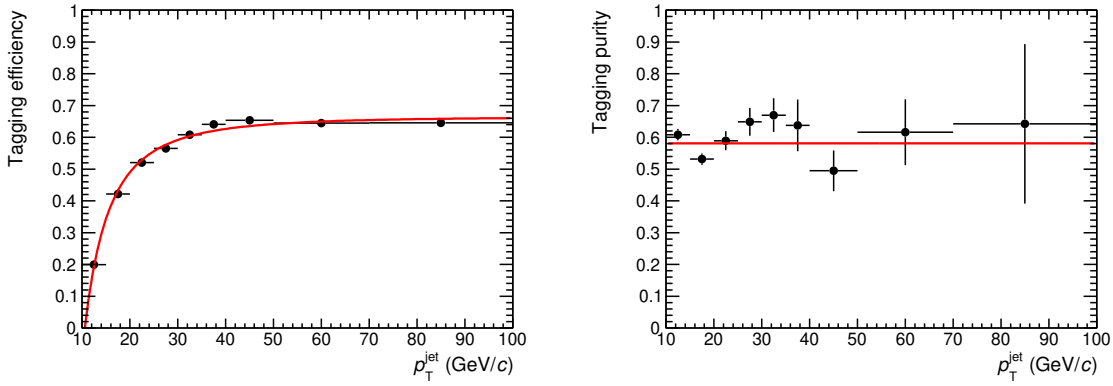

Figure 3.20: Tagging efficiency (left) and purity (right) as a function of $p_{\mathrm{T}}^{\mathrm{jet}}$ together with their parameterizations used to study the effect of alternative binning in the measured spectrum.

A comparison of results obtained with the alternative binnings and the default one is shown in Fig. 3.21. The (symmetric) uncertainty in each bin is taken as the standard deviation of all four variations.

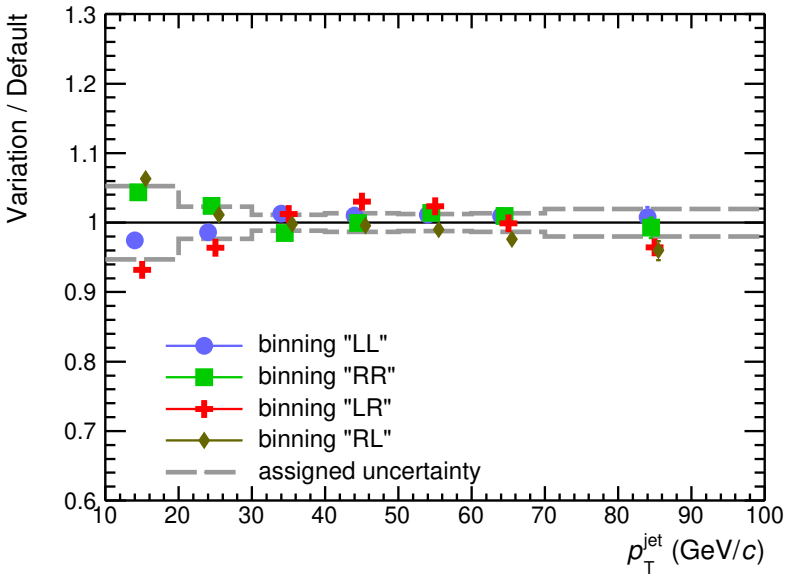

Figure 3.21: The ratio of the spectrum obtained with the alternative binnings of the measured spectrum to the default analysis spectrum. All the spectra were obtained with parametrized tagging purity and efficiency, see text for details. The gray dashed line shows the final uncertainty values assigned to the binning variation.

3.6.5 Unfolding

The settings and parameters of the unfolding procedure itself were varied in the following aspects:

- prior distribution was changed from the one predicted by PYTHIA to POWHEG dijet simulation [116, 117] simulations taken from [107]
- regularization parameter in SVD unfolding was varied by ± 1, to $k = 4$ and $k = 6$
- unfolding was performed with the "iterative Bayes" method instead of SVD

Unfolding with the "iterative Bayes" appeared to give much more stable results after adding an additional underflow (not-reported) low-$p_{\mathrm{T,part}}^{\mathrm{jet}}$ bin (0–5 GeV/c). However, the SVD method requires the same number of bins in the measured and unfolded spectra. Two options listed below were studied.

- SVD preserves its original binning:
  0, 10, 20, 30, 40, 50, 60, 70 , 100, 200 GeV/c
  and Bayes has different binning:
  0, 5, 10, 20, 30, 40, 50, 60, 70, 100, 200,
  but the same in the reported range 10–100 GeV/c. This is labelled as "different binning".
- both methods have two underflow bins but bins 50–60 and 60–70 GeV/c were merged to keep the same number of bins for the SVD. Then both have the same binning:
  0, 5, 10, 20, 30, 40, **50, 70**, 100, 200 GeV/c.
  This is labelled as "same binning"

Two approaches to unfold with "iterative Bayes" are show in Fig. 3.22. In both cases, the deviations from the default result in some bins suffer from variance much larger than the mean effect of the systematic variation. Nonetheless, as the mean deviations are significantly different from zero (standard error on the mean is $\sqrt{N_{toys}} = 10$ times smaller than the displayed standard deviations) and they are treated as the best estimate of the systematic shift. For each bin the larger deviation from the two approaches is selected as the assigned uncertainty related to change of unfolding algorithm from SVD to "iterative Bayes".

Impacts of all the introduced variations (one value per bin for "iterative Bayes") are shown in Fig. 3.23. They cannot be treated as independent because most of them are mutually exclusive. No clear dependence of the magnitude of the deviations on the jet p_{T} is visible from the plot. Also, some degree of correlation between bins was a feature of the unfolding procedure. Hence, the deviations in individual bins should not be treated as independent. Based on these observations, a common, symmetric uncertainty across the whole p_{T} range was assigned. In each bin the largest deviation is chosen and they were averaged over the bins.

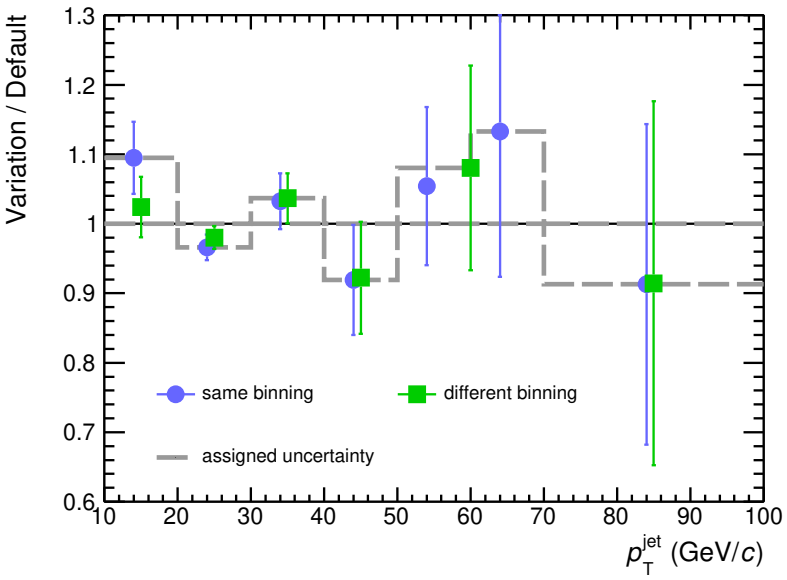

Figure 3.22: The ratio of the spectrum obtained with the iterative Bayes unfolding to the default analysis spectrum from SVD unfolding, see text for details. The gray dashed line shows the uncertainty values assigned to the change of unfolding algorithm and used in Fig. 3.23 ("Bayes").

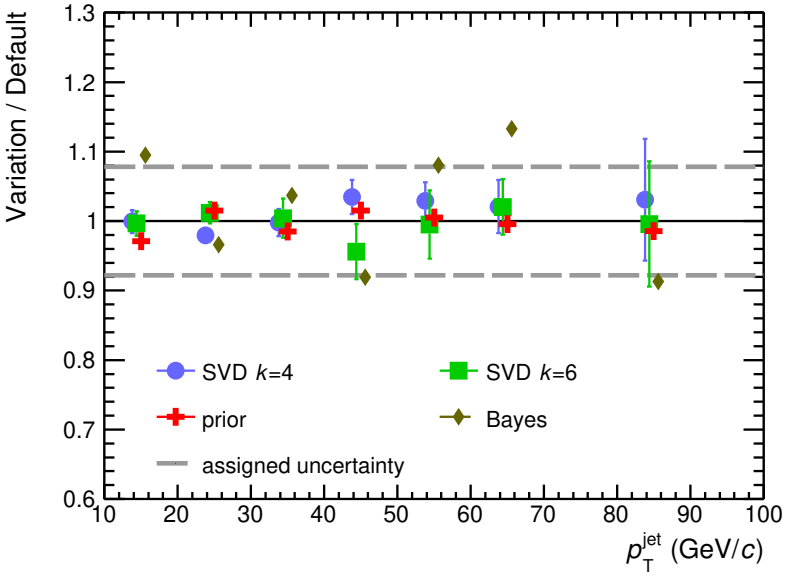

Figure 3.23: The ratio of the spectrum obtained with the alternative unfolding settings to the default analysis spectrum. The gray dashed line shows the final uncertainty values assigned to the unfolding procedure.

3.6.6 Total systematic uncertainties

The estimated contributions to the total systematic uncertainty were summarized in Table 3.3 and displayed in Fig. 3.24. Total systematic uncertainties were evaluated by adding individual systematic uncertainty components in quadrature.

Table 3.3: The summary of the systematic uncertainties related to individual contributions and the total systematic uncertainty. Normalization systematic uncertainty related to luminosity determination is quoted separately.

	$p_{\mathrm{T}}^{\mathrm{jet}}$ (GeV/c)						
	10 – 20	20 – 30	30 – 40	40 – 50	50 – 60	60 – 70	70 – 100
UE fluctuations (%)	−17/+0	−13/+0	−4/+0	−1/+0	−0/+0	−1/+0	−1/+0
Tracking efficiency (%)	±6	±8	±11	±12	±12	±13	±13
Working point (%)	−5/+1	−2/+1	−7/+1	−10/+3	−8/+3	−10/+1	−15/+3
Binning (%)	±5	±2	±1	±1	±1	±1	±2
Unfolding (%)	±8	±8	±8	±8	±8	±8	±8
Total systematic (%)	−21/+11	−18/+12	−15/+13	−17/+15	−16/+15	−18/+15	−22/+16
Normalization (%)	±2.1						

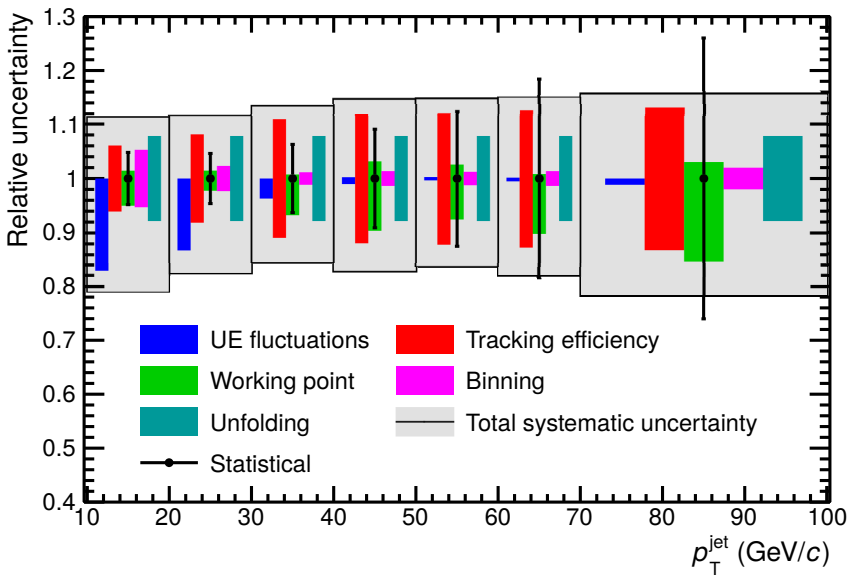

Figure 3.24: The summary of the assigned systematic uncertainties, shown as deviations from 1. Colorful bars, gray boxes, and error bars show individual contributions from different sources, total systematic uncertainty, and statistical uncertainties, respectively.

3.7 Results and discussion

3.7.1 p_{T}-differential cross section of charged-particle b-jets

The final p_{T}-differential cross section of charged-particle b-jets measured in pp collisions at $\sqrt{s} = 5.02\,\text{TeV}$ is shown in Fig. 3.25.

It is compared to NLO pQCD predictions obtained with POWHEG+PYTHIA [116, 117] simulations taken from [107]. The uncertainties of model predictions were obtained by varying the strong coupling constant α_s from 0.111 to 0.123 and increasing and decreasing the renormalization and factorization scales by a factor of 2.

The model describes very well the data, far within the uncertainties for $p_{\text{T}}^{\text{jet}} > 20$ with some tension appearing at $p_{\text{T}}^{\text{jet}} < 20\,\text{GeV}/c$. The model predictions in this first bin are above the data but still match within the combined uncertainties.

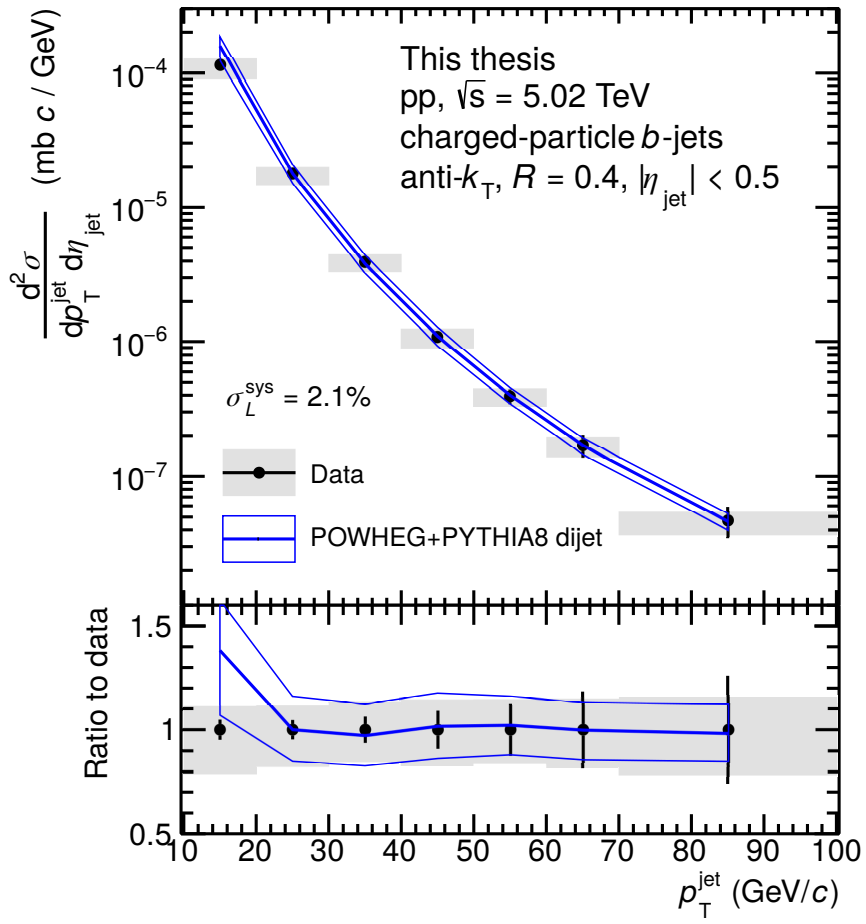

Figure 3.25: Top panel: differential production cross section of charged-particle, anti-k_{T} $R = 0.4$ b-jets measured in pp collisions at $\sqrt{s} = 5.02\,\text{TeV}$. Gray boxes and error bars show its systematic and statistical uncertainties, respectively. Additional normalization uncertainty of σ_L^{sys} 2.1% is not included. Blue lines correspond to NLO pQCD predictions from POWHEG dijet with PYTHIA8 fragmentation, see text for details. Bottom panel: ratio of POWHEG+PYTHIA8 predictions to the data.

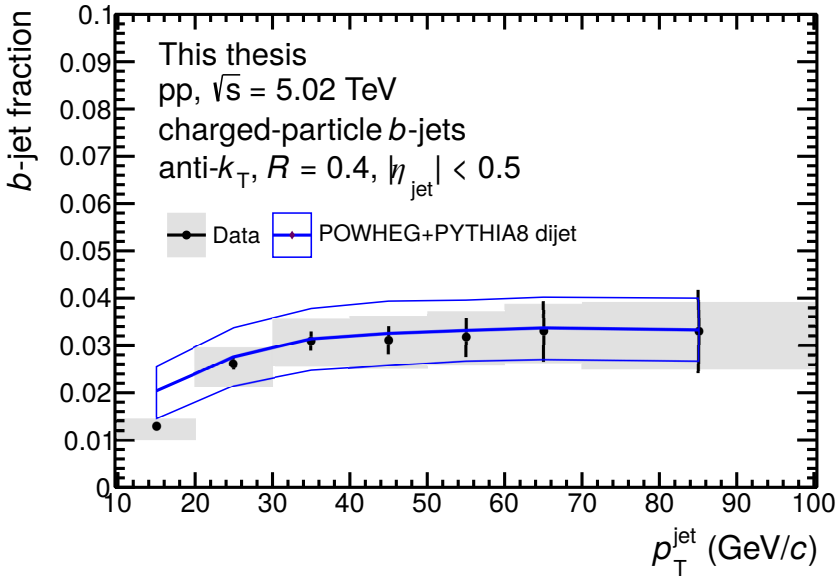

Figure 3.26: Ratio of b-jet to inclusive, untagged jets production cross sections from [88], compared with NLO pQCD predictions from POWHEG dijet with PYTHIA8 fragmentation, see text for details.

3.7.2 b-jet fraction

Fig. 3.26 shows the b-jet fraction defined as the ratio of the obtained b-jet cross section with the cross section of untagged inclusive charged jets from [88]. The compared cross sections were determined based on the separate data samples, collected in 2017 (b-jets) and 2015 (inclusive, untagged jets). Both the statistical and systematic uncertainties are treated as independent. In the latter case, it could be subject to some optimization, especially tracking efficiency which is the dominating uncertainty source in both measurements is at least partially correlated. The b-jet fraction grows with $p_{\mathrm{T}}^{\mathrm{jet}}$ from the level of 1–1.5 % at $p_{\mathrm{T}}^{\mathrm{jet}} = 10\,\mathrm{GeV}/c$ to 2.5–4 % at $p_{\mathrm{T}}^{\mathrm{jet}} = 30\,\mathrm{GeV}/c$ and then saturates or minimally rises. It is compared with POWHEG+PYTHIA8 simulations, which predict a similar trend.

Fig. 3.27 compares the same data with the results from other LHC experiments: ATLAS [69] and CMS [118]. Note that both ATLAS and CMS results are for full jets – taking also into account the component from neutral particles (very roughly corresponding to a shift by a 50% of $p_{\mathrm{T}}^{\mathrm{jet}}$ compared to charged jets measured by ALICE). Note also the differences in $\sqrt{s}$, the measured jet R and covered η ranges. Nonetheless, all three experiments are consistent within the uncertainties, showing a consistent rise of b-fraction from 1% to 4% in $p_{\mathrm{T}}^{\mathrm{jet}}$ range from 10 to 300 GeV/c.

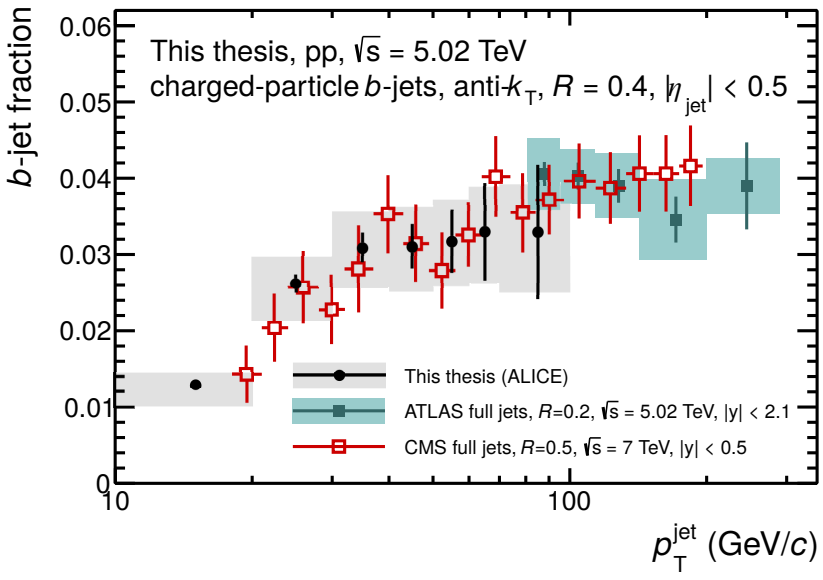

Figure 3.27: Ratio of b-jet to inclusive, untagged jets production cross sections from [88], compared with results from ATLAS [69] and CMS [118]. Error bars for CMS data points represent the combined statistical and systematic uncertainties. Note the differences in $\sqrt{s}$, jet R, and (pseudo)rapidity coverage, as well as the fact that the charged jets from ALICE are compared to full jets from ATLAS and CMS.

3.8 Summary and outlook

In this chapter, an analysis of b-jets using a novel procedure was described. The analysed data were collected in pp collisions at $\sqrt{s} = 5.02$ TeV – a very important dataset for ALICE due to its potential as a baseline for other collision systems. This dataset was already analysed in ALICE [107]. The physics message remains unchanged, with current uncertainties — which were not greatly reduced — they are compatible with NLO pQCD predictions and other LHC experiments.

The proposed method has, however some very strong merits, which can be utilized in further studies. First of all, it provides consistent results for a very broad range of purities from 30% to 90%. It gives the flexibility to match working point selection with the requirements of a particular analysis, which may demand higher statistics or higher purity of the obtained b-jet sample. Access to very high purities ($\geq 80\%$) is a qualitative change: from "b-jet-enriched sample" (b-jet purities of 30–50%) to "b-jet sample" (contaminated with minority share from other flavours).

Secondly, the tagger performance was verified with the data-driven method. The templates produced from BDT scores are close to optimal in terms of flavour separation and thus are applicable in the wider range of tagging purity and jet p_{T}.

It is the first application of machine learning in the analysis of HF jets measured by ALICE. The obtained results agree very well with the two other, well-established methods. Given its undeniable advantages, it should be a method of first choice in future HF jet measurements.

Having a pure sample of b-jets, one can proceed to study their structure. This would require an additional preceding step, namely the study of the possible fragmentation biases of the method. This can be done first in MC simulations and then verified in data either with

b-jets tagged with another method *e.g.* with lepton-tagging or with tag-and-probe method *e.g.* with b dijets, where fragmentation of two b-jets is independent.

Jet substructure carries a lot of information about the parton radiation and hadronization. A possible research program covers a large span of insightful measurements: from observables referred to as "jet shapes" (*e.g.* generalized angularities [20, 21]), through whole space of groomed observables (*e.g.* soft-dropped z_g, R_g) to Lund planes [27]. A particularly interesting prospect is the measurement of the dead-cone effect. It can be achieved with the iterative declustering technique [46], which however requires full reconstruction of beauty hadron. The second approach is to utilize recently proposed energy correlators [119].

Chapter 4

Simulations of dead-cone effect with thermal background

4.1 Motivation and aim

As it was described in Sec. 1.4.3, the radiation pattern of quarks in the medium is a rich source of information about the properties of interactions between them. Whether or not it is modified with respect to proton-proton collisions, an important prerequisite for such measurement is the ability to remove the effects related to the presence of uncorrelated, heavy-ion background.

The uncorrelated background can be simulated using a thermal model (see next section for details), which is added to the pp event (simulated *e.g.*, with PYTHIA) at the particle level. This is referred to as an event *embedding*. The exact magnitude and direction of the modifications introduced by the uncorrelated heavy-ion background will also depend on the radiation pattern of the medium-induced radiation. However, one can study the generic features of these modifications, assuming that the probe itself does not differ from the vacuum case (no radiation from interactions of the probe with medium). Following this assumption, we aim at a method which based on the embedded event, restores the values obtained in the vacuum.

4.2 Simulation setup

The simulation setup is described in detail in the next sections. In short, events are generated by PYTHIA with heavy flavour (HF) hadrons made stable particles. They are then embedded into the thermal background and processed using constituent subtractor. Afterward, jets found before and after embedding are reclustered, declustered, matched, groomed, and compared between the two levels.

All the parameters and settings used in this analysis are listed in Table 4.1.

Event construction Events generated by PYTHIA 8 at $\sqrt{s} = 5\,\text{TeV}$ with decays of beauty hadron being blocked (assumption of fully reconstructed beauty hadron, which was proved to be necessary, see Fig. 1.10 and discussion therein). This stage is referred to as PYTHIA- or vacuum-level. Throughout the analysis, only charged particles (except for the HF hadron) are considered for greater similarity to experimental capabilities. Next, such event is embedded into simplified heavy-ion underlying event modelled by a thermal model, creating the "combined-" or "embedded-level". This model produces particles with uniform $\eta - \varphi$ distribution and assigns them p_{T} drawn from gamma distribution $\Gamma(p_{\text{T}}; \alpha, \beta) \sim p_{\text{T}}^{\alpha-1} e^{-p_{\text{T}}/\beta}$ and number of particles comes from the Gaussian distribution. Parameters of thermal background were only roughly tuned to reproduce the variation of the jet p_{T} introduced by the background observed in central 0-10% Pb–Pb events. The thermal model is very simple but

Table 4.1: Values of parameters used in the simulation.

symbol	parameter	value
	PYTHIA	
$\sqrt{s}$	center of mass energy `Beams:eCM`	5 TeV
$\hat{p}_{\mathrm{T}}^{\mathrm{min}}$	`PhaseSpace:pTHatMin`	20 GeV/c
	thermal background	
β	in Γ distribution	0.4 GeV/c
α	in Γ distribution	2
$\langle \mathrm{d}N/\mathrm{d}\eta \rangle$	average number of particles	2000
$\sigma(\mathrm{d}N/\mathrm{d}\eta)$	width of gaussian distribution	400
	constituent subtraction	
ΔR^{max}	max. distance between ghost-particle pairs	0.25
α		0
	jet reconstruction	
R	jet radius	0.4
$p_{\mathrm{T,jet}}^{\mathrm{min}}$	minimum jet p_{T}	10 GeV/c
$\lvert\eta\rvert$	jet pseudorapidity range	< 0.9
	jet finding algorithm	anti-k_{T}
	jet declustering algorithm	Cambridge-Aachen (CA)

can qualitatively capture the basic properties of the background produced in central Pb–Pb collisions. After embedding of PYTHIA event into the heavy-ion background, the constituent subtraction (CS) procedure [120] is performed – the event-wide variant of CS was chosen.

Jet finding and reclustering Having a list of particles for each event before the embedding – at PYTHIA level – and after the embedding (and CS) – the combined level – the jet finder with the same settings is run at both levels. The anti-k_{T} algorithm with $R = 0.4$ was chosen as a baseline algorithm.

Next, each jet is reclustered using the CA algorithm and then declustered – at each step properties of the splitting are recorded. Only the leading branch is followed, resulting in a list of angularly-ordered splittings (corresponding to the primary Lund plane). Utilization of other reclustering algorithms is also possible but leads to a dramatic change in the results as well as their interpretations and is beyond the scope of this analysis [27, 72].

Grooming Results shown later include both groomed and not groomed jets. Discussed here groomers as well as jet grooming in general were introduced in Sec. 1.2.2. Some authors differentiate jet taggers from groomers (as *e.g.* in [72]), here such distinction is not followed and grooming is used as a name of procedure which for each jet selects either one or zero splitting out of its primary Lund plane.

Algorithmically, all considered groomers take as an input an angularly-ordered array of splittings and consist of two steps:

- optional filtering step,
- selection of splitting which maximizes some quantity.

For instance, the Soft Drop (SD) involves its grooming condition ($z > z_{\text{cut}}(\theta/R)^{\beta}$) and then selects the first splitting (almost always the one with the largest θ) out of those which pass this condition. Dynamical Grooming (DyG) skips the filtering step and only selects the splitting having the highest "hardness". Introduced later in this chapter max-$z/\theta_{|\,k_{\mathrm{T}}>0.1}$ first removes splittings with k_{T} below some cut-off value and then returns the one with the highest value of z/θ. No splitting is selected if none of the splittings passes the filtering step.

Following [35], a series of simple groomers with self-explanatory names (which involve no filtering step) like max-z or max-k_{T} are also considered.

Matching procedure Jets at vacuum and embedded levels are matched geometrically – they create a pair if they are each others' closest match and the angular distance between them is smaller than $0.6R$.

Substructure observables related to jet declustering are harder to define because the perturbations introduced by the background can lead to a completely different declustering tree without any one-to-one correspondence between splittings. For instance, in a jet with a symmetric split, close to $z = 0.5$, the leading and subleading prongs can be swapped due to random background fluctuation. As a result, another prong is tracked in the next declustering steps and the whole consecutive splitting tree is redefined. Splittings on the vacuum and combined levels consist of different subsets of jet constituents and cannot be reasonably matched.

Usage of groomers, which yield only one splitting, simplifies this problem because there is only one splitting to compare at the vacuum and embedded level.

One can then check if their subleading prongs consist of the same set of particles. Subleading prongs are compared because the particle from the leading prong can be involved in multiple splittings (at several declustering steps). Operationally the match is defined as correct if $> 50\%$ of the subleading prong at the PYTHIA level is reconstructed inside the subleading prong at combined level [35]. The fraction of jets satisfying this condition is denoted as *subleading prong purity*.

4.3 Subleading prong purity

As it has been clearly shown in Sec. 1.3 due to different fragmentation patterns, many intuitions originating from inclusive jet studies are not applicable to the case of beauty jets. Recall the most important differences are:

- Leading particle effect: beauty hadron carries a large fraction of jet energy so they have less high-z splittings
- Higher number of splittings for light than for heavy quark jets and even higher for gluonic ones

It is therefore instructive to reconsider some of the known jet properties with the differences between jet flavours in mind.

Studies of *subleading prong purity* for various groomers [35] performed on inclusive sample of jets show that:

- subleading prong purity grows with $p_{\mathrm{T}}^{\mathrm{jet}}$,
- better performance is observed for groomers selecting splittings with high longitudinal momentum, such as max-$p_{\mathrm{T}}^{\mathrm{soft}}$, max-$z$, DyG with $a \to 0$ or SD with $\beta = 0$ and high z_{cut}.

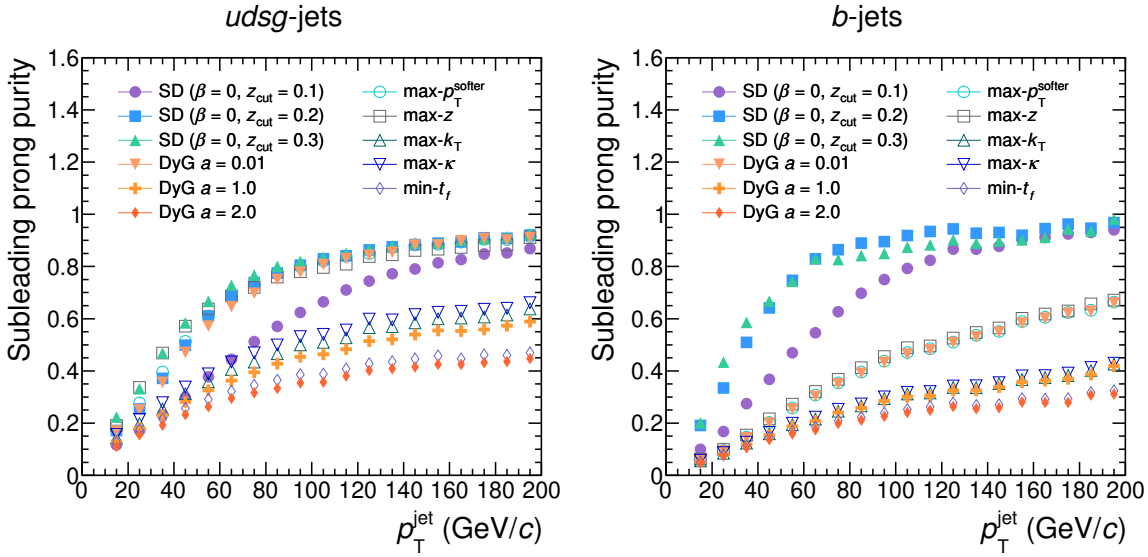

Figure 4.1: Subleading prong purity for selection of groomers for *udsg*– (left) and *b*–jets (right).

The same procedure applied to beauty jets yields different results, as shown in Fig. 4.1. One can distinguish the same "families" of groomers moving together in both cases, like max-k_{T}, max-κ, and DyG $a = 1$. Improvement with $p_{\mathrm{T}}^{\mathrm{jet}}$ is also observed. Nonetheless, most of the analyzed groomers perform notably worse for beauty jets - subleading prong purities are around 1.5–2x lower. The only exception is Soft Drop, to which we will come back later in Sec. 4.7.

4.4 Lund planes for *udsg* and *b*-jets

An attempt to understand this requires a comparison of primary Lund planes for 4 cases: *udsg*– and *b*–jets simulated in a vacuum and embedded into a thermal background.

They will be compared using a symmetrized relative differences:

$$Q(x, y) = \frac{x - y}{x + y} \quad ,$$

where for the one- or two-dimensional histograms the same operation is performed bin-wise.

Fig. 4.2 shows the abovementioned Lund planes and Fig. 4.3 shows symmetrized relative differences Q. Readers can refer to Appendix A for the same plots for different $p_{\mathrm{T}}^{\mathrm{jet}}$ ranges (also for groomers used later). Fig. 4.4 shows projections of these Lund planes on $\ln(1/\theta)$ axis and symmetrized relative differences Q between the projections.

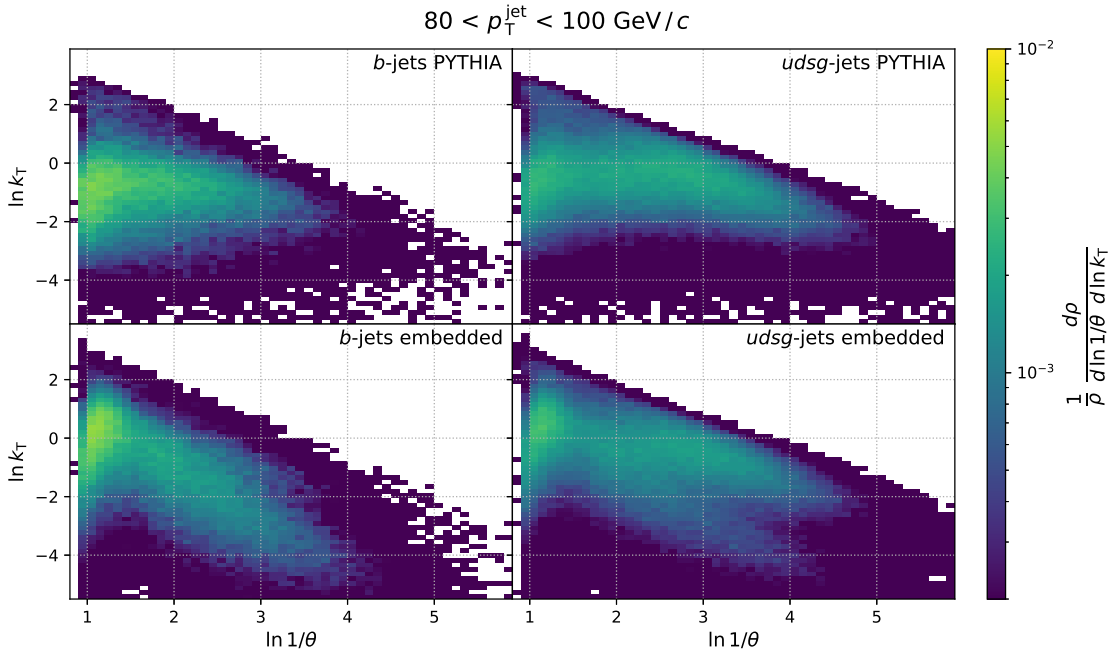

Figure 4.2: Primary Lund planes $\rho(\ln(k_{\mathrm{T}}), \ln(1/\theta))$ for b–jets (left column) and $udsg$–jets (right column), in vacuum (top row) and embedded in the thermal background (bottom row).

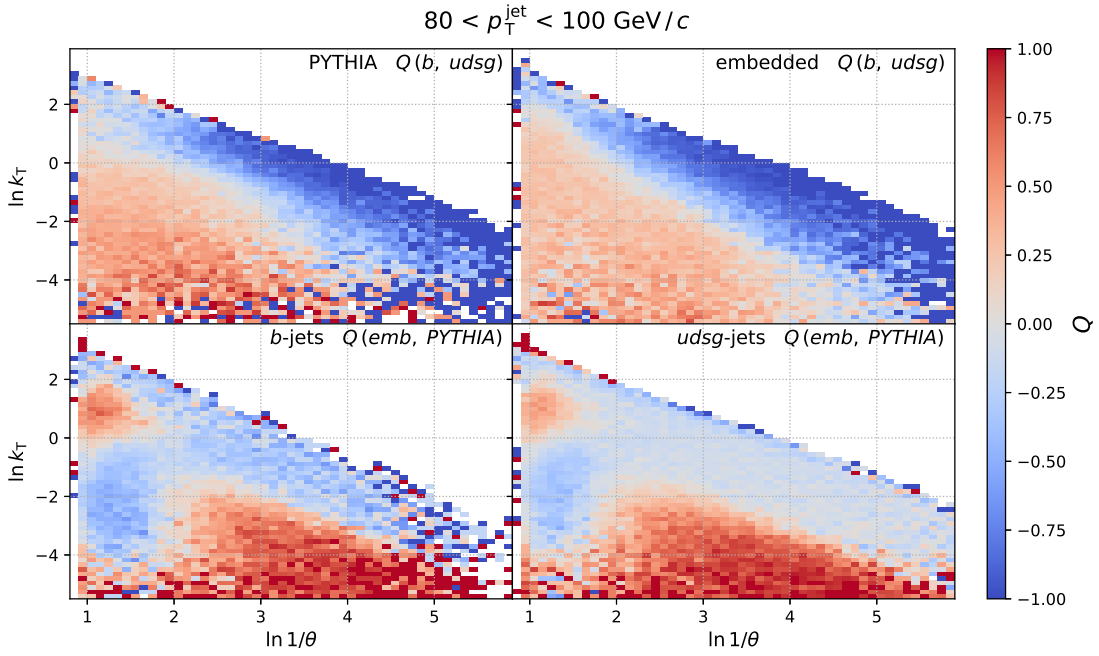

Figure 4.3: Symmetrized relative differences Q between primary Lund planes: $Q(\rho_b^{\mathrm{vac}}, \rho_{udsg}^{\mathrm{vac}})$ (top left), $Q(\rho_b^{\mathrm{emb}}, \rho_{udsg}^{\mathrm{emb}})$ (top right), $Q(\rho_b^{\mathrm{emb}}, \rho_b^{\mathrm{vac}})$ (bottom left) and $Q(\rho_{udsg}^{\mathrm{emb}}, \rho_{udsg}^{\mathrm{vac}})$ (bottom right).

Differences between Lund planes for beauty and light flavour jets in vacuum are clearly apparent. The most striking one is the depletion of large z, small θ splittings for beauty jets (visible as a blue band on the top left plot of Fig. 4.3), which is the manifestation of the dead-cone effect and different fragmentation. A lower number of high-z splittings, which are the most robust against the heavy-ion background for b–jets, is the dominating factor

determining their lower subleading prong purities. The second, less important one is that b-jets in vacuum have a lower average number of splittings per jet, making the impact of the background more pronounced.

The thermal background modifies the Lund planes by introducing more splittings in two separated regions [1] :

- around $(\ln(1/\theta), \ln(k_{\mathrm{T}})) = (1, 1)$
- at small $\theta < 0.14$ ($\ln(1/\theta) > 2$), low k_{T} ($\ln(k_{\mathrm{T}}) < -2$) and low z ($z \lesssim 0.1$)

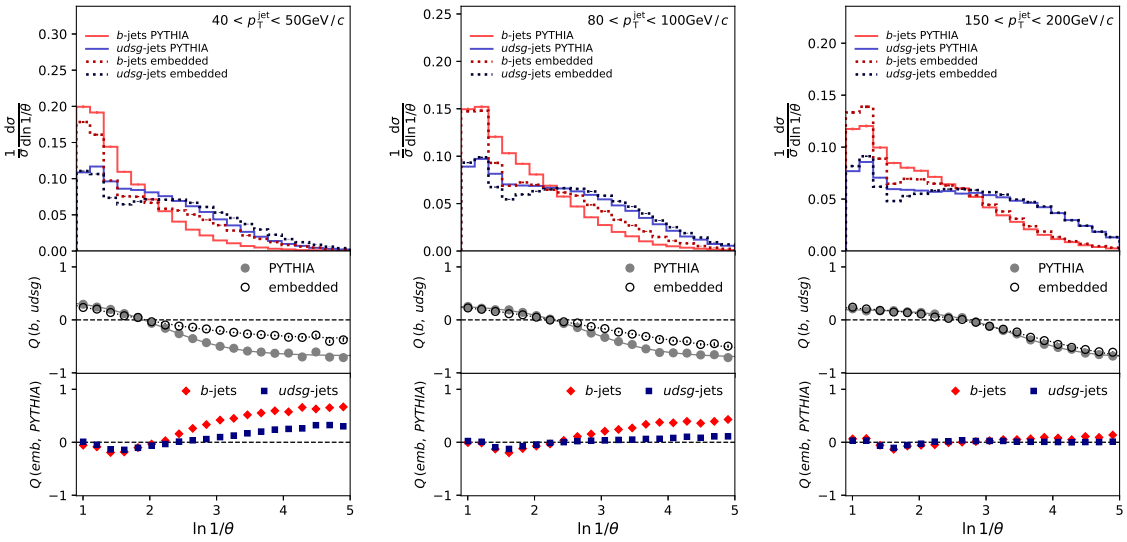

Figure 4.4: Top panels: angular distributions of all splittings belonging to primary Lund plane for three $p_{\mathrm{T}}^{\mathrm{jet}}$ ranges: 40–50 GeV/c, 80–100 GeV/c and 150–200 GeV/c. Middle panels: Q between b–jets and $udsg$–jets (in vacuum and after embedding). Bottom panels: Q between embedded and vacuum cases (for b–jets and $udsg$–jets).

The modifications of the jet Lund plane by the uncorrelated background are nontrivial. They are a convolution of geometrical effects (more background particles appear at a larger distance from jet axis r), properties of the algorithm used for jet reclustering (here: CA), and initial jet fragmentation. We note that a tendency towards more bimodal θ distribution, with a dip around $\theta = 0.2$ or $\ln(1/\theta) = 1.6$, can be explained by the first two factors, as shown in Appendix B.

The impact of background is generally quite strong and projecting on the θ axis may cover it to some extent. It is stronger for jets with lower p_{T} and differs between $udsg$– and b–jets. It leads to modification of the b– to $udsg$–jets ratio as seen in the top row of Fig. 4.3. Reduction of this modification to the minimum is one of the aims of this study.

We note that the dead-cone-like effect is still visible after embedding into the thermal background; however, quantitatively becomes strongly distorted w.r.t. jets in vacuum as it is shown in middle panels of Fig. 4.4 and in more detail in section 4.5.

As the background-related splittings occupy various parts of the Lund planes, they cannot be easily removed using cuts on any of the quantities characterizing splittings θ, k_{T} nor z. Especially cutting away splittings with low k_{T}, which is effective in the reduction of

[1] This is valid in a relative sense: background adds also splittings in between these two regions, but this area is already densely populated in a vacuum case. Please note that the given numbers apply only to the $p_{\mathrm{T}}^{\mathrm{jet}}$ range shown in Fig. 4.2 and 4.3. See Appendix A to compare with others.

hadronization effects [46], is not enough here. We turn back to using groomers in order to minimize the impact of the underlying heavy-ion event and maximize the visibility of the dead-cone effect. As a side effect, we also uncover some interesting insights about jets and the influence of the thermal background on them.

4.5 DyG with $a \to 0$ and transition angles as a function of $p_{\mathrm{T}}^{\mathrm{jet}}$

One of the groomers with the highest subleading prong purity among groomers without a filtering step (like a Soft Drop) is Dynamical Grooming with parameter $a \to 0$. It has good theoretical justification and is proven to be resilient to underlying event (UE) [33] and pileup [121].

Figure 4.5 shows projections of Lund planes obtained for DyG on $\ln(1/\theta)$ axis and symmetrized relative differences between them. These results, in comparison to the inclusive primary Lund planes (where no groomer was applied, shown in Fig. 4.4) show that the dead-cone effect is more prominent (distributions b and $udsg$ are better separated) and the impact of the background is slightly reduced, especially for light flavour jets.

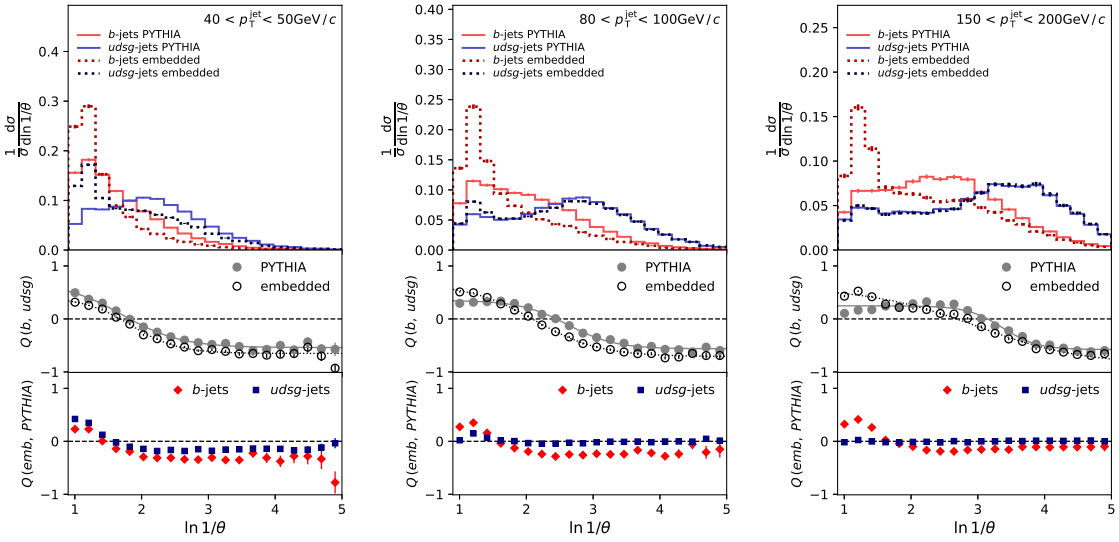

Figure 4.5: Top panels: angular distributions of splittings selected by DyG $a = 0.01$. Middle panels: Q between b–jets and $udsg$–jets (in vacuum and after embedding). Bottom panels: Q between embedded and vacuum cases (for b–jets and $udsg$–jets).

Modification by the thermal background is shown in the bottom panels of Fig. 4.5. In the lowest $p_{\mathrm{T}}^{\mathrm{jet}}$ bin, distributions for b– and $udsg$–jets are strongly altered, both to a similar degree. The impact of the background is greatly reduced at higher jet p_{T} in case of $udsg$–jets but not for b–jets. For all the cases the background acts in a similar way: it increases the average θ (decreases $\ln(1/\theta)$), but rather than shifting the whole distribution, it only enhances counts in the first couple of bins.

Both vacuum and embedded scenarios show strong depletion of low-θ splittings for b-jets (see middle panels). From the figure emerges that the dead-cone effect seems to be equally apparent for jets with and without embedded background. Namely, the amplitude of the effect (measured as a deviation of Q below 0 at small angles) is similar. On the other hand, from the bottom panels in Fig. 4.5, it is evident that the transition angle (defined *e.g.* as the angle at which Q crosses zero) shifts with increasing $p_{\mathrm{T}}^{\mathrm{jet}}$ towards lower values of θ as expected from Eq. 1.6. A more detailed examination reveals that this transition angle Q differs for the

vacuum and the embedded case, and the amplitude of the signal resembling the dead-cone effect for the embedded cases is sometimes larger than in a vacuum.

Extraction of transition angles θ_{tr} The transition angle (defined *e.g.* as the angle at which Q crosses zero) shifts with increasing $p_{\mathrm{T}}^{\mathrm{jet}}$ towards lower values of θ as expected from Eq. 1.6. Looking carefully one can however see that it differs for vacuum and the embedded case. Also, the fact that the amplitude of the effect resembling the dead-cone effect for embedded case is sometimes larger than in a vacuum tells us to remain sceptical. In order to obtain a systematic comparison of embedded and vacuum cases, $Q(\theta)$ is fitted with a sigmoid function:

$$s(\theta) = \frac{(B-A)}{1+e^{-k(\theta-\theta_{tr})}} + A \ . \tag{4.1}$$

A and B correspond to the asymptotic values in $\pm\infty$, k denotes the steepness of the function and θ_{tr} marks the centre of the sigmoid or the angle at which value $\frac{A+B}{2}$ is reached – if $B = -A$ then $s(\theta_{tr}) = 0$. θ_{tr} is then interpreted as the searched transition angle.

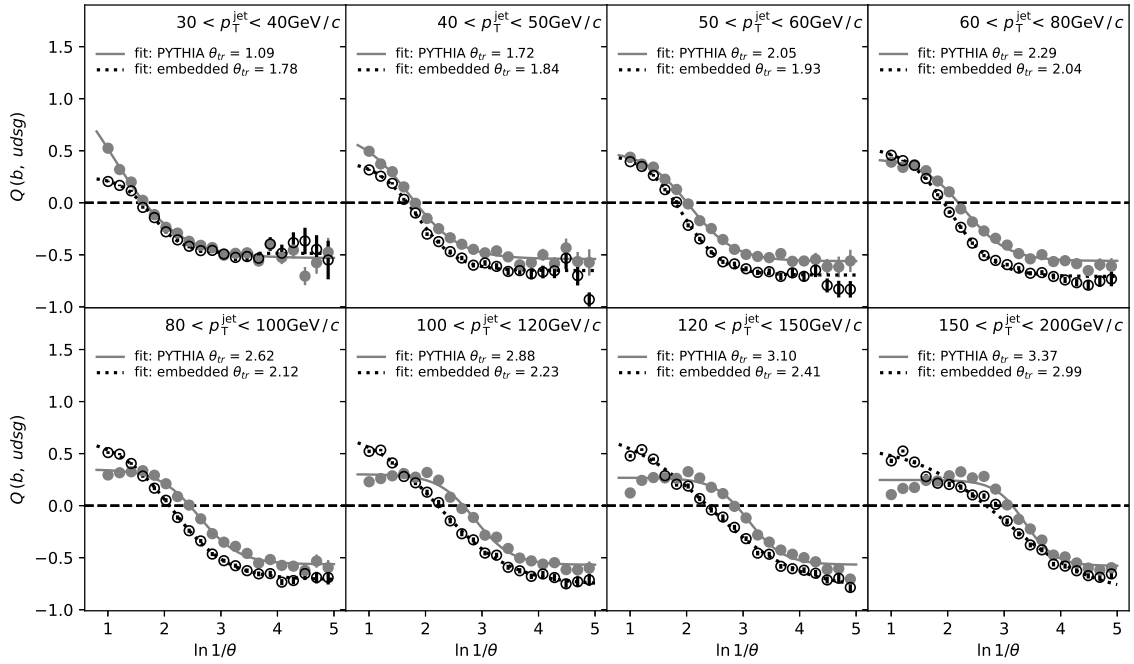

Figure 4.6: Fits of sigmoid function defined by Eq. 4.1 to Q between angular distributions of splittings selected by DyG $a = 0.01$ for b–jets and $udsg$–jets (in a vacuum and after embedding).

Fits of sigmoid function to $Q(\theta)$ in $p_{\mathrm{T}}^{\mathrm{jet}}$ ranging from 30 to 200 GeV/c are shown in Fig. 4.6. Obtained transition angles θ_{tr} are plotted against corresponding $p_{\mathrm{T}}^{\mathrm{jet}}$ in Fig. 4.7 (left) separately for vacuum and embedded cases.

The transition angles in vacuum show a strong dependence on $p_{\mathrm{T}}^{\mathrm{jet}}$– its shape follows quite closely the naïve m_Q/E_{rad} relation, with some offset between them [2]. θ_{tr} obtained for embedded jets do not follow this relation, being almost constant in a wide range of $p_{\mathrm{T}}^{\mathrm{jet}}$. Despite the visible depletion of low-angle emissions for b–jets, embedded jets do not show the expected dead-cone feature which is dependence on radiator energy. The mismatch between simulations with background and in a vacuum is most apparent in the right panel of Fig. 4.7,

[2] see Sec. 4.9 for the discussion on the m_Q/E_{rad} relation and link between $p_{\mathrm{T}}^{\mathrm{jet}}$ and E_{rad}

where the same values are plotted against each other – background subtraction and applied groomer fails to mitigate the impact of uncorrelated thermal background.

It is a straightforward result of thermal background properties observed in Fig. 4.5. It has a larger impact on b–jets and enhances a number of splittings at large angles (at the same θ values independently on $p_{\mathrm{T}}^{\mathrm{jet}}$) so it can emulate the dead-cone effect, but cannot follow typical relation with energy scale.

One important lesson is that looking at the narrow range of $p_{\mathrm{T}}^{\mathrm{jet}}$ or E_{rad}, one can be easily tricked into seeing an effect resembling the dead-cone effect, which is however only an artefact of the different impact of thermal background on heavy– and light–flavour jets.

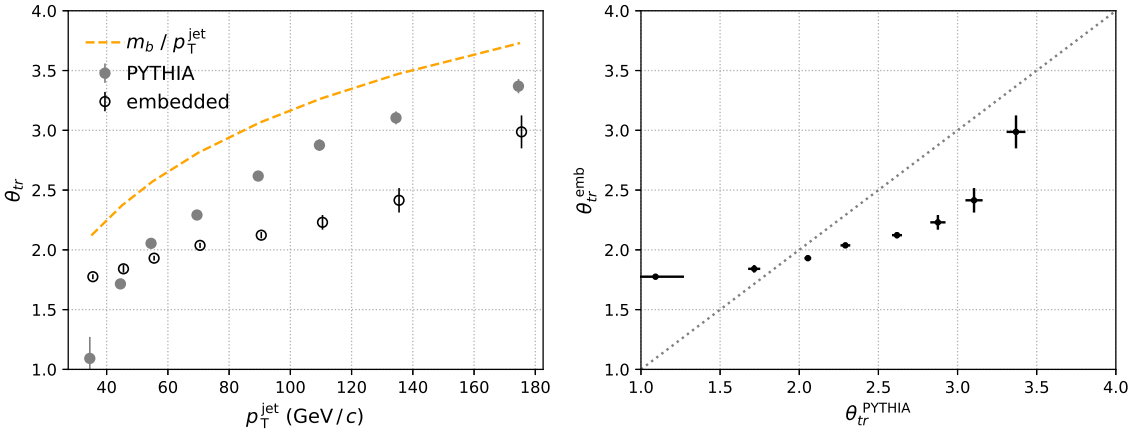

Figure 4.7: Extracted transition angles $\theta_{tr}^{\mathrm{vac}}$ and $\theta_{tr}^{\mathrm{emb}}$ for DyG $a = 0.01$ as a function of $p_{\mathrm{T}}^{\mathrm{jet}}$ (left) and $\theta_{tr}^{\mathrm{emb}}$ as a function of $\theta_{tr}^{\mathrm{vac}}$ (right) for the same $p_{\mathrm{T}}^{\mathrm{jet}}$ bins.

4.6 max-z groomer and implicit dependence on θ in DyG

max-z is another groomer, very similar to DyG with $a \to 0$, but having a bit higher subleading prong purity for light flavour jets at intermediate $p_{\mathrm{T}}^{\mathrm{jet}}$.

It is a simple groomer selecting just the splitting with the highest longitudinal momentum fraction z, while Dynamical Grooming maximizes the following quantity: $\kappa_i(a) = z_i(1-z_i)\, E_{\mathrm{rad},i}\, (\frac{\theta_i}{R})^a$. The first part of the equation denotes the maximization of z, like in max-z, but non-linearly, less strictly close to $z = 0.5$. The last term is responsible for dependence on the splitting angle, however, for sufficiently small a, *e.g.* $a = 0.01$ used here, it is completely negligible, with the difference between $\theta = 0.005$ and $\theta = 0.4$ at the level of a few per cent. It means that the term, which differentiates DyG from max-z is dependent on E_{rad}. E_{rad} is related directly to the ordering of the splitting – it drops as the declustering procedure progresses. For CA it is therefore closely related to the splitting angle θ – large E_{rad} is conjugated with large θ, so besides the last term, DyG has also an additional, implicit preference towards larger angles (even for $a \to a$).

Fig. 4.8 shows the θ distributions for max-z groomer. Compared to DyG $a = 0.01$ the values for light flavour jets are shifted towards lower θ values. Simultaneously the distributions obtained for b–jets show little difference, which together increases the separation between the flavours.

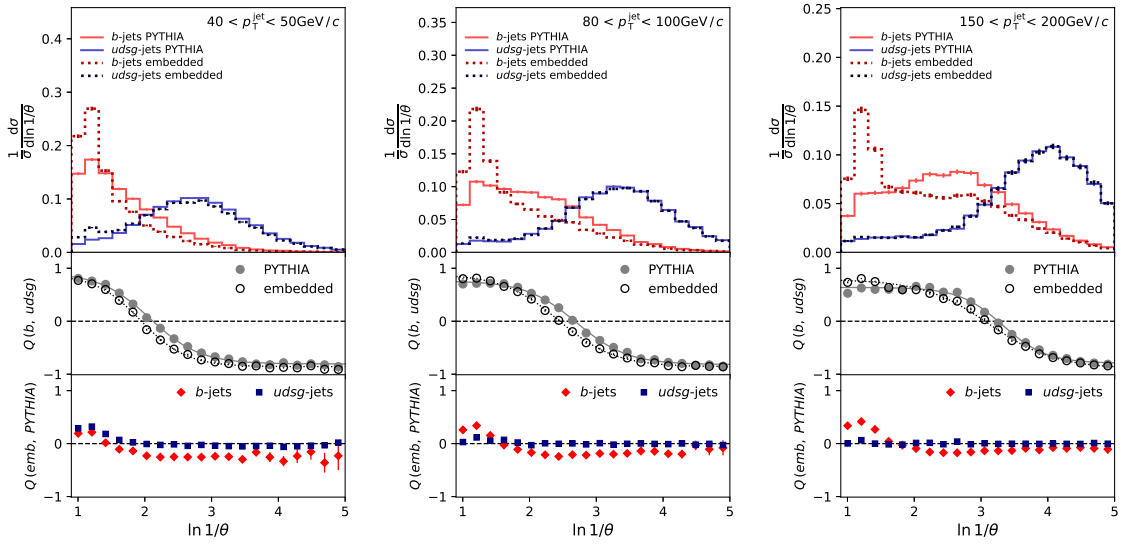

Figure 4.8: Top panels: angular distributions of splittings selected by max-z groomer. Middle panels: Q between b–jets and $udsg$–jets (in vacuum and after embedding). Bottom panels: Q between embedded and vacuum cases (for b–jets and $udsg$–jets).

Comparing the middle panels of Fig. 4.5 and Fig. 4.8, one can see that the transition from enhancement to depletion (in b–jets compared to $udsg$–jets) is sharper in the case of max-z ($Q(\theta)$ is steeper close to the θ_{tr}). The transition angles obtained from the fits to Q, displayed in Fig. 4.9 show much better performance for the embedded jets – they yield results much closer to the vacuum jets compared to DyG.

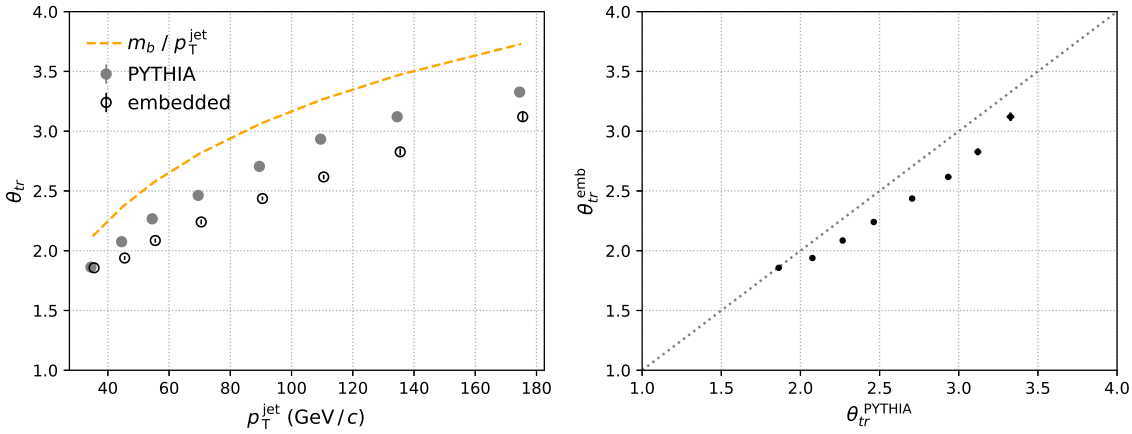

Figure 4.9: Extracted transition angles $\theta_{tr}^{\mathrm{vac}}$ and $\theta_{tr}^{\mathrm{emb}}$ for max-z groomer as a function of $p_{\mathrm{T}}^{\mathrm{jet}}$ (left) and $\theta_{tr}^{\mathrm{emb}}$ as a function of $\theta_{tr}^{\mathrm{vac}}$ (right) for the same $p_{\mathrm{T}}^{\mathrm{jet}}$ bins.

Based on the comparison of max-z groomer and DyG $a = 0.01$ (with its implicit preference towards higher θ) one can say that choosing a groomer which focuses on small angles has several advantages. To begin with, it increases the separation between the two flavours, making it a cleaner observable. Moreover, it shifts the transition angles θ_{tr} towards smaller values, *i.e.* away from the region which is mostly affected by large k_{T} (and thus hard to remove) background. Finally, it is closer to the core idea behind the dead-cone effect: depletion of small-angle radiation. All the jets have some large angle splittings, the difference is in the

small θ part of the distribution. Therefore groomer tuned for sensitivity to the dead-cone effect should be focused there.

4.7 Soft drop and groomer efficiency

Coming back to Fig. 4.1, the groomer which performs notably better for beauty jets than other groomers is Soft Drop. The issue in using them is that subleading prong purity does not tell the full story and can be even ill-defined in an experimental context.

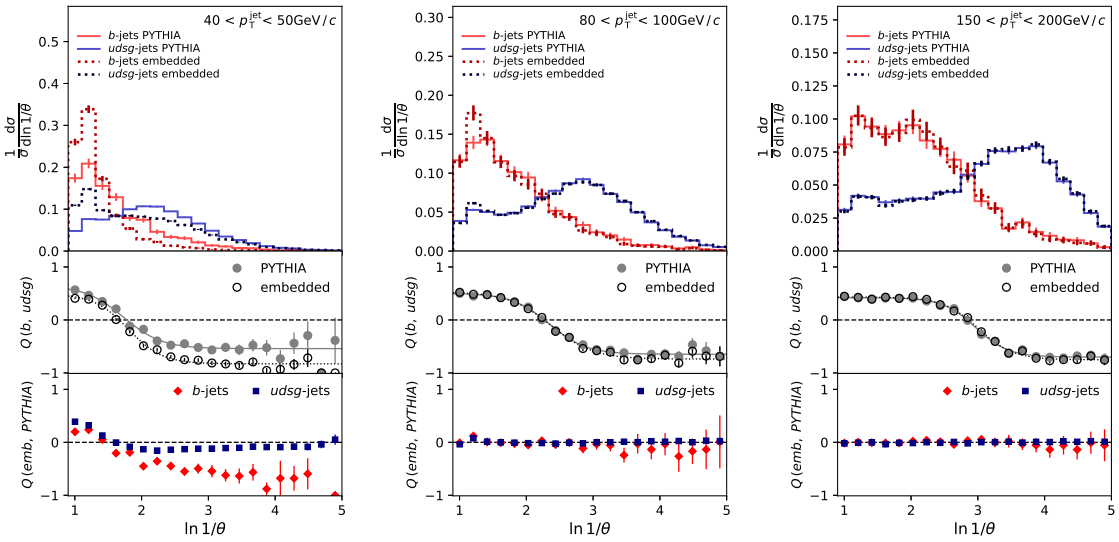

Figure 4.10: Top panels: angular distributions of splittings selected by SD ($\beta = 0, z_{\text{cut}} = 0.2$). Middle panels: Q between b–jets and $udsg$–jets (in vacuum and after embedding). Bottom panels: Q between embedded and vacuum cases (for b–jets and $udsg$–jets).

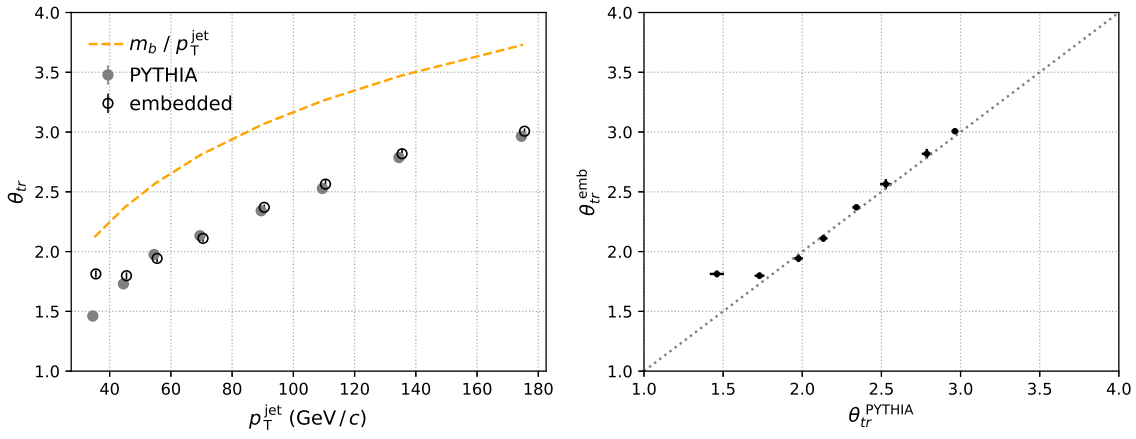

Figure 4.11: Extracted transition angles θ_{tr}^{vac} and θ_{tr}^{emb} for SD ($\beta = 0, z_{\text{cut}} = 0.2$) as a function of $p_{\text{T}}^{\text{jet}}$ (left) and θ_{tr}^{emb} as a function of θ_{tr}^{vac} (right) for the same $p_{\text{T}}^{\text{jet}}$ bins.

The θ distributions and extracted transition angles for Soft Drop with commonly used parameter set: $\beta = 0$ and $z_{\text{cut}} = 0.2$ are displayed in Fig. 4.10 and 4.11. They confirm that Soft Drop shows great resilience to the thermal background above $p_{\text{T}}^{\text{jet}}$ of 80 GeV/c. Except for the first bin ($p_{\text{T}}^{\text{jet}}$ = 30–40 GeV/c), θ_{tr} for vacuum and embedded cases are well aligned.

We note, that performance at the low $p_{\mathrm{T}}^{\mathrm{jet}} \lesssim 50\,\mathrm{GeV}/c$ can be improved by choosing more strict z_{cut} value.

Sample size reduction and selection bias When comparing Figures 4.8 and 4.10, an additional observation is that the error bars, representing statistical uncertainties, are significantly larger when Soft Drop is applied to beauty jets. This reveals the first drawback of Soft Drop, namely the inclusion of a z-cut that is not satisfied by all jets. While the Soft Drop condition is met by a negligibly high fraction (90-95%) of light flavour jets, the same cannot be said for beauty jets, where it amounts to only about 10% for higher jet transverse momenta.

This presents two problems. Firstly, the sample size of beauty jets is reduced by a factor of ten. For heavy-flavour jets, this is a significant disadvantage as the available data sample size is one of the limiting factors in the ongoing analyses. This is particularly true when considering other requirements for the dead-cone analysis (refer to Sec. 4.10), which involve additional steps that further diminish the size of the original b-jet sample. Secondly, it imposes a strong selection bias, which assessment calls for separate studies.

Non-operationality of subleading prong purity in experimental context The situation is even more complicated when moving to low–p_{T} b–jets because the fraction of jets which satisfy the Soft Drop condition is not only low, but also differs significantly between jets in vacuum and those embedded in thermal background. Fractions of jets satisfying grooming condition are further referred to as grooming efficiencies: ϵ_g^{vac}, ϵ_g^{bckg}, $\epsilon_g^{\&}$ correspondingly for jets at vacuum level, embedded level and for pairs of jets which meet grooming condition at both levels.

The intuition behind subleading prong purity is the following. The same grooming procedure is applied on sample of jets, first in vacuum then in background. Subleading prong purity tells what fraction of jets – out of those which pass grooming condition on both levels – the procedure returns the same [3] splitting at both levels.

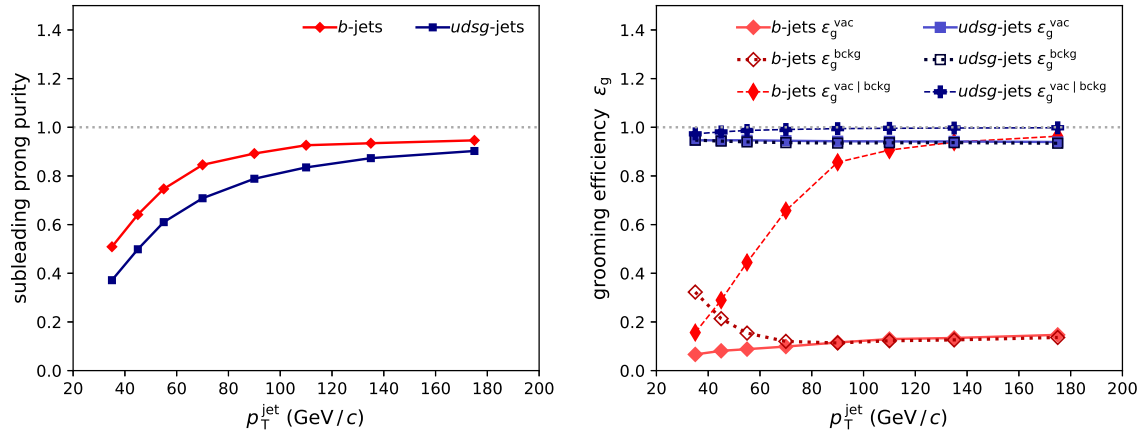

Figure 4.12: Subleading prong purities (left) and grooming efficiencies (right) as a function of $p_{\mathrm{T}}^{\mathrm{jet}}$ for b– and $udsg$–jets obtained for SD ($\beta = 0, z_{\mathrm{cut}} = 0.2$).

As the information on the vacuum scenario is not accessible when measuring heavy-ion collisions, a different question is closer to experimental reality: for what fraction of jets which passed grooming condition in PbPb, the grooming procedure would yield the same splittings if these jets were magically moved to pp.

[3] the same defined as sharing more than 50% of vacuum subleading prong p_{T}

The numerator of both expressions is the same: jets which pass grooming condition on both levels and for which grooming yields the same splitting at both levels. Denominator, however in first case consists of jets which meet grooming condition on both levels, and in the latter – those passing it in PbPb. Subleading prong purity to be experimentally operational should therefore be scaled by $\frac{\epsilon_g^{\&}}{\epsilon_g^{bckg}}$ factor, which could be also called conditional grooming efficiency $\epsilon_{\mathrm{g}}^{\mathrm{vac|bckg}}$ *i.e.* the probability that the jet which passed the grooming condition in the embedded event would pass it also in vacuum. Grooming efficiencies are shown in Fig. 4.12 For light flavour jets or high–p_{T} b-jets this factor is very close to 1, but drops quickly for b–jets with $p_{\mathrm{T}}^{\mathrm{jet}} < 100\,\mathrm{GeV}/c$. For b–jets with p_{T} around $50\,\mathrm{GeV}/c$ it means that subleading prong purity is overestimated by a factor of 3.

The same conclusions are valid for other choices of z_{cut} value with a natural gradation of purity and efficiency with the strictness of the grooming condition.

Overestimation of subleading prong purity for low–p_{T} b–jets is apparent when looking again at the left panel of Fig. 4.10. Their distribution there is strongly distorted by the background, which conflicts with their spurious high subleading prong purity displayed in left panel of Fig. 4.12 (above 60%).

In summary Soft Drop with $\beta = 0$ and $z_{\mathrm{cut}} = 0.2$ at $p_{\mathrm{T}}^{\mathrm{jet}} \gtrsim 80\,\mathrm{GeV}/c$ is highly robust against the impact of uncorrelated thermal background for both *udsg*– and b–jets. For beauty jets it comes at the cost of reduced about 10 times efficiency and related potential selection bias which needs to be studied.

At lower $p_{\mathrm{T}}^{\mathrm{jet}}$ the subleading prong purities for b–jets are greatly reduced by the mismatch between grooming efficiencies at vacuum and embedded levels. Despite it, the extracted transition angles coincide before and after embedding. While specific jet splittings are not fully traceable in this regime, in principle the dead-cone could be still preserved in different subset of jet splittings. Telling if this is the case requires further studies.

4.7.1 Variations of Soft Drop

Alternative choices of β in Soft Drop are also worth considering. For $\beta > 0$ grooming is more strict at large angles, which seems to be helpful in dealing with splittings located at large θ and large k_{T} region (also large z), which are typically harder to remove without affecting interesting part of the Lund plane. The issue common for the entire Soft Drop family is its separating power, resulting from large groomer efficiency difference between jet flavours. Light flavour jets tend to preserve very high grooming efficiency even for very strict choice of parameters. For instance for Soft Drop with $\beta = 0$ and $z_{\mathrm{cut}} = 0.3$, a fraction of jets passing the corresponding grooming condition is above 80% for light flavour jets and only 3–6% for b–jets (depending on $p_{\mathrm{T}}^{\mathrm{jet}}$). It is obvious that for such numbers, a typical b–jet which managed to survive the grooming, will have exactly one splitting which satisfies related condition, while jet originating from light flavour quark or gluon can have a few of them. Out of these splittings, only the first one (one with the largest θ) will be used by the Soft Drop in the tagging mode. Large fraction of small–θ splittings which satisfy the grooming condition for *udsg*–jets are rejected and dead-cone effect is less pronounced.

A simple solution to this problem would be reversing the Soft Drop and among a set of splittings passing the grooming condition selecting the last splitting (with the smallest θ). As such approach seems to be contradictory to the main Soft Drop intention or feature, we avoid calling it Soft Drop. At the same time we do not drop this idea completely.

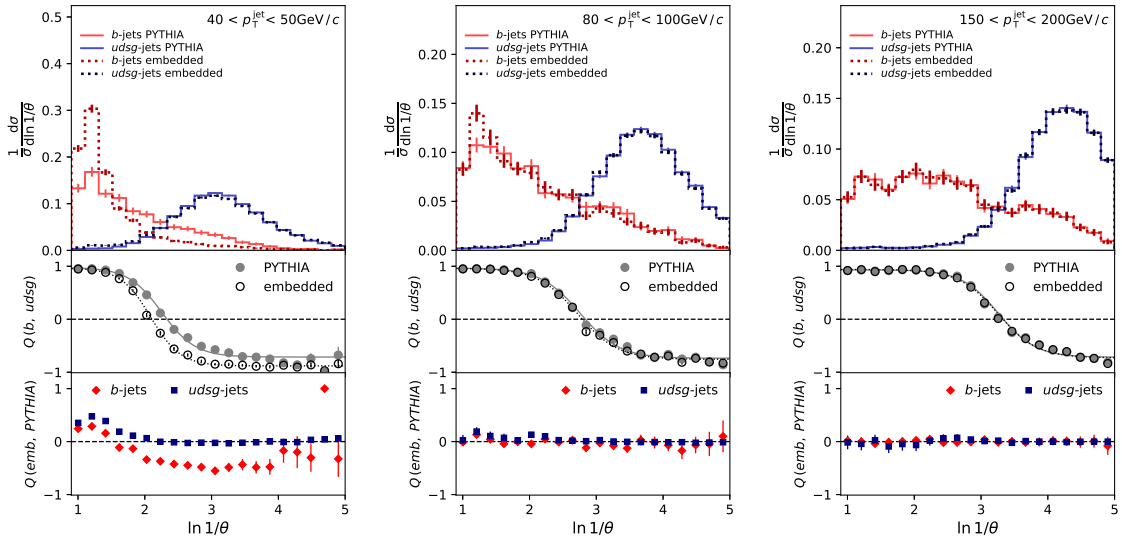

Figure 4.13: Top panels: angular distributions of the last splittings (instead of first as in Soft Drop) satisfying grooming condition of SD ($\beta = 0, z_{\text{cut}} = 0.2$). Middle panels: Q between b–jets and $udsg$–jets (in vacuum and after embedding). Bottom panels: Q between embedded and vacuum cases (for b–jets and $udsg$–jets).

The θ distribution obtained with this approach are shown in Fig. 4.13. As expected, the distributions for $udsg$–jets were strongly shifted towards lower angles and for b–jets they are very similar as in regular Soft Drop (compare Fig. 4.10) because usually there is only one splitting passing the grooming condition so the two approaches are equivalent for them. Grooming efficiencies are by definition not affected and subleading prong purities increased by 5-10% for $udsg$–jets with $p_{\text{T}}^{\text{jet}} < 100\,\text{GeV}/c$.

4.8 Groomer maximising z/θ

Selection of the last instead of the first splitting passing some condition has more benefits. It appears that one can drastically loosen the grooming condition without large impact on resilience to background at the distribution level and limited influence on subleading prong purity (scaled by $\epsilon_{\text{g}}^{\text{vac|bckg}}$). It removes important drawbacks of Soft Drop with strict cut on z related to grooming efficiency described in Sec. 4.7.

Choosing the last available splitting often coincides with selecting the one with the largest z. Both approaches have some advantages. Simultaneously the differences between them are too small and not insightful enough to deserve separate consideration. An intermediate approach is therefore proposed, maximising z/θ. Such groomer yields exactly the same splitting as groomer taking the last available splitting for around 75–85% of jets depending on flavour, simulated collision system and p_{T}. With max-z groomer, it agrees in 65–75% of cases. For comparison, the agreement between it and max-k_{T} groomer is at the level of 30-70% for beauty and only 3-10% for light flavour jets.

The entire analysis focuses on particle level simulation, without studying correspondence to parton level, which is beyond its scope. However based on other studies one can assume that rejecting the low-k_{T} part of the Lund plane would be helpful in removing hadronization effects. As the selected splittings mostly populate high-z region, the amplitude of these effects can be expected to be moderate [72] so rather loose cut of $k_{\text{T}} > 0.1\,\text{GeV}/c$ is chosen. Such a cut removes also part of the introduced by the background splittings at low–θ. Following the explicit convention, this groomer is labelled as max-$z/\theta_{|\,k_{\text{T}}>0.1}$ for the rest of this chapter.

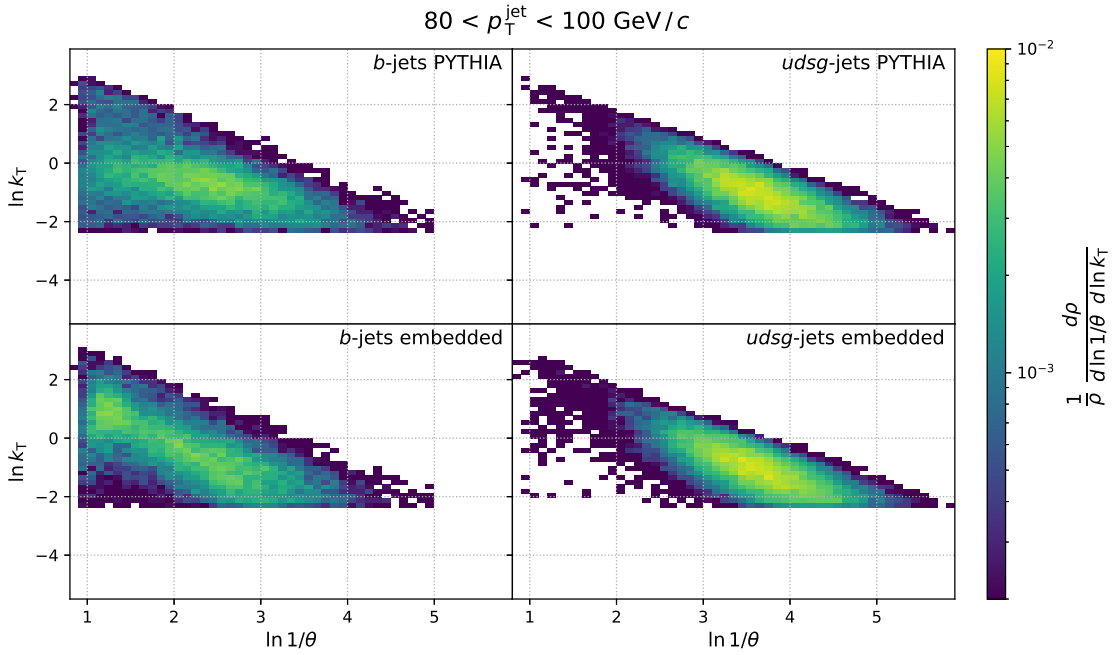

Figure 4.14: Primary Lund planes $\rho(\ln(k_T), \ln(1/\theta))$ for b–jets (left column) and $udsg$–jets (right column), in vacuum (top row) and embedded in the thermal background (bottom row) after applying max-$z/\theta_{|\,k_T>0.1}$ groomer.

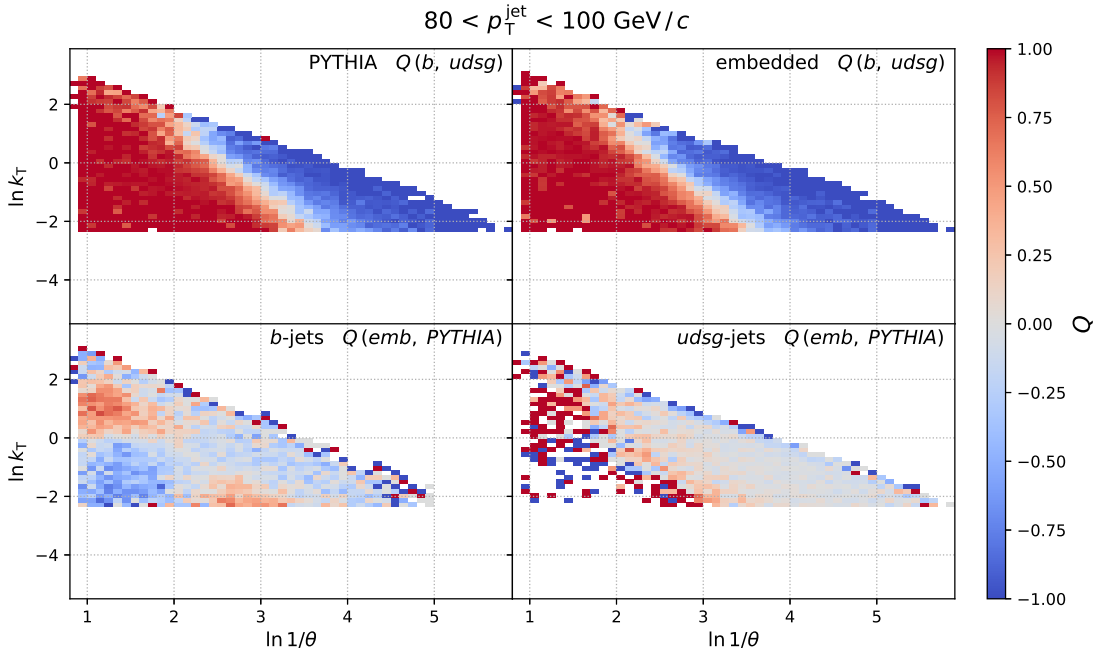

Figure 4.15: Symmetrized relative differences Q between primary Lund planes after applying max-$z/\theta_{|\,k_T>0.1}$ groomer: $Q(\rho_b^{vac}, \rho_{udsg}^{vac})$ (top left), $Q(\rho_b^{emb}, \rho_{udsg}^{emb})$ (top right), $Q(\rho_b^{emb}, \rho_b^{vac})$ (bottom left) and $Q(\rho_{udsg}^{emb}, \rho_{udsg}^{vac})$ (bottom right).

4.8.1 Performance of max-$z/\theta_{|\,k_T>0.1}$

Fig. 4.14 shows Lund planes obtained with max-$z/\theta_{|\,k_T>0.1}$ for beauty and light flavour jets in vacuum and embedded into thermal background and Fig. 4.15 shows symmetrized relative

differences between particular pairs of Lund planes. For the $p_{\mathrm{T}}^{\mathrm{jet}}$ displayed there, the impact of background on light flavour jets is almost completely removed by the groomer. For the beauty jets, it is still present at large θ and partially at very low k_{T} near the cutoff value. It points to some sensitivity on the exact value of this cutoff. At the same time, after integration over the k_{T} axis, the θ distribution is very similar to vacuum case as shown in Fig. 4.16. Similarly to other groomers light flavour jets are more resilient to thermal background. However for max-$z/\theta_{|\,k_{\mathrm{T}}>0.1}$ also b–jets show only small susceptibility to its impact. In higher $p_{\mathrm{T}}^{\mathrm{jet}}$ bins there is a rather small additional bump at high θ, which does not affects the interesting low θ region. In the low $p_{\mathrm{T}}^{\mathrm{jet}}$ bin, θ distribution of embedded b–jets is very close to the vacuum ones, notably much closer even than in case of a very strict (passed by less than 10% of jets) SD ($\beta = 0$, $z_{\mathrm{cut}} = 0.2$).

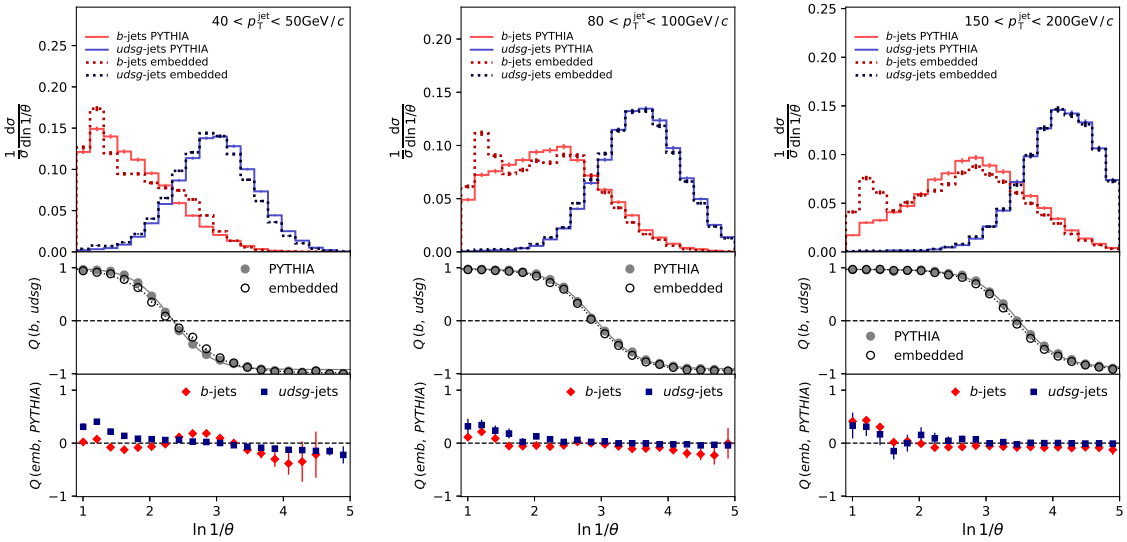

Figure 4.16: Top panels: angular distributions of splittings selected by max-$z/\theta_{|\,k_{\mathrm{T}}>0.1}$ groomer. Middle panels: Q between b–jets and *udsg*–jets (in vacuum and after embedding). Bottom panels: Q between embedded and vacuum cases (for b–jets and *udsg*–jets).

max-$z/\theta_{|\,k_{\mathrm{T}}>0.1}$ provides excellent separation between flavours, better than other considered groomers, namely DyG $a = 0.01$ (Fig. 4.5), max-z (Fig. 4.8), SD ($\beta = 0$, $z_{\mathrm{cut}} = 0.2$) (Fig. 4.10) and maybe even "reversed Soft Drop" (Fig. 4.13). It is convenient to compare middle panels of the plots: for max-$z/\theta_{|\,k_{\mathrm{T}}>0.1}$ the symmetrized relative difference Q is very close to ± 1 for large part of the θ range. It tells that the visibility of the dead-cone effect is better than for any other groomer.

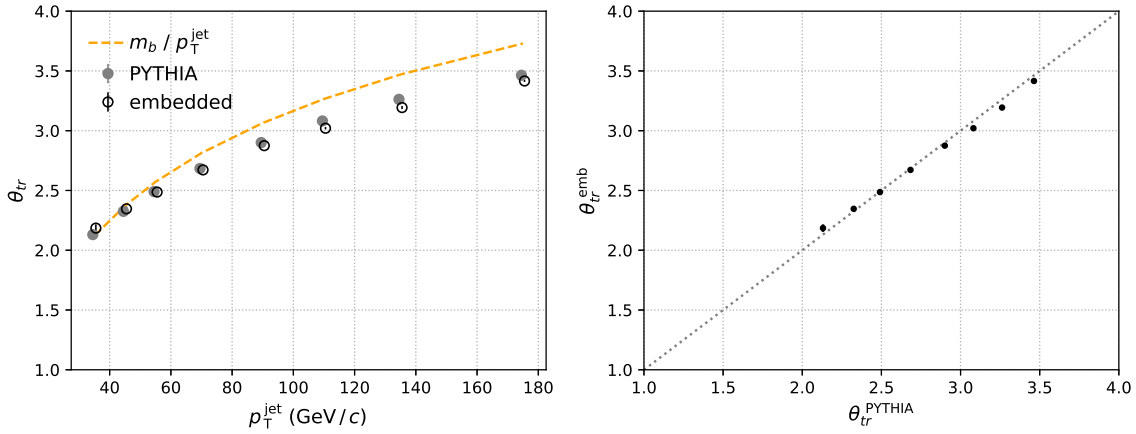

Figure 4.17: Extracted transition angles θ_{tr}^{vac} and θ_{tr}^{emb} for max-$z/\theta_{\,|\,k_{\text{T}}>0.1}$ groomer as a function of $p_{\text{T}}^{\text{jet}}$ (left) and θ_{tr}^{emb} as a function of θ_{tr}^{vac} (right) for the same $p_{\text{T}}^{\text{jet}}$ bins.

Fig. 4.16 and 4.17 show that observed residual modifications of θ distributions introduced by the background have almost no impact on the θ_{tr}. They follow closely the naïve m_Q/E_{rad} relation. A natural consequence of choosing the smallest rather than the largest angle (as in SD) is that the found θ_{tr} are smaller. While it seems to be beneficial for the separation between flavours and resilience to the background, it challenges to a larger degree the precision of the experimental apparatus. At highest $p_{\text{T}}^{\text{jet}} = 150$ *to* $200\,\text{GeV}/c$ the transition angle is close to $\theta = 0.03$ and to observe it one clearly needs to measure splittings at even smaller angles. It is not impossible as shown in published by ATLAS measurements which goes down to $\theta = 0.005$ [28] and preliminary studies by ALICE [122] (down to $\theta = 0.007$)

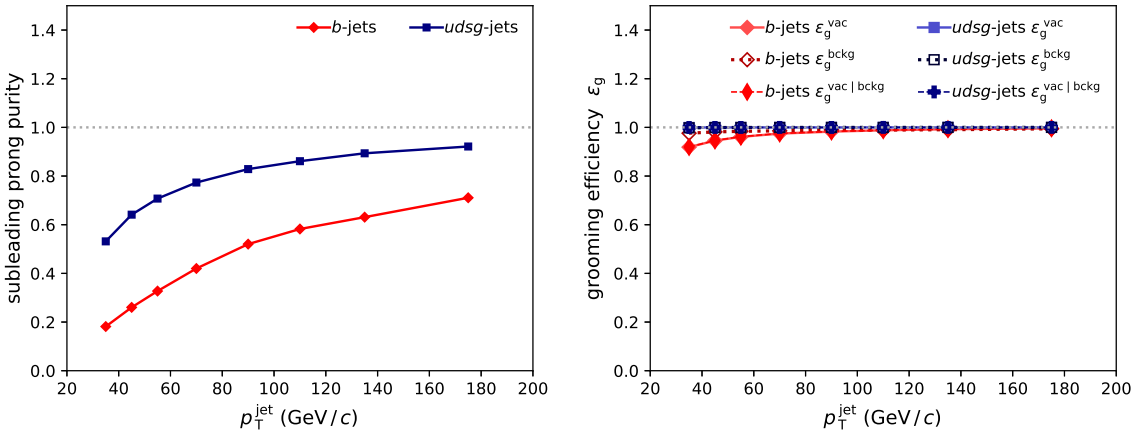

Figure 4.18: Subleading prong purities (left) and grooming efficiencies (right) as a function of $p_{\text{T}}^{\text{jet}}$ for b– and $udsg$–jets obtained for max-$z/\theta_{\,|\,k_{\text{T}}>0.1}$ groomer.

Fig. 4.18 shows subleading prong purity and grooming efficiencies of max-$z/\theta_{\,|\,k_{\text{T}}>0.1}$. All efficiencies are much above 90%. The subleading prong purity for $udsg$–jets grows with $p_{\text{T}}^{\text{jet}}$ from 50 to 90%, while for b–jets it is much lower and increases from 20 to 70% with 50% reached around $p_{\text{T}}^{\text{jet}} = 100\,\text{GeV}/c$. The values obtained for b–jets are not fully satisfactory, because they indicate problems in unfolding due to off-diagonal terms in the response matrix. They are significantly lower than it is doable with SD. They are however better by at least 10% than any groomer preserving full grooming efficiency shown in Fig. 4.1.

The main achievement of proposed groomer w.r.t groomers considered at the beginning of the chapter is a combination of perfect grooming efficiency and separation power with descent resilience to the thermal background (very good at sample level, worse at single-jet level).

4.9 θ_{tr} as a function of E_{rad} and $p_{\mathrm{T}}^{\mathrm{jet}}$

Everywhere in this chapter transition angles θ_{tr} were plotted as a function of $p_{\mathrm{T}}^{\mathrm{jet}}$ along with naïve m_Q/E_{rad} relation. One should not expect that these two will coincide, even in an idealized case. The expected level of disagreement is also not known without dedicated studies. First of all, $p_{\mathrm{T}}^{\mathrm{jet}}$ and E_{rad} are in general not the same – they are equal only in the case of the first splitting and besides it E_{rad} is always smaller than $p_{\mathrm{T}}^{\mathrm{jet}}$. Secondly, $\theta_{tr}(E_{\mathrm{rad}})$ also would not correspond to m_Q/E_{rad} – they are only the result of some arbitrary parametrization of specifically normalized θ distributions and simple relation m_Q/E_{rad} will not replace proper QCD calculations. One should keep in mind these two limitations.

The natural idea would be to use E_{rad} instead of $p_{\mathrm{T}}^{\mathrm{jet}}$ to come closer to the true dead-cone effect, however, it is also not a perfect solution, especially from the experimental point of view. First of all, radiator energy is under poorer experimental control than $p_{\mathrm{T}}^{\mathrm{jet}}$ because it accumulates the distortions introduced by the background in both total jet p_{T} and in angular ordering. Especially the second is hard to account for. Secondly, jets at very various $p_{\mathrm{T}}^{\mathrm{jet}}$ behave differently in the background – one should in general avoid mixing jets at very different $p_{\mathrm{T}}^{\mathrm{jet}}$ scales. Additionally, they often require different experimental treatment, *e.g.* triggering.

Generally, as the leading branch of heavy flavour jet tends to carry a large fraction of its momentum, its selected splitting will usually have higher corresponding E_{rad} than light flavour jets at the same $p_{\mathrm{T}}^{\mathrm{jet}}$. The scale of this difference will depend largely on the properties of a particular groomer. Fig. 4.19 shows distributions of E_{rad} for SD ($\beta = 0, z_{\mathrm{cut}} = 0.2$) and max-$z/\theta_{|\,k_{\mathrm{T}}>0.1}$. For b–jets in both cases they are very close to $p_{\mathrm{T}}^{\mathrm{jet}}$. Light flavour jets for SD are only slightly lower as these are the first splittings which satisfy the grooming condition, so p_{T} of almost all jet constituents is summed up to compute the E_{rad}. For max-$z/\theta_{|\,k_{\mathrm{T}}>0.1}$ these are often splittings close to the end of the splitting tree and on average E_{rad} corresponds to about half of the $p_{\mathrm{T}}^{\mathrm{jet}}$.

What would be the outcome of comparing splittings with the same E_{rad} instead of the same $p_{\mathrm{T}}^{\mathrm{jet}}$? From θ distributions for any groomer, one can see that as the jet energy scale increases, the θ of the selected splitting shifts towards lower values. Equalization of E_{rad} between *udsg*–jets and b–jets would increase the separation between flavours. For the same $p_{\mathrm{T}}^{\mathrm{jet}}$ of b–jets the transition angles would shift towards lower values (higher $\ln(1/\theta)$).

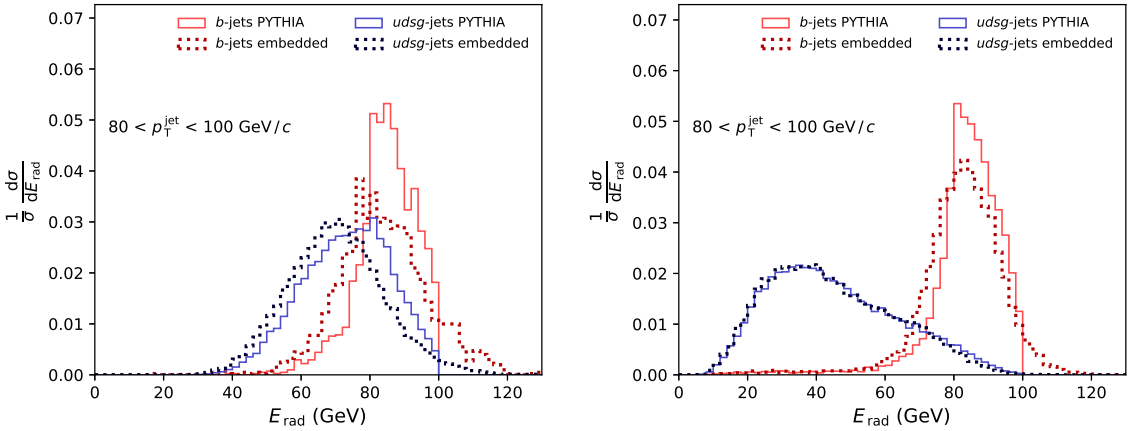

Figure 4.19: Distributions of E_{rad} at the splitting selected by SD ($\beta = 0, z_{\mathrm{cut}} = 0.2$) (left) and max-$z/\theta_{|k_{\mathrm{T}}>0.1}$ (right) for jets with $p_{\mathrm{T}}^{\mathrm{jet}} = 80$–$100\,\mathrm{GeV}/c$. E_{rad} in the embedded case can exceed $p_{\mathrm{T}}^{\mathrm{jet}}$ because jets were selected based on their p_{T} at vacuum level.

Another property of the groomed θ and hence extracted transition angles is the sensitivity to the chosen value of the k_{T} cut. A more strict cut rejects the splittings at the smallest angles (as can be seen on any Lund plane) and shifts θ_{tr} towards higher values of θ. The values of k_{T} cut are rather arbitrary and serve practical reasons – possible exact calibration of the transition angles to m_Q/E_{rad} curve would likely be accidental and should not be the target.

For the reasons listed above, the transition angles θ_{tr} are not expected to follow exactly m_Q/E_{rad} and their analyses as a function of E_{rad} instead of $p_{\mathrm{T}}^{\mathrm{jet}}$ are not pursued. However, the idea that the sought procedure should yield the same results after the addition of uncorrelated background is a requirement which is sensible and fully operational in the simulation studies. It proves the robustness against the selected model of background which is the prime goal of this study. Comparing values obtained with and without background with each other (as it was done in the right-hand side of Fig. 4.7, 4.9, 4.11, 4.17) is the least questionable approach.

4.10 Conclusions

Uncorrelated background modifies the substructure of the jets, particularly, additional background particles can populate low-θ region of the Lund plane and shadow the dead-cone effect. To mitigate its impact some kind of grooming technique, to remove the multitude of soft background particles is needed.

Impact of thermal background on b–jets is stronger than in the case of light flavour jets, because their splittings are characterized by much smaller values of z (and there are fewer of them). This feature of beauty jets makes the application of Soft Drop problematic – contrary to inclusive jets, grooming efficiency for b–jets cannot be neglected.

Finally, convolution of presence of background with arbitrary grooming technique can lead to spurious enhancement of dead-cone – it is important to study the effect as a function of the energy scale, while $p_{\mathrm{T}}^{\mathrm{jet}}$ may be preferred over E_{rad} for operative reasons.

Final recommendations In order to measure dead-cone effect in heavy-ion collisions one needs to measure b–jets with fully reconstructed beauty hadron. The next step should be reclustering and declustering of the jets and selection of specific splitting using groomer. We propose max-$z/\theta_{|k_{\mathrm{T}}>0.1}$ groomer, which proved to be effective in the restoration of θ distribution shape for both b– and $udsg$–jets down to low p_{T}. It achieves that with almost

100% grooming efficiency utilizing full b–jet sample and being therefore free from potential jet selection bias and issues with non-operationality. max-$z/\theta_{|k_{\mathrm{T}}>0.1}$ gives very good results on the sample level – it does not select exactly the same splitting before and after the embedding. It is reflected by the purities which are reached by this groomer – around 60% at $p_{\mathrm{T}}^{\mathrm{jet}} = 100\,\mathrm{GeV}/c$. Such values could complicate or even rule out completely the application of unfolding. Fortunately, the residual differences between vacuum and embedded jets after performing constituent subtraction and grooming are so small that unfolding may be unnecessary taking into account other sources of uncertainties.

That being said, the Soft Drop may still be a valid choice, especially as a complementary method. Thanks to its higher purity, SD could for instance validate the impact of the unfolding on the final result. Unfortunately, high purity is not the only prerequisite for the successful construction of the response matrix. Low values of $\epsilon_{\mathrm{g}}^{\mathrm{vac|bckg}}$ can make it infeasible just like degraded purity, so in case of SD with $\beta = 0$ and $z_{\mathrm{cut}} = 0.2$, unfolding could be performed for jets with $p_{\mathrm{T}}^{\mathrm{jet}} \gtrsim 80$–$100\,\mathrm{GeV}/c$.

Outlook The studied here settings correspond to central 0–10% PbPb collision and jets with radius $R = 0.4$. Removal of background effects would be of course easier in semicentral collisions, while the same effects, simply weaker, should play roles. Switching to more peripheral collisions would enable to go down with $p_{\mathrm{T}}^{\mathrm{jet}}$ or increase subleading prong purity. Alternatively one could decrease jet radius to $R = 0.2$ to reduce the catchment area of the jets. This brings however some drawback as lowering energies of the jets enhances m_b to energy ratio and thus expected dead-cone angle, which already at $p_{\mathrm{T}}^{\mathrm{jet}} = 40\,\mathrm{GeV}/c$ equals to 0.1 so would be comparable to R. At higher energies, however, this would clearly increase subleading prong purities.

Studies described in this chapter could be further extended. Transition angles θ_{tr} extracted from embedded PYTHIA jets may follow exactly their values from the vacuum. However, it is not clear how sensitive to modifications induced by various medium models this method would be. It definitely calls for further studies.

Based on studies discussed in this chapter another groomer with better theoretical support could be proposed. Ideally, it could benefit from preserving the main features of max-$z/\theta_{|k_{\mathrm{T}}>0.1}$: selecting splittings close to the end of the splitting tree, preferably with high z while omitting strict cuts (*e.g.* on z or k_{T}) which helped to achieve good separation power, resilience to uncorrelated background and high grooming efficiency.

It would be interesting to investigate the origin of so large observed grooming efficiencies between vacuum and embedded cases – what are the splittings passing grooming condition in embedded jets which did not pass it in the vacuum?

For completeness, this study should be supplemented by simulation on parton level and estimation of expected experimental precision achievable at LHC experiment in Run 3 and Run 4.

Appendices

Appendix A

Lund planes

This appendix contains Lund planes obtained for groomers described in Sec. 4. For each groomer and $p_{\mathrm{T}}^{\mathrm{jet}}$ range the same two panels of plots are shown, therefore their captions as skipped.

Left panels show: primary Lund planes $\rho(\ln(k_{\mathrm{T}}), \ln(1/\theta))$ for b–jets (left column) and *udsg*–jets (right column), in vacuum (top row) and embedded in thermal background (bottom row).

Right panels show: symmetrized relative differences Q between primary Lund planes: $Q(\rho_b^{\mathrm{vac}}, \rho_{udsg}^{\mathrm{vac}})$ (top left), $Q(\rho_b^{\mathrm{emb}}, \rho_{udsg}^{\mathrm{emb}})$ (top right), $Q(\rho_b^{\mathrm{emb}}, \rho_b^{\mathrm{vac}})$ (bottom left) and $Q(\rho_{udsg}^{\mathrm{emb}}, \rho_{udsg}^{\mathrm{vac}})$ (bottom right)

A.1 all splittings (no groomer applied)

A.1.1 $40 < p_{\mathrm{T}}^{\mathrm{jet}} < 50\,\mathrm{GeV}/c$

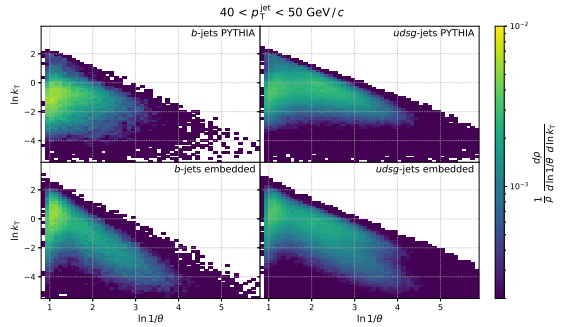

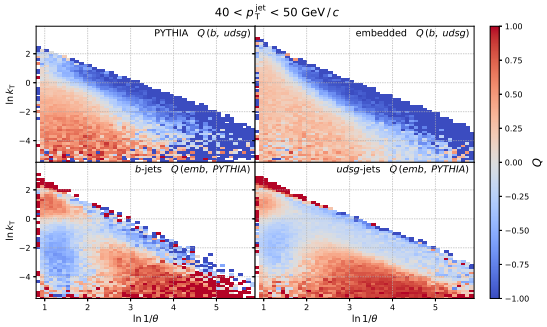

A.1.2 $80 < p_{\mathrm{T}}^{\mathrm{jet}} < 100\,\mathrm{GeV}/c$

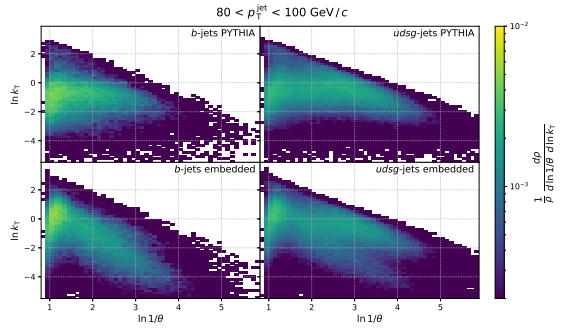

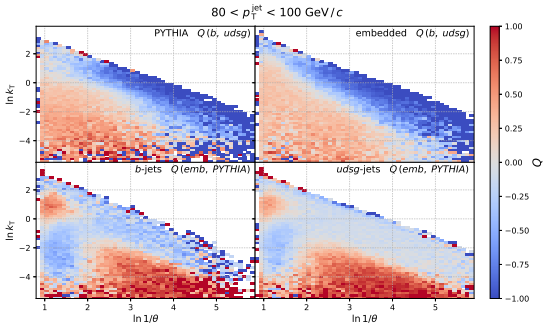

A.1.3 $150 < p_{\mathrm{T}}^{\mathrm{jet}} < 200\,\mathrm{GeV}/c$

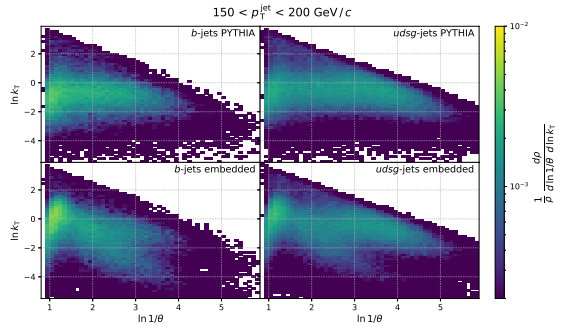

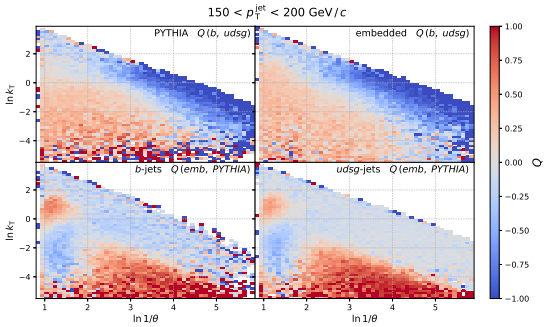

A.2 Groomed with DyG $a = 0.01$

A.2.1 $40 < p_{\mathrm{T}}^{\mathrm{jet}} < 50\,\mathrm{GeV}/c$

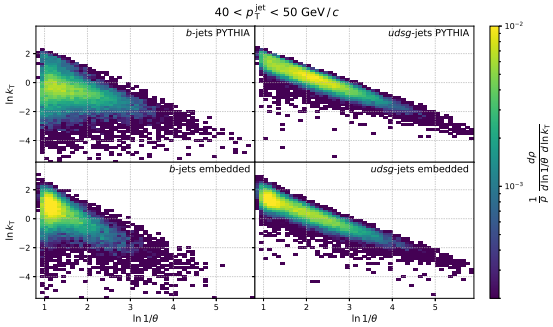

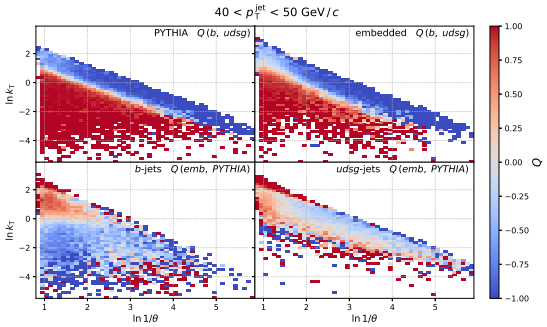

A.2.2 $80 < p_{\mathrm{T}}^{\mathrm{jet}} < 100\,\mathrm{GeV}/c$

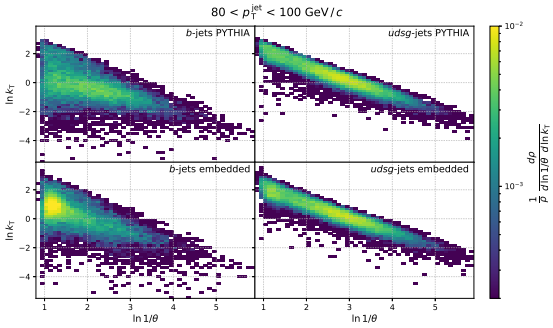

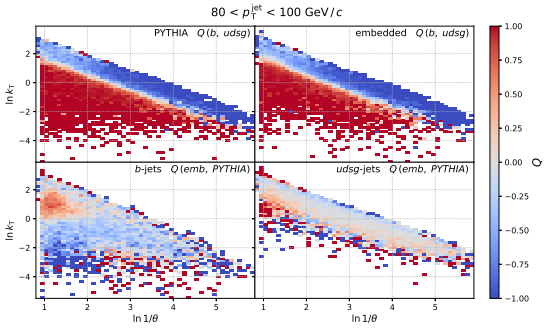

A.2.3 $150 < p_{\mathrm{T}}^{\mathrm{jet}} < 200\,\mathrm{GeV}/c$

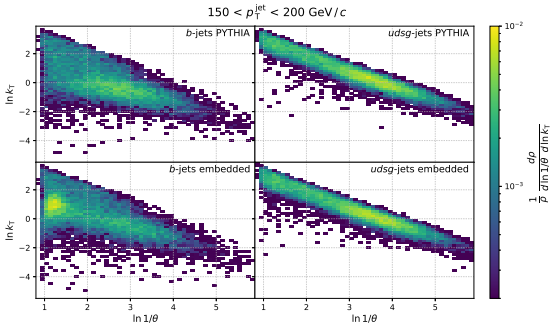

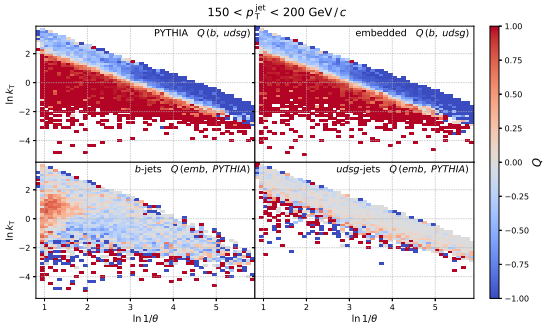

A.3 Groomed with max-z

A.3.1 $40 < p_{\mathrm{T}}^{\mathrm{jet}} < 50\,\mathrm{GeV}/c$

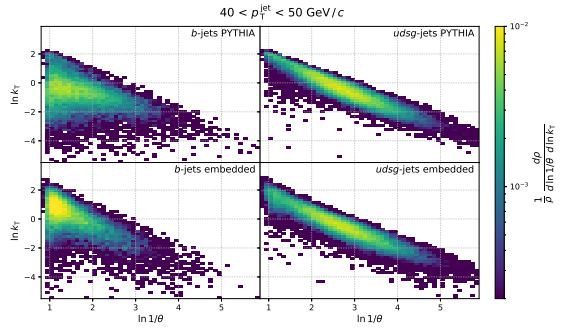

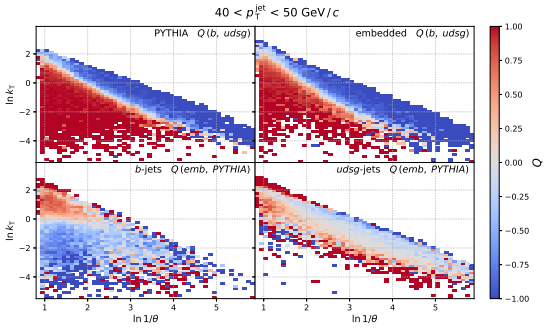

A.3.2 $80 < p_{\mathrm{T}}^{\mathrm{jet}} < 100\,\mathrm{GeV}/c$

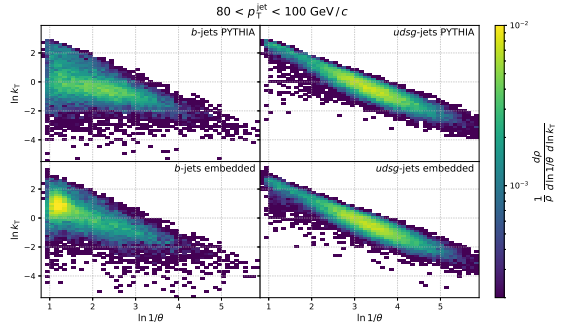

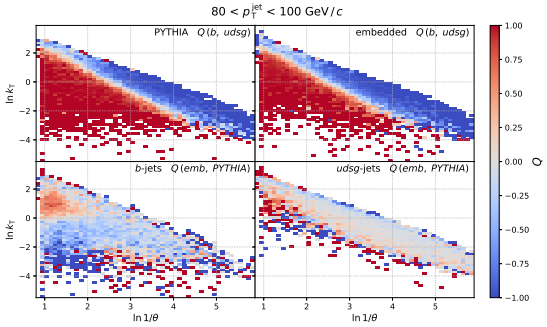

A.3.3 $150 < p_{\mathrm{T}}^{\mathrm{jet}} < 200\,\mathrm{GeV}/c$

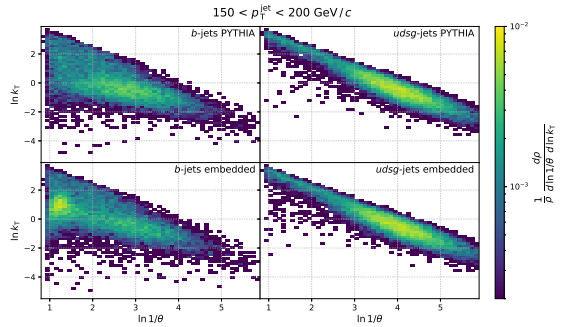

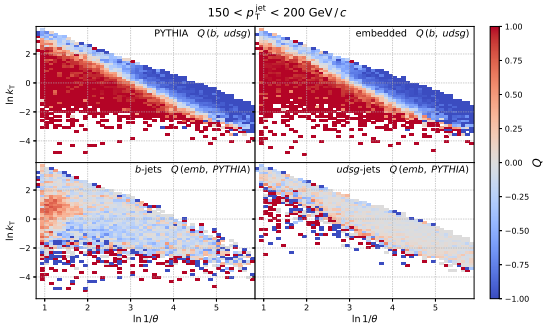

A.4 Groomed with SD ($\beta = 0, z_{\mathrm{cut}} = 0.2$)

A.4.1 $40 < p_{\mathrm{T}}^{\mathrm{jet}} < 50\,\mathrm{GeV}/c$

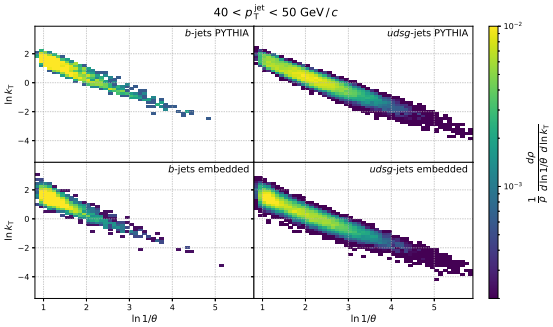

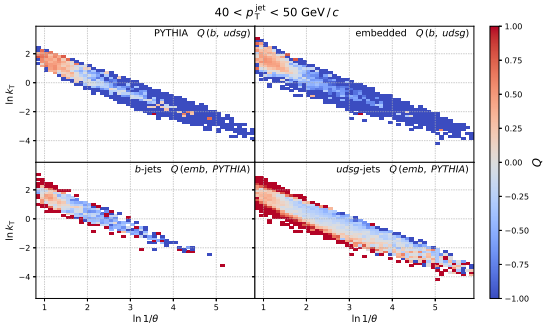

A.4.2 $80 < p_{\mathrm{T}}^{\mathrm{jet}} < 100\,\mathrm{GeV}/c$

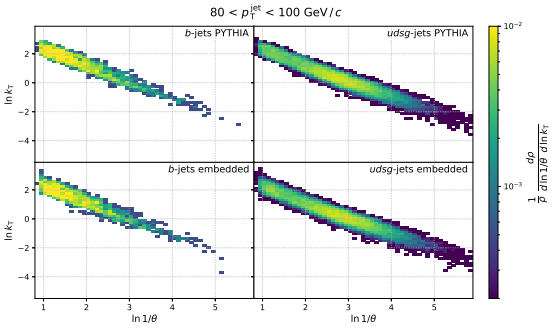

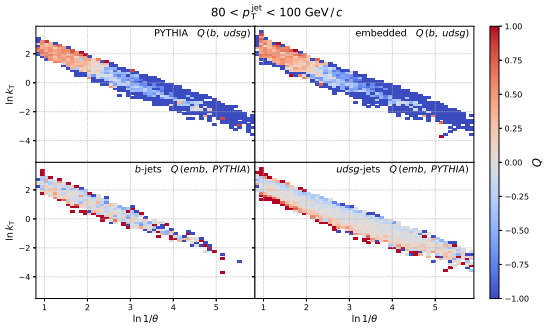

A.4.3 $150 < p_{\mathrm{T}}^{\mathrm{jet}} < 200\,\mathrm{GeV}/c$

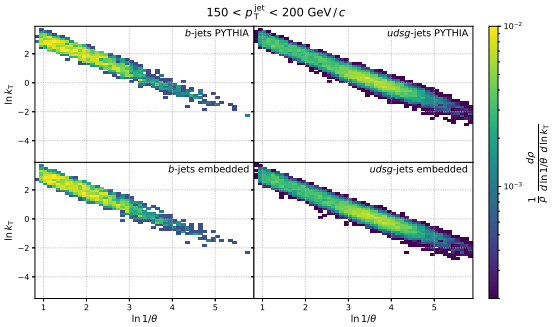

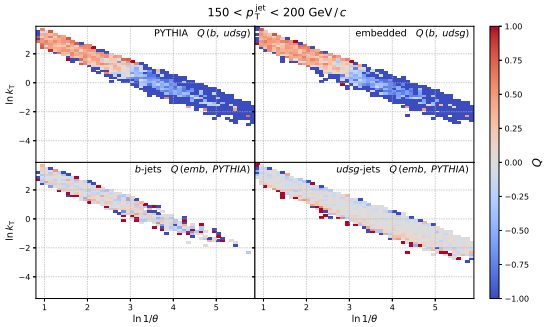

A.5 Groomed with last splitting passing SD ($\beta = 0, z_{\mathrm{cut}} = 0.2$)

A.5.1 $40 < p_{\mathrm{T}}^{\mathrm{jet}} < 50\,\mathrm{GeV}/c$

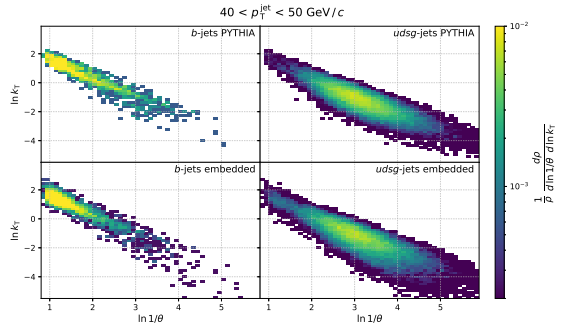

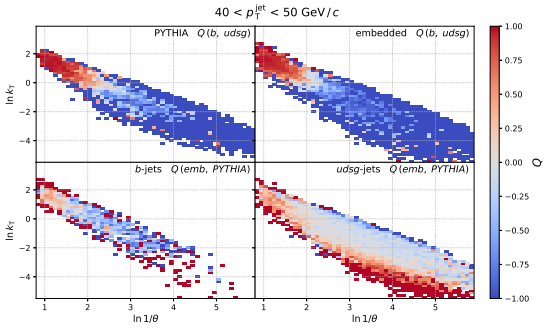

A.5.2 $80 < p_{\mathrm{T}}^{\mathrm{jet}} < 100\,\mathrm{GeV}/c$

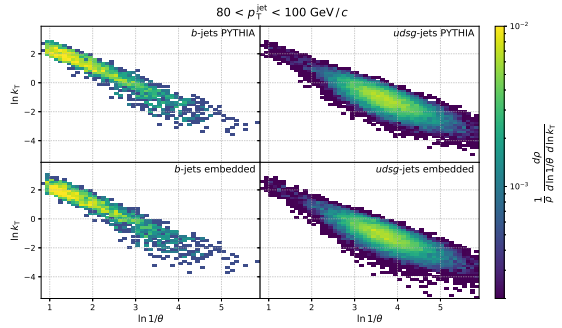

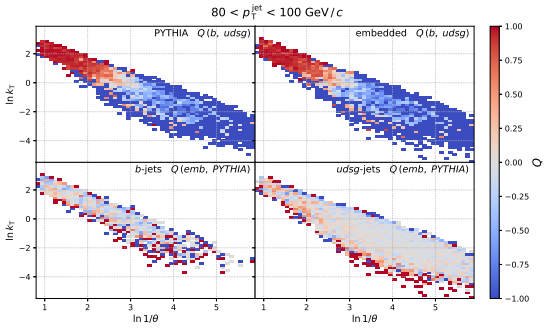

A.5.3 $150 < p_{\mathrm{T}}^{\mathrm{jet}} < 200\,\mathrm{GeV}/c$

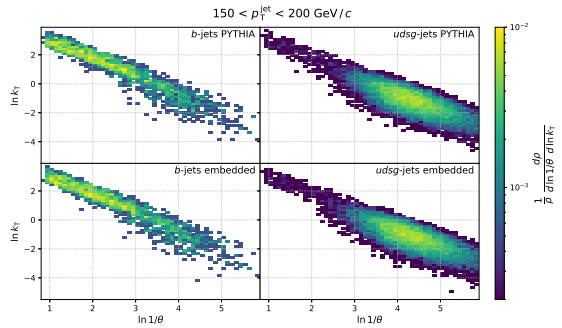

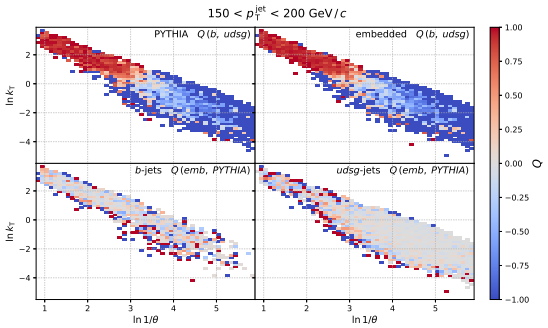

A.6 Groomed with max-$z/\theta_{|k_T>0.1}$

A.6.1 $40 < p_T^{jet} < 50\,GeV/c$

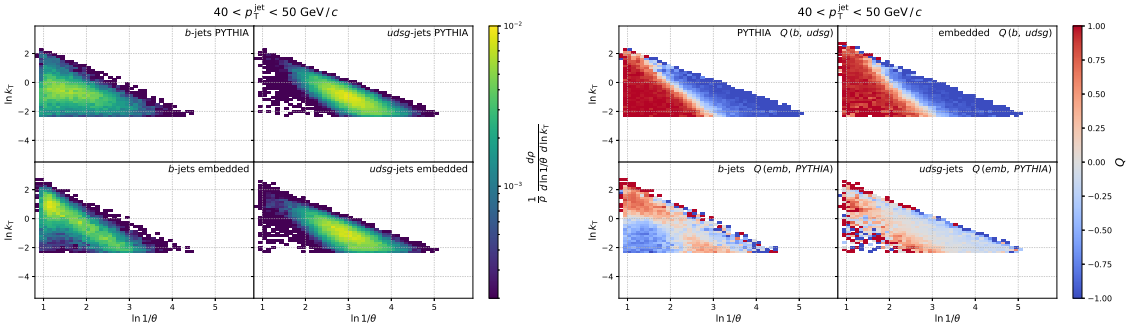

A.6.2 $80 < p_T^{jet} < 100\,GeV/c$

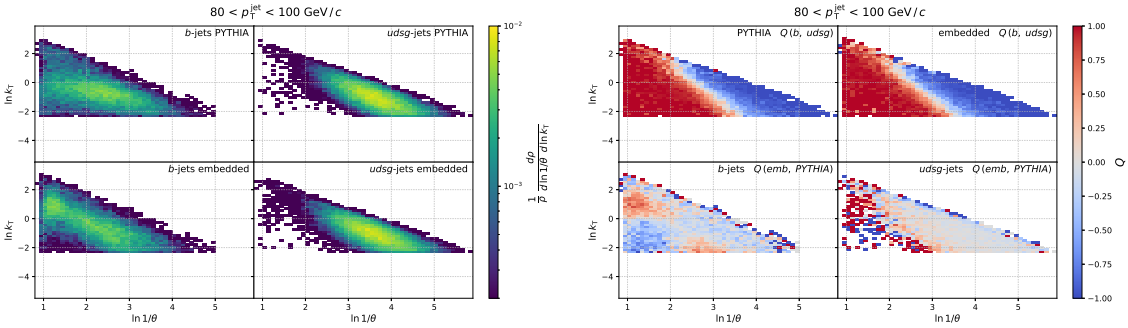

A.6.3 $150 < p_T^{jet} < 200\,GeV/c$

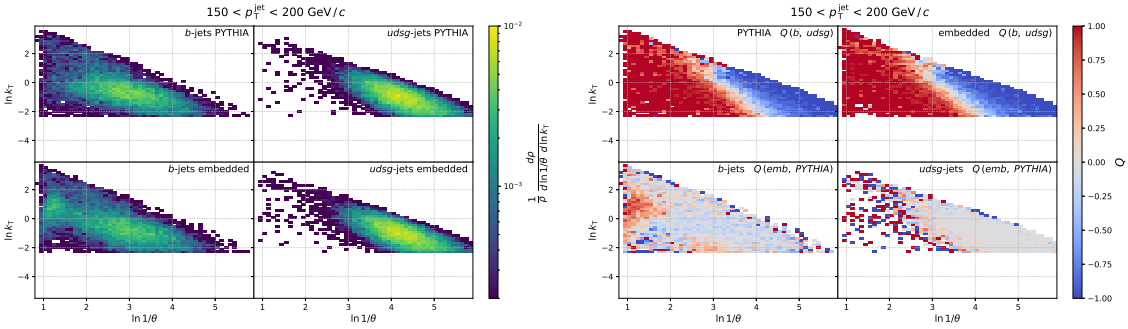

Appendix B

Reclustering of random particles with CA

It is worth studying the simple geometrical properties of CA reclustering in the case of jets with many constituents. For this purpose, an extremely simplified setup was prepared: N_{const} particles with $p_{\mathrm{T}} = 1\,\mathrm{GeV}/c$ were randomly placed in the circle of radius equal $R = 0.4$ on $\eta - \varphi$ plane. Two variations are considered: first with no additional constraints (denoted *without core*) and second when one of the constituents is assigned huge $p_{\mathrm{T}} \gg 1\,\mathrm{GeV}/c$ and is placed at the centre of the circle (called *with core*). All the particles forming these artificial jets (called *jets* for simplicity for the rest of this appendix) are reclustered with the CA algorithm. Only first-order splittings from the leading branch (*i.e.* those corresponding to the primary Lund plane) are further considered.

The uniform angular distribution of particles within the jet reflects well the properties of the uncorrelated heavy-ion background. It is not an accurate picture of vacuum jets. The presence of the core particle is a naïve proxy for the hard jet embedded in the background. This proxy is closer to reality for heavy-flavour jets.

We note that typical ranges (10%–90% percentiles) for the number of constituents for $100\,\mathrm{GeV}/c$ jets simulated with PYTHIA are around 8–22 and 3–11 for *udsg*– and *b*–jets, respectively (for stable beauty hadrons). After embedding into the thermal background and constituent subtraction procedure as described in Chapter 4 they grow to 17–53 and 7–38.

Fig. B.1 shows the relation between the number of primary splittings and the number of constituents of the jet. The relation is close to $N_{splittings} \sim \log(N_{const})$ with some signs of saturation for a higher number of constituents. For the core case, with the higher number of constituents, one could describe this as "background particles are mostly clustered among themselves". These observations are probably not too surprising.

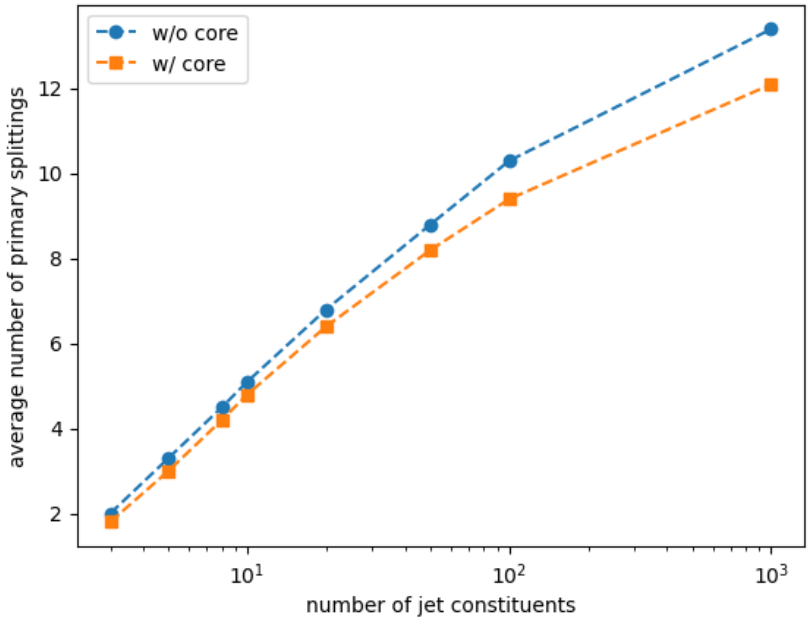

Figure B.1: Average number of primary splittings after CA reclustering of artificial jets as a function of the number of constituents of the jet.

What is more interesting is what the splitting angle θ distributions look like. They are shown in Fig. B.2 and Fig. B.3 for cases without and with core consecutively. For $N_{const} = 3$, the angle distribution differs very much between the two considered scenarios - for jets with core the probability is proportional to the area of the thin ring with radius $\mathrm{d}R = \theta$ around the jet centre. For the case without core, the distributions reach much higher values, even close to $0.8 = 2R$, due to the finite probability of all the particles being placed around $\mathrm{d}R = 0.4$ from the middle of the jet.

As $N_{constit}$ grows, the distributions for the two scenarios become more similar. However, even for 1000 random particles put inside the jet, the presence of the single core particle still has a significant impact on the final distribution.

The shapes of the θ distributions are then really peculiar, with $\theta = 0.2$ being the "forbidden" value. It can be understood from the illustrations shown in Fig. B.4. Any particle at a given distance from the jet centre $\mathrm{d}R_0$, before being merged to the jet core, has to first be clustered with all particles closer than $\mathrm{d}R_0$ from it. This is true until 4 or 5 centres of gravity around $\mathrm{d}R_0 = 0.3$ are left (4 or 5 are universal numbers for any sufficiently large N_{const}). We call them *distant clusters*. They are not further clustered together as the distance between them is larger than their $\mathrm{d}R_0$ – they become primary splittings. As they collect particles from significant jet area, they accumulate large p_{T}. Particles lying at $\mathrm{d}R_0 \gtrsim 0.3$ are merged with these 4 or 5 distant clusters. Particles at $\mathrm{d}R_0 < 0.3$ are merged either to the jet core (becoming primary splittings) or one of the distant clusters (becoming their secondary splittings) – whatever is closer. For particles at $\mathrm{d}R = 0.2$, it is almost always the second option.

While the behaviour for $N_{const} = 1000$ can be treated as a curiosity, this simple picture illustrates an important property of reclustering with CA algorithm. The usage of a very simple simulation setup confirms that this is purely a geometrical property, without any underlying physics.

Already for $N \geq 8$ randomly placed particles (below typical heavy-ion jet multiplicity) a clear bimodal shape of the θ distribution is observed. It is true for both extreme considered

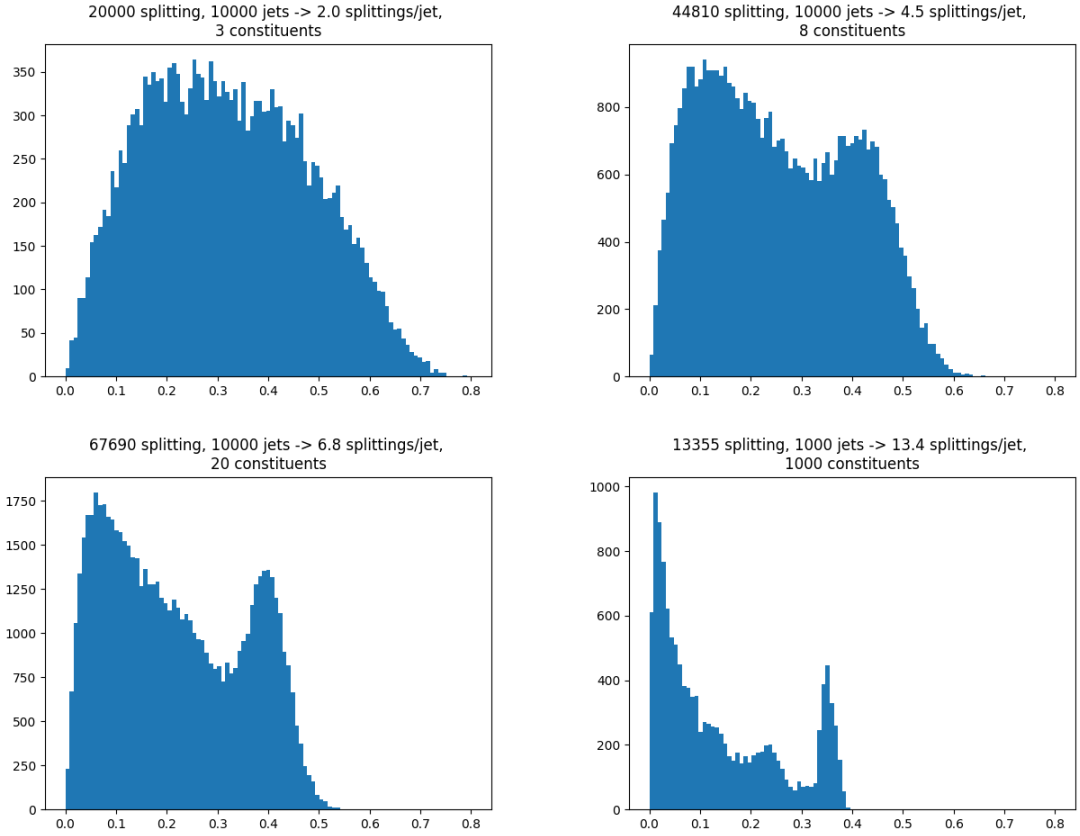

Figure B.2: Distributions of splitting angle θ of primary splititngs for various N_{const} for scenario without core. Distributions were averaged over 10000 jet generations. $N_{const} = 3$, 8, 20, and 1000 in the top left, top right, bottom left, and bottom right plots, respectively. The horizontal axes range from 0 to 0.8.

scenarios - with and without a core. The details, like the relative area under the two peaks or their exact shapes, depend on the N_{const} and the presence of the core.

Arguably common intuition, that uncorrelated heavy-ion background contributes mostly to the large θ part of the distribution is not true (or at least should not be taken for granted). In fact, random particles tend to form a bimodal distribution. A similar effect is observed in a simulation of realistic PYTHIA jets embedded in the thermal background, as shown in Chapter 4.

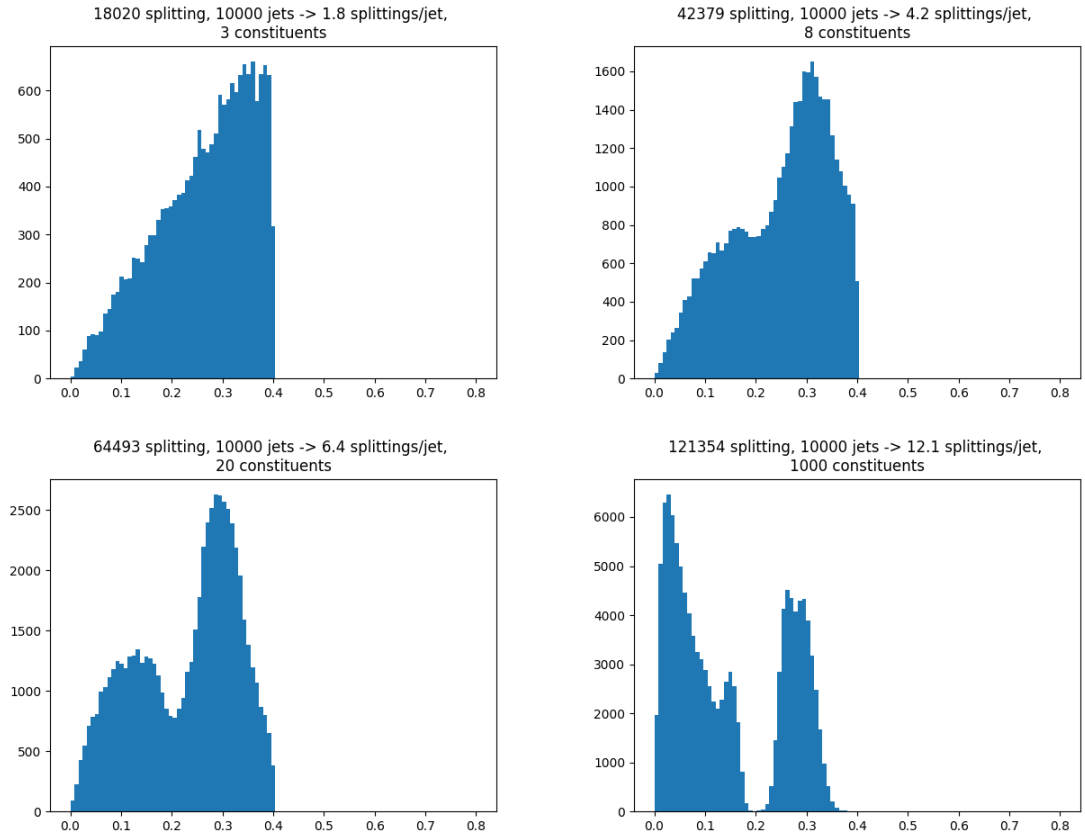

Figure B.3: Distributions of splitting angle θ of primary splititngs for various N_{const} for scenario with core. Distributions were averaged over 10000 jet generations. N_{const} = 3, 8, 20, and 1000 in the top left, top right, bottom left, and bottom right plots, respectively. The horizontal axes range from 0 to 0.8.

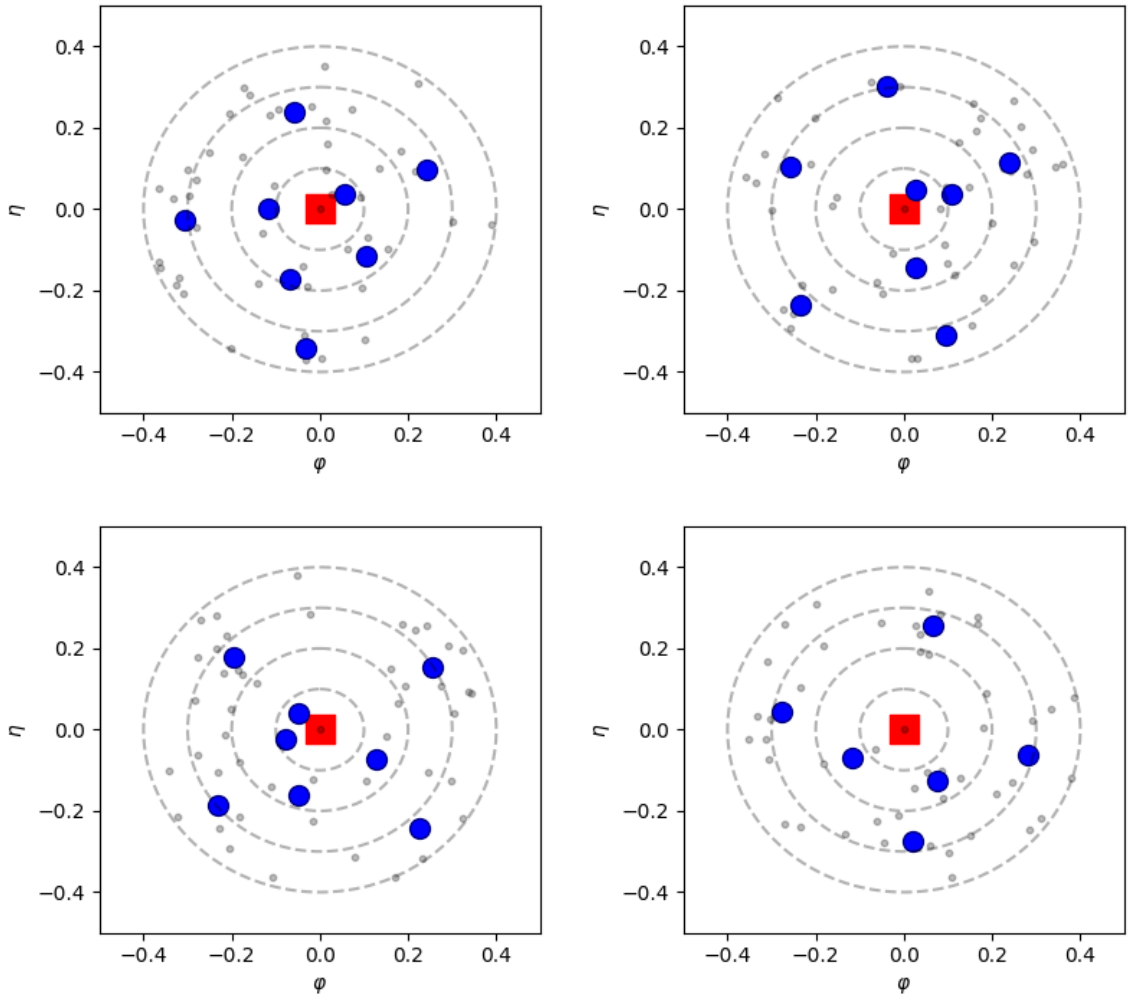

Figure B.4: Examples of jets with $N_{constit} = 50$, with core scenario. Small gray dots denote jet constituents, large blue dots denote primary splittings and square marks the jet core. Concentric dashed circles have radii of 0.1, 0.2, 0.3 and 0.4.

Bibliography

[1] A. Purcell, "Go on a particle quest at the first CERN webfest. Le premier webfest du CERN se lance à la conquête des particules", (2012), https://cds.cern.ch/record/1473657.

[2] M. E. Peskin and D. V. Schroeder, *An Introduction to quantum field theory* (Addison-Wesley, Reading, USA, 1995).

[3] A. Zee, *Quantum field theory in a nutshell, Published in: Princeton, UK: Princeton Univ. Pr. (2010) 576 p* (2003).

[4] **PDG** Collaboration, R. Workman et al., "Review of Particle Physics: 2022", PTEP **2022**, 083C01 (2022), http://cds.cern.ch/record/2836514.

[5] C. W. Bauer et al., "An Effective field theory for collinear and soft gluons: Heavy to light decays", Phys. Rev. D **63**, 114020 (2001), arXiv:hep-ph/0011336.

[6] Y. L. Dokshitzer, "Calculation of the Structure Functions for Deep Inelastic Scattering and e+ e- Annihilation by Perturbation Theory in Quantum Chromodynamics.", Sov. Phys. JETP **46**, 641 (1977).

[7] V. N. Gribov and L. N. Lipatov, "Deep inelastic e p scattering in perturbation theory", Sov. J. Nucl. Phys. **15**, 438 (1972).

[8] G. Altarelli and G. Parisi, "Asymptotic Freedom in Parton Language", Nucl. Phys. B **126**, 298 (1977).

[9] B. Andersson et al., "Parton Fragmentation and String Dynamics", Phys. Rept. **97**, 31 (1983).

[10] G. P. Salam and G. Soyez, "A Practical Seedless Infrared-Safe Cone jet algorithm", JHEP **05**, 086 (2007), arXiv:0704.0292 [hep-ph].

[11] G. P. Salam, "Towards Jetography", Eur. Phys. J. C **67**, 637 (2010), arXiv:0906.1833 [hep-ph].

[12] M. Cacciari and G. P. Salam, "Dispelling the N^3 myth for the k_t jet-finder", Phys. Lett. B **641**, 57 (2006), arXiv:hep-ph/0512210.

[13] S. Catani et al., "Longitudinally invariant K_t clustering algorithms for hadron hadron collisions", Nucl. Phys. B **406**, 187 (1993).

[14] S. D. Ellis and D. E. Soper, "Successive combination jet algorithm for hadron collisions", Phys. Rev. D **48**, 3160 (1993), arXiv:hep-ph/9305266.

[15] Y. L. Dokshitzer et al., "Better jet clustering algorithms", JHEP **08**, 001 (1997), arXiv:hep-ph/9707323.

[16] M. Wobisch and T. Wengler, "Hadronization corrections to jet cross-sections in deep inelastic scattering", in Workshop on Monte Carlo Generators for HERA Physics (Plenary Starting Meeting) (Apr. 1998), pp. 270–279, arXiv:hep-ph/9907280.

[17] M. Cacciari, G. P. Salam, and G. Soyez, "The anti-k_t jet clustering algorithm", JHEP **04**, 063 (2008), arXiv:0802.1189 [hep-ph].

[18] M. Cacciari, G. P. Salam, and G. Soyez, "FastJet User Manual", Eur. Phys. J. C **72**, 1896 (2012), arXiv:1111.6097 [hep-ph].

[19] G. P. Salam, *Jets and jet substructure 2: using jets*, https://gsalam.web.cern.ch/gsalam/repository/talks/2014-CFHEP-jets2.pdf, Accessed: 2023-08-01.

[20] L. G. Almeida et al., "Substructure of high-p_T Jets at the LHC", Phys. Rev. D **79**, 074017 (2009), arXiv:0807.0234 [hep-ph].

[21] A. J. Larkoski, J. Thaler, and W. J. Waalewijn, "Gaining (Mutual) Information about Quark/Gluon Discrimination", JHEP **11**, 129 (2014), arXiv:1408.3122 [hep-ph].

[22] J. Cogan et al., "Jet-Images: Computer Vision Inspired Techniques for Jet Tagging", JHEP **02**, 118 (2015), arXiv:1407.5675 [hep-ph].

[23] S. Marzani, G. Soyez, and M. Spannowsky, *Looking inside jets: an introduction to jet substructure and boosted-object phenomenology*, Vol. 958 (Springer, 2019), arXiv:1901.10342 [hep-ph].

[24] A. J. Larkoski, I. Moult, and B. Nachman, "Jet Substructure at the Large Hadron Collider: A Review of Recent Advances in Theory and Machine Learning", Phys. Rept. **841**, 1 (2020), arXiv:1709.04464 [hep-ph].

[25] R. Kogler et al., "Jet Substructure at the Large Hadron Collider: Experimental Review", Rev. Mod. Phys. **91**, 045003 (2019), arXiv:1803.06991 [hep-ex].

[26] M. Bahr et al., "Herwig++ Physics and Manual", Eur. Phys. J. C **58**, 639 (2008), arXiv:0803.0883 [hep-ph].

[27] F. A. Dreyer, G. P. Salam, and G. Soyez, "The Lund Jet Plane", JHEP **12**, 064 (2018), arXiv:1807.04758 [hep-ph].

[28] **ATLAS** Collaboration, G. Aad et al., "Measurement of the Lund Jet Plane Using Charged Particles in 13 TeV Proton-Proton Collisions with the ATLAS Detector", Phys. Rev. Lett. **124**, 222002 (2020), arXiv:2004.03540 [hep-ex].

[29] **ALICE** Collaboration, *Physics Preliminary Summary: Measurement of the primary Lund plane density in pp collisions at $\sqrt{s} = 13$ TeV with ALICE*, tech. rep., ALICE-PUBLIC-2021-002 (2021), https://cds.cern.ch/record/2759456.

[30] **CMS** Collaboration, *Measurement of the primary Lund jet plane density in proton-proton collisions at $\sqrt{s} = 13$ TeV*, tech. rep., CMS-PAS-SMP-22-007 (CERN, Geneva, 2023), https://cds.cern.ch/record/2853467.

[31] **ALICE** Collaboration, S. Acharya et al., "Measurement of the groomed jet radius and momentum splitting fraction in pp and Pb−Pb collisions at $\sqrt{s_{NN}} = 5.02$ TeV", Phys. Rev. Lett. **128**, 102001 (2022), arXiv:2107.12984 [nucl-ex].

[32] A. J. Larkoski et al., "Soft Drop", JHEP **05**, 146 (2014), arXiv:1402.2657 [hep-ph].

[33] Y. Mehtar-Tani, A. Soto-Ontoso, and K. Tywoniuk, "Dynamical grooming of QCD jets", Phys. Rev. D **101**, 034004 (2020), arXiv:1911.00375 [hep-ph].

[34] P. Caucal, A. Soto-Ontoso, and A. Takacs, "Dynamical Grooming meets LHC data", JHEP **07**, 020 (2021), arXiv:2103.06566 [hep-ph].

[35] J. Mulligan and M. Ploskon, "Identifying groomed jet splittings in heavy-ion collisions", Phys. Rev. C **102**, 044913 (2020), arXiv:2006.01812 [hep-ph].

[36] **CMS** Collaboration, V. Khachatryan et al., "Measurement of $B\bar{B}$ Angular Correlations based on Secondary Vertex Reconstruction at $\sqrt{s} = 7$ TeV", JHEP **03**, 136 (2011), arXiv:1102.3194 [hep-ex].

[37] **DELPHI** Collaboration, J. Abdallah et al., "A study of the b-quark fragmentation function with the DELPHI detector at LEP I and an averaged distribution obtained at the Z Pole", Eur. Phys. J. C **71**, 1557 (2011), arXiv:1102.4748 [hep-ex].

[38] **ALEPH** Collaboration, A. Heister et al., "Study of the fragmentation of b quarks into B mesons at the Z peak", Phys. Lett. B **512**, 30 (2001), arXiv:hep-ex/0106051.

[39] **OPAL** Collaboration, G. Abbiendi et al., "Inclusive analysis of the b quark fragmentation function in Z decays at LEP", Eur. Phys. J. C **29**, 463 (2003), arXiv:hep-ex/0210031.

[40] **SLD** Collaboration, K. Abe et al., "Measurement of the b quark fragmentation function in Z0 decays", Phys. Rev. D **65**, [Erratum: Phys.Rev.D 66, 079905 (2002)], 092006 (2002), arXiv:hep-ex/0202031.

[41] **ATLAS** Collaboration, G. Aad et al., "Measurement of b-quark fragmentation properties in jets using the decay $B^{\pm} \to J/\psi K^{\pm}$ in pp collisions at $\sqrt{s} = 13$ TeV with the ATLAS detector", JHEP **12**, 131 (2021), arXiv:2108.11650 [hep-ex].

[42] **ATLAS** Collaboration, G. Aad et al., "Measurements of jet observables sensitive to b-quark fragmentation in tt^{-} events at the LHC with the ATLAS detector", Phys. Rev. D **106**, 032008 (2022), arXiv:2202.13901 [hep-ex].

[43] **ALICE** Collaboration, S. Acharya et al., "Measurement of the production of charm jets tagged with D^0 mesons in pp collisions at $\sqrt{s} = 5.02$ and 13 TeV", JHEP **06**, 133 (2023), arXiv:2204.10167 [nucl-ex].

[44] **ALICE** Collaboration, S. Acharya et al., "Measurements of groomed-jet substructure of charm jets tagged by D^0 mesons in proton-proton collisions at $\sqrt{s} = 13$ TeV", (2022), arXiv:2208.04857 [nucl-ex].

[45] Y. L. Dokshitzer, V. A. Khoze, and S. I. Troian, "On specific QCD properties of heavy quark fragmentation ('dead cone')", J. Phys. G **17**, 1602 (1991).

[46] L. Cunqueiro and M. Płoskoń, "Searching for the dead cone effects with iterative declustering of heavy-flavor jets", Phys. Rev. D **99**, 074027 (2019), arXiv:1812.00102 [hep-ph].

[47] K. Garner, *Reconstruction of Bottom Jets in Proton-Proton Collisions at $\sqrt{s}$ =13 TeV with ALICE*, https://indico.cern.ch/event/755366/contributions/3357599/attachments/1859342/3055162/KGarner_PosterSQM.pdf, Accessed: 2023-08-01.

[48] **ALICE** Collaboration, S. Acharya et al., "Direct observation of the dead-cone effect in quantum chromodynamics", Nature **605**, [Erratum: Nature 607, E22 (2022)], 440 (2022), arXiv:2106.05713 [nucl-ex].

[49] **NA61/SHINE** Collaboration, L. Turko, "Looking for the Phase Transition–Recent NA61/SHINE Results", Universe **4**, edited by D. Blaschke et al., 52 (2018), arXiv:1801.06919 [hep-ex].

[50] **HotQCD** Collaboration, A. Bazavov et al., "Equation of state in (2+1)-flavor QCD", Phys. Rev. D **90**, 094503 (2014), arXiv:1407.6387 [hep-lat].

[51] T. Bhattacharya et al., "QCD Phase Transition with Chiral Quarks and Physical Quark Masses", Phys. Rev. Lett. **113**, 082001 (2014), arXiv:1402.5175 [hep-lat].

[52] C. Ratti and R. Bellwied, *The Deconfinement Transition of QCD: Theory Meets Experiment*, Vol. 981, Lecture Notes in Physics (June 2021).

[53] A. Bzdak et al., "Mapping the Phases of Quantum Chromodynamics with Beam Energy Scan", Phys. Rept. **853**, 1 (2020), arXiv:1906.00936 [nucl-th].

[54] "The ALICE experiment – A journey through QCD", (2022), arXiv:2211.04384 [nucl-ex].

[55] P. Foka and M. A. Janik, "An overview of experimental results from ultra-relativistic heavy-ion collisions at the CERN LHC: Bulk properties and dynamical evolution", Rev. Phys. **1**, 154 (2016), arXiv:1702.07233 [hep-ex].

[56] **ALICE** Collaboration, B. B. Abelev et al., "Elliptic flow of identified hadrons in Pb-Pb collisions at $\sqrt{s_{\rm NN}} = 2.76$ TeV", JHEP **06**, 190 (2015), arXiv:1405.4632 [nucl-ex].

[57] **ALICE** Collaboration, K. Aamodt et al., "Higher harmonic anisotropic flow measurements of charged particles in Pb-Pb collisions at $\sqrt{s_{NN}}$=2.76 TeV", Phys. Rev. Lett. **107**, 032301 (2011), arXiv:1105.3865 [nucl-ex].

[58] U. Heinz and R. Snellings, "Collective flow and viscosity in relativistic heavy-ion collisions", Ann. Rev. Nucl. Part. Sci. **63**, 123 (2013), arXiv:1301.2826 [nucl-th].

[59] P. Kovtun, D. T. Son, and A. O. Starinets, "Viscosity in strongly interacting quantum field theories from black hole physics", Phys. Rev. Lett. **94**, 111601 (2005), arXiv:hep-th/0405231.

[60] J. Rafelski and B. Muller, "Strangeness Production in the Quark - Gluon Plasma", Phys. Rev. Lett. **48**, [Erratum: Phys.Rev.Lett. 56, 2334 (1986)], 1066 (1982).

[61] **CMS** Collaboration, A. M. Sirunyan et al., "Measurement of nuclear modification factors of Υ(1S), Υ(2S), and Υ(3S) mesons in PbPb collisions at $\sqrt{s_{\rm NN}} = 5.02$ TeV", Phys. Lett. B **790**, 270 (2019), arXiv:1805.09215 [hep-ex].

[62] **CMS** Collaboration, V. Khachatryan et al., "Measurement of transverse momentum relative to dijet systems in PbPb and pp collisions at $\sqrt{s_{\rm NN}} = 2.76$ TeV", JHEP **01**, 006 (2016), arXiv:1509.09029 [nucl-ex].

[63] **CMS** Collaboration, A. M. Sirunyan et al., "Comparing transverse momentum balance of b jet pairs in pp and PbPb collisions at $\sqrt{s_{\rm NN}} = 5.02$ TeV", JHEP **03**, 181 (2018), arXiv:1802.00707 [hep-ex].

[64] "Measurement of the radius dependence of charged-particle jet suppression in Pb-Pb collisions at $\sqrt{s_{\rm NN}} = 5.02$ TeV", (2023), arXiv:2303.00592 [nucl-ex].

[65] M. Gyulassy and X.-n. Wang, "Multiple collisions and induced gluon Bremsstrahlung in QCD", Nucl. Phys. **B420**, 583 (1994), arXiv:nucl-th/9306003 [nucl-th].

[66] R. Baier et al., "Radiative energy loss of high-energy quarks and gluons in a finite volume quark - gluon plasma", Nucl. Phys. B **483**, 291 (1997), arXiv:hep-ph/9607355.

[67] R. Baier et al., "Radiative energy loss and p(T) broadening of high-energy partons in nuclei", Nucl. Phys. B **484**, 265 (1997), arXiv:hep-ph/9608322.

[68] Y. Mehtar-Tani, C. A. Salgado, and K. Tywoniuk, "Jets in QCD Media: From Color Coherence to Decoherence", Phys. Lett. B **707**, 156 (2012), arXiv:1102.4317 [hep-ph].

[69] **ATLAS** Collaboration, G. Aad et al., "Measurement of the nuclear modification factor of b-jets in 5.02 TeV Pb+Pb collisions with the ATLAS detector", Eur. Phys. J. C **83**, 438 (2023), arXiv:2204.13530 [nucl-ex].

[70] **ATLAS** Collaboration, *Heavy Ion RAA summary Plots 2022*, tech. rep. (CERN, Geneva, 2022), https://cds.cern.ch/record/2807726.

[71] N. Armesto, C. A. Salgado, and U. A. Wiedemann, "Medium induced gluon radiation off massive quarks fills the dead cone", Phys. Rev. D **69**, 114003 (2004), arXiv:hep-ph/0312106.

[72] H. A. Andrews et al., "Novel tools and observables for jet physics in heavy-ion collisions", J. Phys. G **47**, 065102 (2020), arXiv:1808.03689 [hep-ph].

[73] **ALICE** Collaboration, K. Aamodt et al., "The ALICE experiment at the CERN LHC", JINST **3**, S08002 (2008).

[74] **ALICE** Collaboration, B. B. Abelev et al., "Performance of the ALICE Experiment at the CERN LHC", Int. J. Mod. Phys. **A29**, 1430044 (2014), arXiv:1402.4476 [nucl-ex].

[75] **ALICE** Collaboration, B. Abelev et al., "Upgrade of the ALICE Experiment: Letter Of Intent", Journal of Physics G: Nuclear and Particle Physics **41**, 087001 (2014).

[76] "ALICE upgrades during the LHC Long Shutdown 2", (2023), arXiv:2302.01238 [physics.ins-det].

[77] **ALICE** Collaboration, *ALICE 2017 luminosity determination for pp collisions at* $\sqrt{s}$ *= 5 TeV*, tech. rep., ALICE-PUBLIC-2018-014 (CERN, 2018), https://cds.cern.ch/record/2648933.

[78] **ALICE** Collaboration, P. Kuijer, "The inner tracking system of the Alice experiment", Nucl. Instrum. Meth. A **530**, edited by C. Civinini and E. Focardi, 28 (2004).

[79] **ALICE** Collaboration, G. Dellacasa et al., *ALICE technical design report of the inner tracking system (ITS)*, tech. rep., CERN-LHCC-99-12 (June 1999), https://cds.cern.ch/record/1625842.

[80] **ALICE** Collaboration, C. Lippmann, *Upgrade of the ALICE Time Projection Chamber*, tech. rep., CERN-LHCC-2013-020, ALICE-TDR-016 (Mar. 2014), https://cds.cern.ch/record/1622286/.

[81] J. Alme et al., "The ALICE TPC, a large 3-dimensional tracking device with fast readout for ultra-high multiplicity events", Nucl. Instrum. Methods Phys. Res., A **622**, 316 (2010).

[82] R. Veenhof, *Choosing a gas mixture for the ALICE TPC*, tech. rep., ALICE-INT-2003-29 (May 2003).

[83] **ALICE** Collaboration, J. Adam et al., "Centrality dependence of the pseudorapidity density distribution for charged particles in Pb-Pb collisions at $\sqrt{s_{\rm NN}}$ = 5.02 TeV", Phys. Lett. B **772**, 567 (2017), arXiv:1612.08966 [nucl-ex].

[84] W. Blum, L. Rolandi, and W. Riegler, *Particle detection with drift chambers*, Published in: Berlin, Germany: Springer (2008) 448 p (2008).

[85] M. Ivanov et al., "TPC tracking and particle identification in high-density environment", (2003), arXiv:physics/0306108.

[86] **ALICE** Collaboration, *The ALICE definition of primary particles*, tech. rep., ALICE-PUBLIC-2017-005 (2017), https://cds.cern.ch/record/2270008.

[87] **ALICE** Collaboration, S. Acharya et al., "Multiplicity dependence of charged-particle jet production in pp collisions at $\sqrt{\mathbf{s}}$ = **13 TeV**", Eur. Phys. J. C **82**, 514 (2022), arXiv:2202.01548 [nucl-ex].

[88] **ALICE** Collaboration, S. Acharya et al., "Measurement of charged jet cross section in *pp* collisions at $\sqrt{s}$ = 5.02 TeV", Phys. Rev. D **100**, 092004 (2019), arXiv:1905.02536 [nucl-ex].

[89] **ALICE** Collaboration, B. B. Abelev et al., "Charged jet cross sections and properties in proton-proton collisions at $\sqrt{s}$ = 7 TeV", Phys. Rev. D **91**, 112012 (2015), arXiv:1411.4969 [nucl-ex].

[90] **ALICE** Collaboration, J. Adam et al., "Centrality Dependence of the Charged-Particle Multiplicity Density at Midrapidity in Pb-Pb Collisions at $\sqrt{s_{\rm NN}}$ = 5.02 TeV", Phys. Rev. Lett. **116**, 222302 (2016), arXiv:1512.06104 [nucl-ex].

[91] **GEANT4** Collaboration, S. Agostinelli et al., "GEANT4–a simulation toolkit", Nucl. Instrum. Meth. A **506**, 250 (2003).

[92] P. Skands, S. Carrazza, and J. Rojo, "Tuning PYTHIA 8.1: the Monash 2013 Tune", Eur. Phys. J. C **74**, 3024 (2014), arXiv:1404.5630 [hep-ph].

[93] R. Brun et al., "GEANT Detector Description and Simulation Tool", 10.17181/CERN.MUHF.DMJ1 (1994).

[94] M. Cacciari, G. P. Salam, and G. Soyez, "The Catchment Area of Jets", JHEP **04**, 005 (2008), arXiv:0802.1188 [hep-ph].

[95] **CMS** Collaboration, S. Chatrchyan et al., "Measurement of the Underlying Event Activity in *pp* Collisions at $\sqrt{s} = 0.9$ and 7 TeV with the Novel Jet-Area/Median Approach", JHEP **08**, 130 (2012), arXiv:1207.2392 [hep-ex].

[96] A. Kalweit, "Production of light flavor hadrons and anti-nuclei at the LHC", PhD thesis (Darmstadt, Tech. U., 2012), https://cds.cern.ch/record/2283095/.

[97] T. Chen and C. Guestrin, "Xgboost: A scalable tree boosting system", in Proceedings of the 22nd ACM SIGKDD International Conference on Knowledge Discovery and Data Mining (2016), pp. 785–794, arXiv:1603.02754.

[98] L. Grinsztajn, E. Oyallon, and G. Varoquaux, "Why do tree-based models still outperform deep learning on typical tabular data?", in Proceedings of Advances in Neural Information Processing Systems, Vol. 35 (2022), pp. 507–520, arXiv:2207.08815.

[99] P. T. Komiske, E. M. Metodiev, and J. Thaler, "Energy Flow Networks: Deep Sets for Particle Jets", JHEP **01**, 121 (2019), arXiv:1810.05165 [hep-ph].

[100] H. Qu and L. Gouskos, "ParticleNet: Jet Tagging via Particle Clouds", Phys. Rev. D **101**, 056019 (2020), arXiv:1902.08570 [hep-ph].

[101] H. Qu, C. Li, and S. Qian, "Particle Transformer for Jet Tagging", (2022), arXiv:2202.03772 [hep-ph].

[102] M. Zaheer et al., "Deep sets", CoRR (2017), arXiv:1703.06114.

[103] **ATLAS** Collaboration, *Deep Sets based Neural Networks for Impact Parameter Flavour Tagging in ATLAS*, tech. rep., ATL-PHYS-PUB-2020-014 (2020), https://cds.cern.ch/record/2718948.

[104] J. H. Friedman, "Greedy function approximation: A gradient boosting machine.", Annals Statist. **29**, 1189 (2001).

[105] L. Breiman, "Random Forests", Machine Learning **45**, 5 (2001).

[106] A. Collaboration, *Charm production and fragmentation fractions at midrapidity in pp collisions at* $\sqrt{s} = 13$ *TeV*, 2023, arXiv:2308.04877 [hep-ex].

[107] **ALICE** Collaboration, S. Acharya et al., "Measurement of inclusive charged-particle b-jet production in pp and p-Pb collisions at $\sqrt{s_{\mathrm{NN}}} = 5.02$ TeV", JHEP **01**, 178 (2022), arXiv:2110.06104 [nucl-ex].

[108] J. Eschle et al., "Zfit: scalable pythonic fitting", SoftwareX **11**, 100508 (2020), https://doi.org/10.1016%2Fj.softx.2020.100508.

[109] L. Brenner et al., "Comparison of unfolding methods using RooFitUnfold", Int. J. Mod. Phys. A **35**, 2050145 (2020), arXiv:1910.14654 [physics.data-an].

[110] G. Cowan, "A survey of unfolding methods for particle physics", Conf. Proc. C **0203181**, edited by M. R. Whalley and L. Lyons, 248 (2002).

[111] A. Hocker and V. Kartvelishvili, "SVD approach to data unfolding", Nucl. Instrum. Meth. **A372**, 469 (1996), arXiv:hep-ph/9509307 [hep-ph].

[112] A. Tikhonov and V. Arsenin, *Solutions of ill-posed problems*, Halsted Press book (Winston, 1977).

[113] G. D'Agostini, "A Multidimensional unfolding method based on Bayes' theorem", Nucl. Instrum. Meth. **A362**, 487 (1995).

[114] Y. Vardi, "Empirical distributions in selection bias models", The Annals of Statistics **13**, 178 (1985).

[115] **ALICE** Collaboration, S. Acharya et al., "Measurements of inclusive jet spectra in pp and central Pb-Pb collisions at $\sqrt{s_{\mathrm{NN}}} = 5.02$ TeV", Phys. Rev. C **101**, 034911 (2020), arXiv:1909.09718 [nucl-ex].

[116] S. Frixione, P. Nason, and C. Oleari, "Matching NLO QCD computations with Parton Shower simulations: the POWHEG method", JHEP **11**, 070 (2007), arXiv:0709.2092 [hep-ph].

[117] S. Alioli et al., "Jet pair production in POWHEG", JHEP **04**, 081 (2011), arXiv:1012.3380 [hep-ph].

[118] **CMS** Collaboration, S. Chatrchyan et al., "Inclusive b-Jet Production in pp Collisions at $\sqrt{s} = 7$ TeV", JHEP **04**, 084 (2012), arXiv:1202.4617 [hep-ex].

[119] E. Craft et al., "Beautiful and Charming Energy Correlators", (2022), arXiv:2210.09311 [hep-ph].

[120] P. Berta et al., "Pileup and Underlying Event Mitigation with Iterative Constituent Subtraction", JHEP **08**, 175 (2019), arXiv:1905.03470 [hep-ph].

[121] Y. Mehtar-Tani, A. Soto-Ontoso, and K. Tywoniuk, "Tagging boosted hadronic objects with dynamical grooming", Phys. Rev. D **102**, 114013 (2020), arXiv:2005.07584 [hep-ph].

[122] **ALICE** Collaboration, L. Havener, "Jet splitting measurements in Pb–Pb and pp collisions at $\sqrt{s}_{\mathrm{NN}} = 5.02$ TeV with ALICE", Nucl. Phys. A **1005**, edited by F. Liu et al., 121906 (2021), arXiv:2002.05307 [nucl-ex].